Abstract

Development of a multi-purpose proton microbeam system: irradiation of tumor cells by energetic protons at the Bragg peak

By

Raafat Haibet

July 2021

Director of Dissertation: Jefferson L. Shinpaugh, PhD

Major Department: Physics

Employing ionization radiation to serve our communities has various applications in agricultural, industrial, and medical fields. The application of physics to medicine deals mainly with ionizing radiation in diagnosis and treating human therapeutic. Radiation treatment is a commonly utilized treatment for a variety of cancers in humans. The aim of utilizing radiation is to destroy tumor cells while reducing damage to healthy cells, and new techniques that can achieve that purpose are continuously being developed. A charged particle microbeam is a specialized opportunity to precisely control the number of particles crossing the individual cells and the dose location within the cell. The design and construction of the collimation and detection system significantly impact the target accuracy.

At East Carolina University, a horizontal multi-purpose microbeam and broad-beam system have been developed with a single electrostatic quadrupole quadruplet focusing lens. It has been combined with the 2 MV tandem Pelletron accelerator to generate a micrometer-sized beam and broad-sized beam for cell irradiation research. This system will have the capability to be used as the primary beam for a microPIXE (particle-induced x-ray emission) and neutron microbeam experimental system. In this study, an electrostatic quadruplet lens and a 10 μm Havar exit window were used to generate a proton microbeam, measured using the knife-edge technique. A 3 MeV proton beam was used to irradiate MCF 7 cancer cells at 0.5 and 1 Gy doses. In conjunction with these doses, the survival curve was calculated using the PrestoBlue assay.

Development of a multi-purpose proton microbeam system: irradiation of tumor cells by energetic protons at the Bragg peak

A Dissertation

Presented to The Faculty of the Department of Physics

East Carolina University

In Partial Fulfillment of the Requirements for the Degree Doctor of Philosophy in Biomedical Physics

By

Raafat Haibet

July 2021

Development of a multi-purpose proton microbeam system: irradiation of tumor cells by energetic protons at the Bragg peak

By

Raafat Haibet

APPROVED BY:

DISSERTATION ADVISOR _____

Jefferson Shinpaugh, Ph.D.

COMMITTEE MEMBER _____

Michael Dingfelder, Ph.D.

COMMITTEE MEMBER _____

Jean-Luc Scemama, Ph.D.

COMMITTEE MEMBER _____

Regina DeWitt, Ph.D.

COMMITTEE MEMBER _____

Kaida Yang, Ph.D.

CHAIR OF THE DEPARTMENT OF PHYSICS _____

Jefferson Shinpaugh, Ph.D.

DEAN OF THE GRADUATE SCHOOL _____

Paul J. Gemperline, Ph.D.

Dedication

To My Parents - My Lovely Wife Asraa - and My Children (Aous, Aymen, Ahmed, and Tanya):

I would like to dedicate this dissertation.

Acknowledgments

I would like to thank my advisor, Dr. Jefferson Shinpaugh, who can always be counted on for the best advice. His expertise and wisdom were invaluable in navigating the challenges, complications, and frustrations that could arise on any given day working in the lab.

I would like to thank my committee members: Dr. Michael Dingfelder, Dr. Regina DeWitt, Dr. Jean--Luc Scemama, Dr. Kaida Yang, for giving their time and using their expertise to assist me in accomplishing this endeavor.

I would like also to thank Dr. Guy Garty, Associate Professor of Radiation Oncology at CUMC, for his helping and advice.

Table of Contents

List of Tables:

List of Figures:

Chapter One
Introduction

1.1 Overview of Radiation:

When radiation penetrates matter, various outcomes can occur from energy deposition, depending on the type of radiation and the quantity of deposited energy. The electronic orbitals for an atom that surrounds the nucleus distribute dependent on the energy levels. So, releasing an electron occupying an orbital needs a specific amount of energy, called ionization energy.[1] The minimum energy required for ionization for an atom in all elements, ionization potential, ranges between a few eV (Alkali elements) to approximately 25 eV (Helium) [1]. Radiation can be classified into two principal classifications depend on its capability to ionize a material: [1,2]

- Non-ionizing radiation represents all electromagnetic radiation that cannot ionize matter due to its lower energy compared to the absorber ionization potential
- Ionizing radiation has quantum energy that exceeds the absorber's atoms and molecules' ionization potential and can ionize matter directly or indirectly.

1.2 Indirectly and Directly Ionizing Radiation:

Ionizing radiation is divided into two categories according to the ionization mode, and into two species according to the ionization density it produces in the absorber. According to the mechanism of ionization, there are two categories of ionizing radiation, indirectly and directly ionizing: [1,2]

1. Directly ionizing radiation is the direct step to deposit energy in the absorber, including Coulomb interactions between absorber atoms orbital electrons and the charged particle that directly ionizes. The charged particles consist of heavy ions, alpha particles, protons, and electrons.

2. Indirectly ionizing radiation is the two steps of deposit energy in the absorber in two steps as refer below:

    - The first step is to release charged particles in the absorber matter.
    - The second step is the releasing charged particles deposit their energy in the absorber by the Coulomb interactions with the absorber's electrons atoms. Finally, indirectly ionizing radiation consists of neutrons, gamma rays, and X-ray photons.

Developing the nuclear accelerator allowed developing energy and mass axes by increasing the energy and accelerating heavy particles like exploring nuclei far from the line's stability. The energetic ions generate defects that modify the material properties base on the irradiation studies concern for radiation damage to the material using nuclear reactors. The accelerator Ion beams produce novel ways to study the radiation damage to materials. The fundamental mechanism comprehension of radiation damage changing in a material structure will decrease the damage and improve the interest properties.[3]

1.3 A Brief History of Microprobe:

A microbeam can localize the radiation field to a micron-sized area using focusing and collimating techniques. Charged particles microbeams provide high spatial resolution quantitative analysis in the Physics, Chemistry, Biology, Geology, Archaeology, and Engineering samples. In 1950 at the University of Paris, Raimond Castaing demonstrated the possibility of exploiting the X-ray emitted from a specimen in an electron microscope for multi-elemental analysis in his significant step forward in X-ray emission spectrometry. Using a 1-μm beam diameter, he focused on a crystal spectrometer with a Geiger counter for X-ray detection and an electron microscope (commercial). The mainly metallurgical specimens were used for studying the spatial composition. This technique made progress when a scanning electron microscope was equipped with an x-ray spectrometer.

Incoming x-rays modulated the brightness of a cathode tube ray as a function of energy. The intensity of the created image gave a visual significance of distributing a given element as the electron probe scanned the sample. [4]

Nuclear physics research rapidly grew during the 1950s, and, consequently, the use of accelerators was also increasing. In addition, there was an extended interest in studying X-ray emission, as it was often prevalent as a background in nuclear and atomic physics experiments. So, it was logical for scientists to be attracted to theoretical and experimental research surrounding this phenomenon.

Naturally, physicists began thinking about the likelihood of utilizing heavy charged particles for analytical purposes due to the cross-section of X-ray production knowledge as a function of particle energy and atomic number. This interest was the prophecy of the theoretical formula for bremsstrahlung production, much less radiation for protons than for electrons. Since the excitation cross-section of characteristic X-ray production for MeV protons is the same for 10 keV electrons, the analysis's sensitivity is mainly determined by the bremsstrahlung background. [5]

That gave physicists inclined to use protons as the better projectile in X-ray emission analysis was experimentally found. The primary source of background is from the bremsstrahlung emit by the secondary electrons created by the proton beam, and the background induced by protons is negligible. [6]

In 1953 and 1959, Zirkle and Bloom studied cell division's fidelity following the irradiation of cells in metaphase using a charged particle microbeam. [7,8]

At the Lawrence Radiation Laboratory in Livermore, California, Khan and co-workers had attempted to apply proton-induced X-ray emission to elemental analysis during the 1960s. They used low-energy protons (100 KeV) to measure thin films' thickness and used a proportional counter for detecting the X-ray produced by the proton beam. The multielement analysis could not perform due to insufficient energy resolution to resolve adjacent elements. [9,10,11]

In the late 1960s, Shaw and Poole attempted to promote a proton analog to the electron microprobe. They used a 100 μm collimated beam generated by an accelerator to emit an X-ray for various pure metals and alloys, but no spectra were issued. In the same period, the significant development of nuclear detector technology was made. [6,12]

In 1970, the first proposed Particle Induced X-ray Emission (PIXE) technique by Sven Johansson et al. at the Lund institute of technology. They demonstrated that combining a MeV proton beam and a high-resolution Si detector constituted a powerful method for multi-elemental analysis of trace elements. [6,11,13,14]

During the 1970s, the new analytical technique's application and testes became popular in many nuclear physics laboratories—this rapid development was caused by several reasons:[15]

- The growing interest within the environmental issues created a requirement for effective techniques of trace-elements analysis.
- The increased availability of small accelerators in many nuclear physics laboratories results from a shift in interest to higher energies for nuclear physics research.
- The attention of PIXE was the progress of the microbeam method.

In 1972, at Nuclear Physics Division, AERE, Harwell, Nr. Didcot, Berks. (England) Harwell, Cookson, et al. used a quadrupole magnet system for developing a focused beam. Their measurement agreed satisfactorily with the theoretical prediction. The diameter of the 3MeV proton-focused beam was less than 4 μm. The microbeam method in PIXE (micro-PIXE) is beneficial in analyzing micron-sized specimens in various science fields.[16]

The microbeam analytical probe was described as its development and use in 1987 [16,17] by Grime and Watt. Numerous groups in the United States, Japan, and Europe have planned and developed an installation for microbeam irradiation biological cells in vitro using charged particles. They recognized the possibility of studying some important radiobiological manners that traditional broad field exposures cannot produce.

1.4 Ion Beam Analysis:

The ion beam analysis (IBA) techniques are well-established non-destructive analytical tools to explore a material's configurations. Several processes simultaneously induce when ion beams bump a material that causes secondary radiation and particles' emission.

These processes have supplied numerous analytical techniques classified depending on the process and detecting the reaction products [3]. Every method provides unique details and utilizes them for applications, as illustrated in figure 1.1 [3].

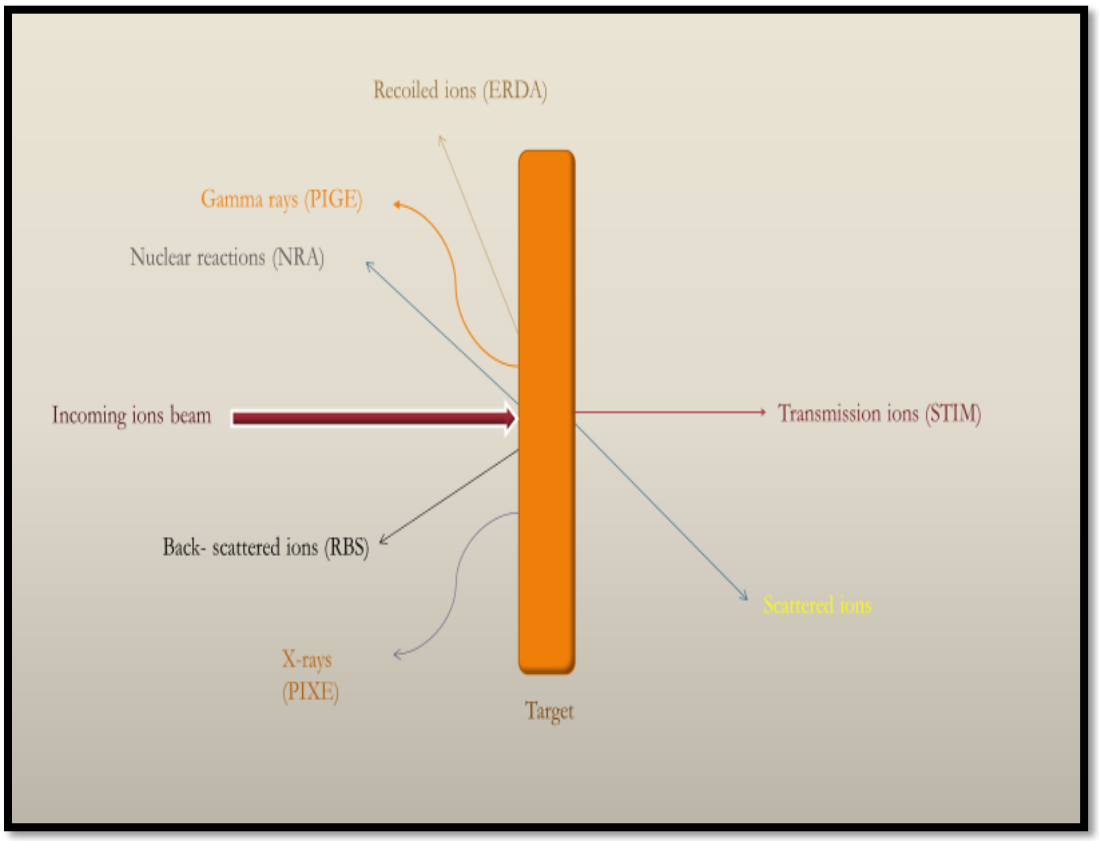

Figure 1.1: Ion beam interaction with the material [3]

1.5 The Principle of Microbeam:

A microbeam is a micrometer or sub-micrometer diameter radiation beam that enables accurate damage in particular positions inside biological specimens. The microbeam is a fundamental experimental technique for determining the cellular source of hazards associated with environmental and occupational exposure to low doses of charged particles.

The using microbeam gives a novel possibility to control a precise number of particles crossing single cells and localizing dose within the cell. [19]

The principal segments of the microbeam imply:

1. An ion beam source.
2. A focusing facility.
3. An ion detector determines a delivered dose.
4. A beam screen.
5. An imaging system.
6. A specific movement.

Several researchers have developed the individual cell's irradiation by the predefined precise number of alpha particles to provide the exact effects of one or more alpha particles over the last several years.[20]

1.6 A General Conception of The PIXE Technique:

For PIXE analysis, a beam of ions can be provided using a relatively small accelerator machine; the Van de Graaff accelerator was widely utilized during the evolution period of PIXE. This accelerator's typical terminal voltage is a few MV, producing approximately MeV energies for protons and twice for helium ions and several tens of microamperes beam current. [11,17]

One modern design of small accelerators that has often been used in PIXE analysis, is a tandem accelerator (such as a tandem Van de Graaff). The tandem accelerator is popular for PIXE analysis due to allowing only half the voltage needed in the traditional (non-tandem) accelerator. Negatively charged ions from an ion source are injected under high vacuum into the accelerator acquire energy due to high positive voltage at the terminal center, called the high voltage terminal. In the stripping canal in the terminal, low-pressure gas is used to strip electrons from the negative ions, thus becoming positive. The positive ions will accelerate away due to the high positive voltage. A common tandem accelerator choice for PIXE analysis is 1.5 MV terminal voltage to provide 3 MeV energy for protons. [11,17]

The beam arriving from the accelerator will pass through the magnet, steers, slits for focusing on a target. The deflection in the magnet can change due to any small energy differences in the accelerator terminal voltage, so a feed-back system or highly regulated terminal voltage is required to provide stable beam energy. [11,17] This energy-analyzed beam is then directed axially down the beamline using electrostatic and magnetic steering elements.

There are two types of end stations in the PIXE technique, target in a vacuum chamber and target in air. In a chamber, the typical pressure is 10^{-6} Torr. A multi-place target design is put inside the chamber to avoid frequent opening and re-evacuation. The detector detects the X-ray emitted from the irradiated specimen, and a Faraday cup is used to observe the throughput beam current from the specimen.

The characteristic X-rays are emitted when the beam impinges a specimen. The detector transmits the detected X-ray data to a computer via the processing unit, amplifier, ADC, and MCA. This data represents by a spectrum by using a specific software program.

The X-ray spectrum comprises the characteristic X-ray lines simultaneously with a continuous background of the specimen's atoms. Figure 1.2 shows a PIXE spectrum that consists of the K_α, K_β peaks, and L radiation from elements. [6]

The bremsstrahlung is emitted by secondary electrons in the continuous background radiation below a few keV and the proton beam in a high-energy tail. The concentration of the element in the specimen is immediately related to the corresponding peak area. [5,15]

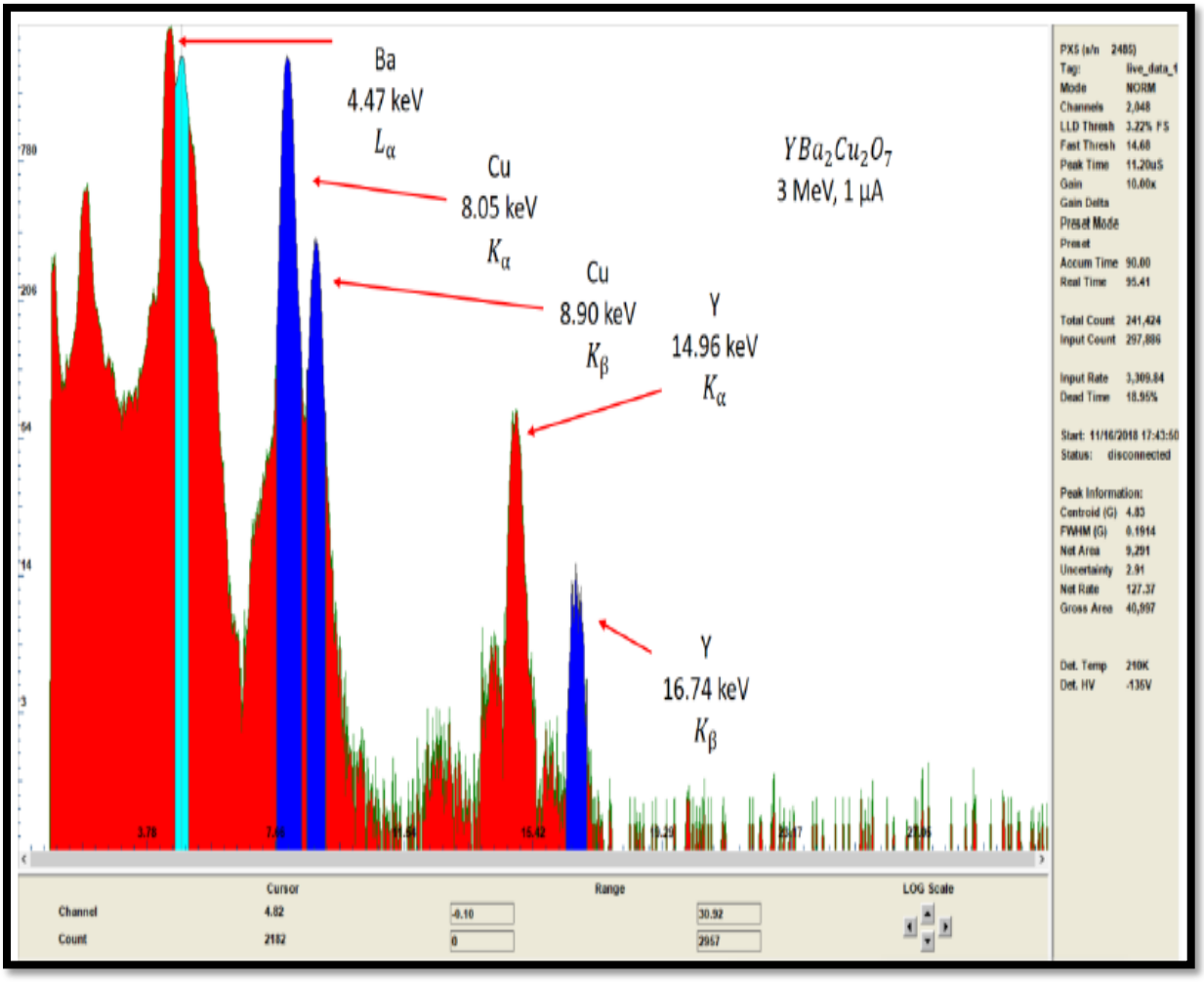

Figure 1.2: PIXE spectra. [6]

1.7 The Principle of Neutron Microbeam:

The neutron radiation effects on many occupationally exposed individuals at the energy facilities are reasons to study the neutron's low energy. [20,21] A neutron microbeam technical has been developed on existing microbeam systems to investigate human exposure to low-energy neutrons and search for the mechanism of neutron-induced bystander consequences.[20]

The 7 Li(p, n)7 Be nuclear reaction is a well-known source for generating neutrons. The near-threshold reaction produces a relatively high neutron yield and a narrow forwardly peaked angular distribution for the outgoing neutrons. [22] The narrow forward-peaked neutron microbeam is the product because the center of mass's velocity is greater than the outgoing velocity of the neutrons. The electrostatic lens system focuses on the incoming proton beam within a thin gold foil lithium fluoride layer. The back foil stops the proton beam, but the forward neutron beam passes through the back and radiates the cells. The back foil will also act as a vacuum window for the system. The neutron beam is restricted within a narrow forward solid angle, as shown in figure 1.3. [20]

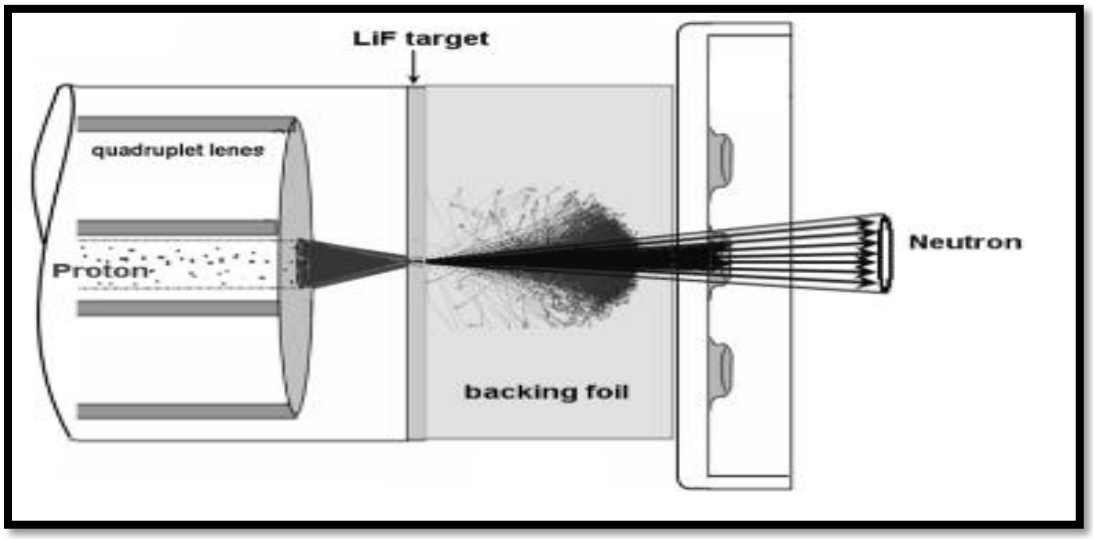

Figure 1.3: A schematic of setup for the neutron field.[23]

1.8 The Principle of The Proton-Induced Soft X-ray:

Soft x-rays are a well-distinguished sort of radiation that causes specific damage to DNA and cellular compositions.[24]

In recent years, it has come under single-cell studies among the advancement of soft x-ray microbeams. Soft x-rays cause damage in the same way as high-LET radiation does, but only in specific areas. The PIXE x-ray microbeam uses a reflection source, similar to most regular x-ray generators, where the produced x-rays are emitted from the proton incidence surface.

The bremsstrahlung background of the x-ray spectrum is significantly reduced when protons are used instead of high-energy electrons. A Fresnel zone plate chooses as the focusing x-ray optic of the PIXE soft x-ray microbeam. A zone plate is a diffractive optic be composed of concentric opaque and transparent rings that decrease as the radius increases.

Zone plates are restricted to monochromatic energy states. Proton-induced x-rays provide minimal bremsstrahlung generation and can be determined as a monochromatic source, as shown in figure 1.4. The focal length zone plate lens (f) given by: [25]

$$f = 4N \frac{\Delta r^2}{\lambda} \ldots. (1)$$

- The outside ring diameter (Δr)

- The number of rings (N)

- The wavelength to be used (λ).

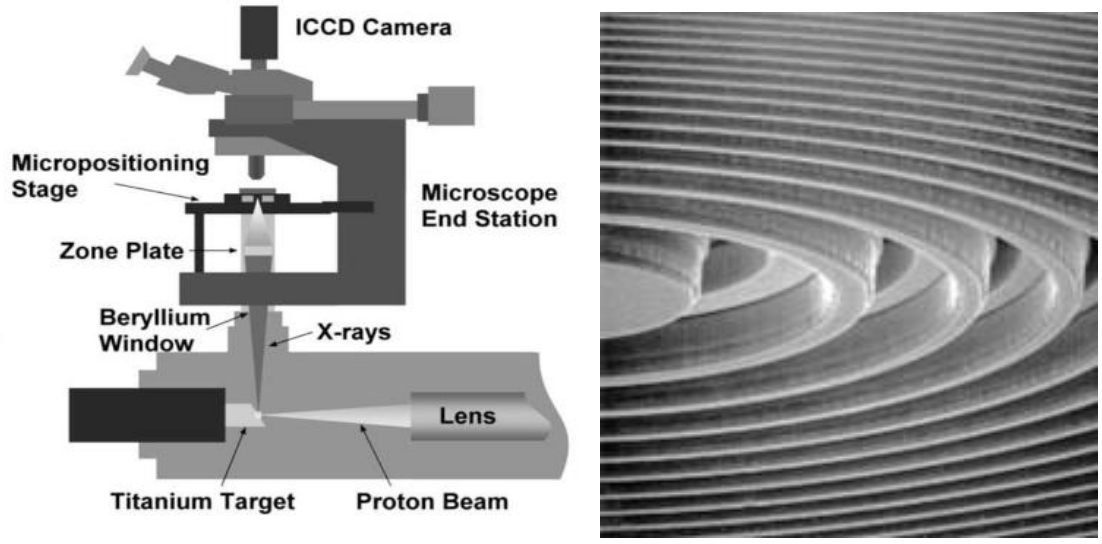

Figure 1.4: The x-ray microbeam end station and zone plate.[25]

1.9 Aims:

There are two primary aims of the project.

- The first aim is to provide a microbeam system with a single electrostatic quadrupole lens to get a micrometer-sized beam that can subsequently be used to produce a neutron microbeam, proton-induced x-ray emission (microPIXE), and proton-induced soft X-ray experiments, and single-cell irradiation experiments. The microPIXE measurements are demonstrated in this study.
- The second aim is to provide a broad beam for irradiation of in-vitro malignant tumor cells to assess cell killing by high linear energy transfer (LET) protons in an energy regime approaching the Bragg peak (maximum energy deposition).

Chapter Two
Theoretical Background

2.1 Charged-Particle interaction with matter:

A charged particle interacts with the nucleus or one or more electrons of an atom if it passes through it—this charged particle being surrounded by its coulomb electric force field. The incident particle interactions almost individually transfer small kinetic energy fractions, usually indicating gradually losing kinetic energy as the continuous slowing down approximation. Thus, the probability of interaction for a charged particle with the matter that passes through is zero.

A typical 1 MeV charged particle has approximately 10^5 interactions before losing all its kinetic energy.[27] The charged particle, known for its type and energy, is roughly characterized by a path length and traced to a specific medium. Each charged particle slows down due to a multitude of interactions that are undergone. So, the charged particle's path length tends to approach an expectation value called the range. Electrons have equivalent charges but obey a different path due to the scattering and do not move straight, mainly electrons, because of their small mass. [27]

The interaction of charged particles with material involves transferring energy from the charged particles to the material they travel. Charged particles passing through material continuously interact with the electrons and nuclei of the surrounding atoms. Charged-particle coulomb-force interactions can be characterized in terms of the relative size of the impact parameter (b) vs. the atomic radius (a).

Three types of interactions become dominant:

- Soft collisions ($b >> a$): The coulomb force field of a particle has an impact on the entire atom. An atom could be ionized or excited to a higher energy level by ejecting a valence electron. an atom of the absorbing medium receives a small amount of energy (~eV).
- Hard or knock-on collisions ($b \sim a$) – Interaction of charged particle with a single atomic electron (treated as free), which gets ejected with considerable kinetic energy. These secondary electrons are also referred to as binary-encounter electrons.
- Radiative (Bremsstrahlung) collisions ($b << a$) when the impact parameter of a charged particle is much smaller than the atomic radius, the Coulomb-force interaction occurs mainly with the nucleus. Figure 2.1 shows Soft, Hard, and Radiative collisions.[27]

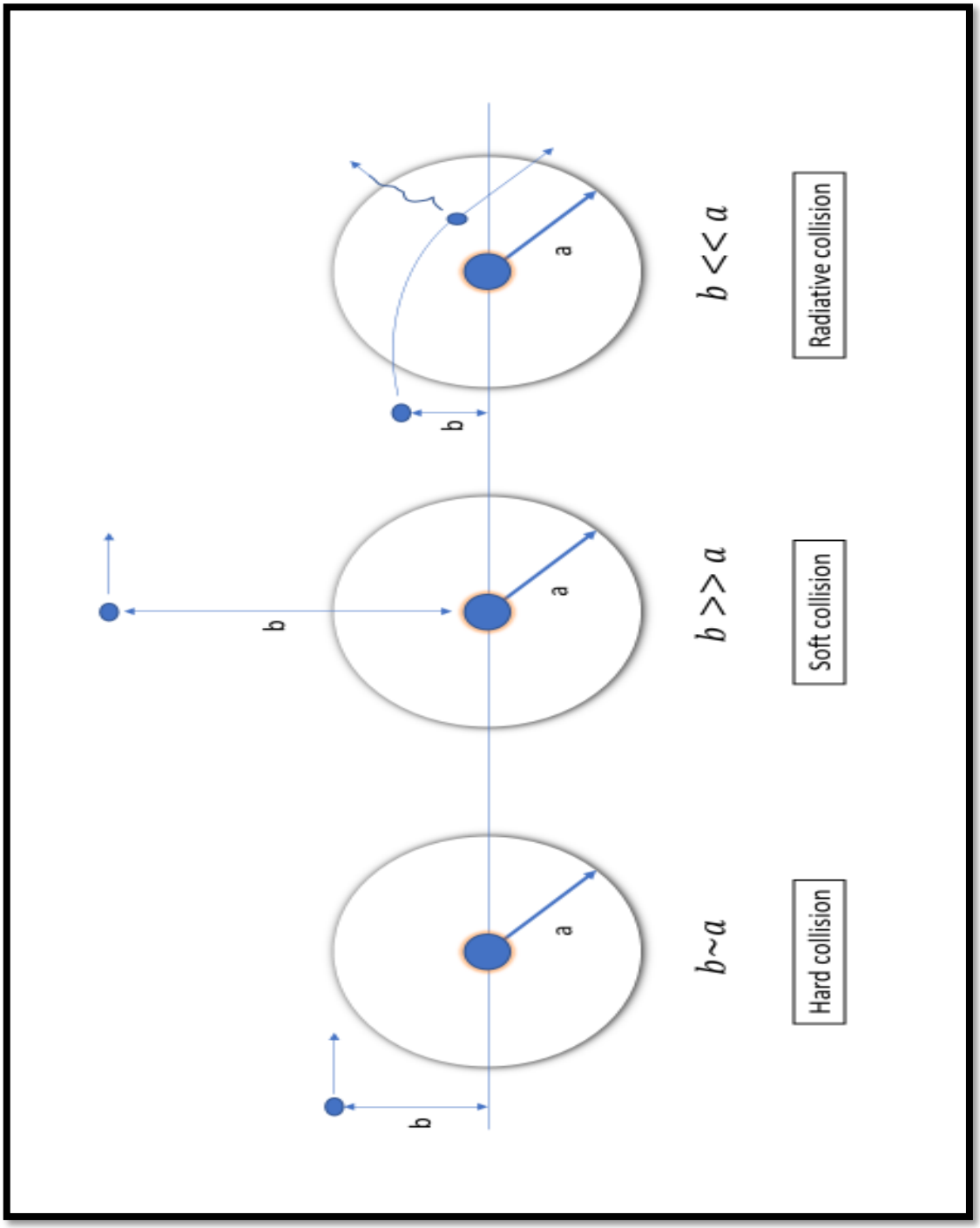

Figure 2.1: The charged particle Coulomb force interactions.

2.2 Stopping power:

The expectation value for a charged particle with kinetic energy T, which loses its energy per unit length in a medium with atomic number Z, is called stopping power see figure 2.2.[26] It is one of the essential phenomena because it measures a projectile's ability to penetrate a target. It divides into collision and radiative stopping power.

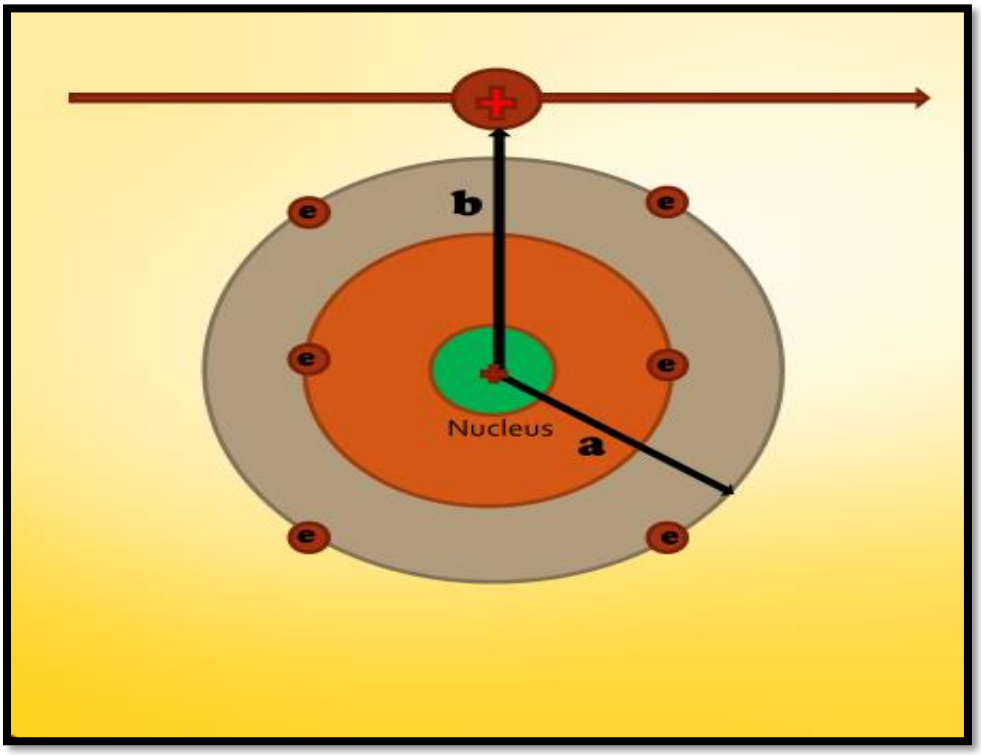

Figure 2.2: Essential parameters in charged particles colliding with atoms.

The stopping power for an addressed type of charged particle is specified by the outcome of the average energy loss per collision, Q_{avg}, and second the probability per unit distance of travel that an electronic collision happens the attenuation coefficient μ. [27]

$$Q_{avg} = \int_{Qmin}^{Qmax} Q\, W(Q)\, dQ \quad \ldots\ldots\ldots (2)$$

Thus, the stopping power is given by:

$$-\frac{dE}{dx} = \mu\, Q_{avg} = \mu \int_{Qmin}^{Qmax} Q\, W(Q)\, dQ \quad \ldots\ldots\ldots (3)$$

W(Q)dQ is the energy loss probability between Q and Q+ dQ for a given collision, and Q is the energy loss for each collision measured in eV. [27]

The mass stopping power ($S_{\circ}(E)$), is the stopping power divided by the material's density, measured in units of MeV/cm^2-g. It represents the rate of energy loss of the charged particle per cm^2-g of the target matter penetrated.[11]

$$S_{\circ}(E) = \frac{1}{\rho}\frac{dE}{dx} \quad \ldots\ldots\ldots (4)$$

The atomic stopping cross-section (MeV/ atom-cm^2) can give as:

$$\varepsilon_{\circ}(E) = \frac{1}{N}\frac{dE}{dx} \quad \ldots\ldots\ldots (5)$$

Where N is the atom density. From equation (1) & (2):

$$S_{\circ}(E) = \frac{6.022\times10^{22}}{A}\, \varepsilon_{\circ}(E) \quad \ldots\ldots (6)$$

A target's atomic number, Anderson, Zeigler, et al. [28,29], calculated stopping power depending on the theoretical and experimental data.

The charged particle range is the traveling distance before it comes to rest. The range in a target increases with decreasing energy loss per unit length traveling within the target.[27]

$$R(E) = \int_0^T \left(-\frac{dE}{dx}\right)^{-1} dE \quad \ldots\ldots\ldots\ldots (7)$$

2.3 Restricted Stopping Power:

The energy absorbed per unit mass into the irradiated material is referred to as the radiation dose. Therefore, absorbed energy plays the most significant role in dosimetry and radiation protection. The energy lost by a charged particle into a medium is determined by stopping power. This is not always equal to the energy absorbed in the target, mainly if the target is tiny compared to the secondary electron ranges produced. Many living cells have diameters of microns' order (10 – 4 cm) on the biological scale, such as the DNA double helix, which has a diameter of about 20 Å. [29] δ-rays with sufficient energy will easily escape from a small volume where the radiation particle has essentially lost most of its energy. The restricted stopping power is defined as a fraction of the collision stopping power, which includes soft and hard collisions that result in delta rays with more minor energies than the cutoff value Δ.[27] The restricted stopping power introduces an association between energy loss with the absorbed energy in a target. It is the linear rate of energy loss due to collisions. The maximum energy transfer to the secondary particle in the interaction is proportional to the incident radiation energy.[28]

$$\left(-\frac{dE}{dx}\right)_{\Delta} = \mu \int_{Q_{min}}^{\Delta} QW(Q)dQ \quad \ldots\ldots (8)$$

2.4 Linear Energy Transfer (LET):

In the early 1950s, the concept of linear energy transfer (LET) was introduced to describe the rate of energy deposited per unit distance across a charged-particle path. The terms LET and stopping power became synonymous. ICRU in 1960 identified LET as $-dE_L/dx$, where dE_L is the average energy locally imparted to a medium by a charged particle traversing a distance dx. It can usually be supposed then that the unrestricted stopping power implies.[28]

$$LET_{\Delta} = \left(-\frac{dE}{dx}\right)_{\Delta} \quad \ldots\ldots\ldots (9)$$

Direct action is the dominant process when radiations with high linear energy transfer (LET) are evaluated. The amount of energy transfer characteristic represents radiation's capability to cause biological damage.

Based on the amount of energy transferred per unit path length traveled, radiation is characterized as high linear energy transfer (high LET) or low linear energy transfer (low LET). High and low LET interactions can induce considerable DNA damage, resulting in a wide range of biological effects. Radiation can also generate free radicals when it reacts with molecules other than DNA, which can react negatively with the DNA molecule.

High LET radiation deposits its energy much more densely along the particle's path. As the particle nears the end of the track, it rapidly decreases and transfers its remaining energy to a small localized sub-region in the irradiated volume. Low LET radiation scatters energy more sparingly along its path across the irradiated volume. [56,57]

The Bragg Curve diagram shows (figure 2.3) the energy loss rate, or Linear Energy Transfer (LET), as a distance function through a stopping medium.

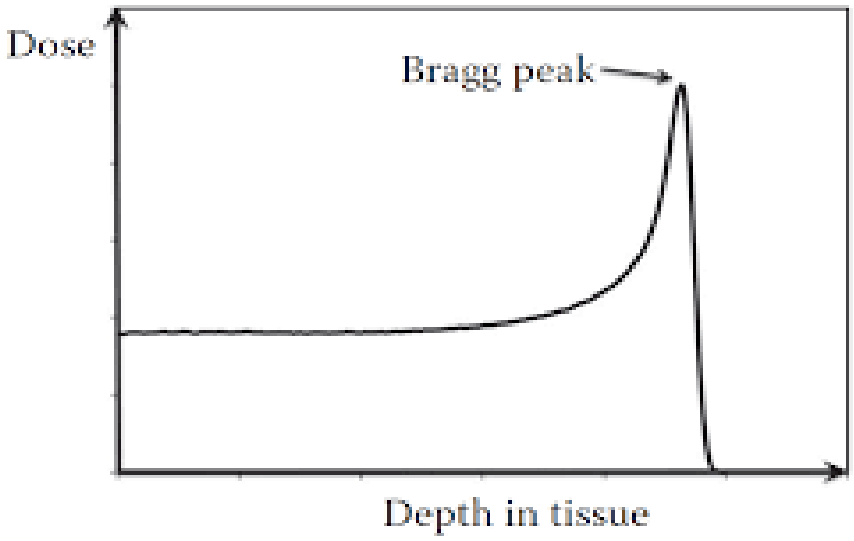

Figure 2.3: The Bragg peak

2.5 Charged-Particle Beam Dose Measurements:

The dose or dose rate in a charged particle beam must be measured in radiotherapy and radiobiological experiments. The current is proportional to the dose rate. The resulting depth dose curve has reversed the mass stopping-power curves for monoenergetic particles of a given kind, such as protons. [28] In the Bragg peak region, near the end of the particle range, the dose rate achieves its maximum. The dose rate at a given depth of x can be calculated using a uniform parallel beam of monoenergetic charged particles typically incident on a tissue slab with a fluence rate measured in cm^{-2} s^{-1}. A thin disc-shaped volume with thickness x and an area A normal to the beam is assumed along the beam's central axis. In the volume element, the rate of energy deposition is: [28,34]

$$\textbf{The rate of energy deposition} = \varphi^{\cdot} A \left(\frac{-dE}{dx}\right) \Delta x \quad \ldots\ldots (10)$$

(–dE/dx) denotes the beam particles' collisional stopping power as they traverse the slab at depth x.

The dose rate $(D^{\cdot})$ is determined by dividing the mass $(\rho\ A\ \Delta x)$ of the volume element with its density, where ρ is the tissue density: [28,34]

$$D^{\cdot} = \frac{\varphi^{\cdot} A\ \Delta x \left(\frac{-dE}{dx}\right)}{\rho\ A\ \Delta x} = \varphi^{\cdot} \left(\frac{-dE}{dx}\right) \ldots\ldots (11)$$

The dose per unit fluence equals the particle's mass stopping power at that depth for a particular depth. For example, whenever the mass stopping power equals (4 MeV. cm^2 /g), the dose per unit fluence can be represented (4 MeV/g). If significant nuclear interactions, such as high-energy protons, equation (13) cannot measure accurate depth dose curves and then use Monte Carlo calculations to predict the individual incident and secondary particles' results cross-sections various nuclear interactions that can occur. [27,33]

2.6 Radiation chemical and biological effects:

Ionizing radiation causes chemical changes in liquid water, which have biological implications. The water makes up 70–85% of mammalian cells, including 10–20% proteins, 10% carbohydrates, and 2–3% lipids. Secondary electrons are abundant in the matter because of ionizing radiation. The secondary electrons mainly produce in water with energies in the range of 10–70 eV. The secondaries slow down rapidly $\leq 10^{-15}$ s to sub excitation energies, energies lesser the threshold for producing electronic transitions ~7.4 eV for liquid water. Radiation causes ionized and excited molecules, H_2O^* and H_2O^+, and free sub-excitation electrons in the local regions. The standard, diffusion-controlled chemical reactions within and around a charged particle's path begin 10^{-12} sec after the particle passes through. Radiation-induced changes produce the three initial species during the pre-chemical period, ranging from ~10^{-15} s to ~10^{-12} s. [28,34]

- First: an ionized water molecule reacts with a neighboring molecule in around 10^{-14} sec, producing a hydronium ion and a hydroxyl radical:

$$H_2O^+ + H_2O \rightarrow H_3O^+ + OH. \ldots\ldots\ldots (12)$$

- Second: an exciting water molecule becomes cleared of its energy by losing an electron, becoming an ion, and continuing by reaction (14) or molecular dissociation. The water molecule's vibrational intervals are ~ 10^{-14} s, which is the time that characterizes the process of separation:

$$H_2O^* \rightarrow \begin{cases} H_2O^+ + e^- \\ H + OH \end{cases} \ldots\ldots\ldots\ldots (13)$$

- Third, the sub-excitation electrons emigrate, lose energy by vibrational and rotational excitation of water molecules, and become thermalized by ~10^{-12} s. The thermalized electrons orient the permanent dipole moments of neighboring water molecules, forming a cluster called a hydrated electron:

$$e^{-} \rightarrow e_{eq}^{-} \text{ …….. (14)}$$

Due to their unpaired electrons, the chemically active species OH. $^{-}$, H_2O^{+}, and (e_{eq}^{-}) are reactive. These radical species are also recognized as free radicals, and they are capable of causing biological damage. These free radicals cause an excellent distribution of DNA damage because cells are made of 80% water; basically, two-thirds of the DNA damage at cells are exposed to ionizing and non-ionizing radiation, particularly low LET. [28,34]

Radiolysis may occur when sufficient energy radiation enters a volume of water. Radiolysis is when a molecule absorbs energy from incoming radiation, and one or more molecular bonds are broken, resulting in reactive species. If the incoming radiation releases an electron from a neutral water molecule, rather than dissociation of the molecule, a diversity of radicals may be generated, which can either interact and damage DNA directly or react with other nearby molecules, producing other reaction species with a longer life, that can then interact with DNA and damage the surroundings. Reactive oxygen species are the general refer to these radicals.[35] When cells are exposed to high LET (> 4 keV/μm) radiation (protons, neutrons, heavy ions), direct damage is the fundamental cause of cell death. [34,36]

Direct DNA damage caused by high LET radiation is hard to repair, and the operation is difficult to modify chemically or physically. Chemical reactions with free radicals because indirect damage produced at radiation interaction with biological material, such as when an O.H.- radical attacks a DNA sugar and causes a single-strand break. A single radiation track could result in double-strand breaks produced by high and low LET radiation or various breaks due to radiation close to the break termini (between 6 and 10 base pairs). [34,36] The biological effects of radiation can differ significantly depending on the dose, type of radiation, and timeframe observed. Some effects are instant, while others take years to occur. These effects are generally classified as stochastic or non-stochastic. Cancer is an example of an effect in which there is no specific determination that it will occur. Many individuals can be exposed to radiation; however, not everybody will develop cancer during their lifetime.

As cancer can occur without exposure naturally, no radiation exposure is expected to cause cancer incidence. The probability of cancer increases as the dose of radiation increases, and there is no dose where there is no threat of developing cancer. Ionizing radiation can cause fewer responsibilities, genetic effects, and mutant offspring due to stochastic effects.

In comparison, non-stochastic effects have a direct causal effect with dose and a threshold dose. Cataracts, skin erythema, infertility, and acute radiation syndrome are deterministic biological effects of ionizing radiation. Acute radiation syndrome may develop when exposed to a large sufficient short-term whole-body dose of radiation. This leads to rapid exhaustion of blood and digestive tract radiosensitive cells, which might cause infection, damage to the bone marrow, organ and tissue damage, or even death at high doses. [28,37]

Chapter Three
Experiment and Method

3.1 Overview of L-15 experimental design:

In the ECU Accelerator Laboratory, ion beams are created with energies up to 8 MeV. The ion beam must be generated, analyzed, focused, accelerated, controlled, and then focused through a high vacuum environment before it ever approaches an experimental target. The L-15 beamline has been developed in this study to be a horizontal multi-purpose proton beam system. It has a single electrostatic quadrupole quadruplet focusing lens brought from NCE. Due to its high particle fluence, this beamline will be used as the primary beam for microPIXE, soft-X-ray microbeam analysis, neutron microbeam, and broad-beam proton cell irradiation experiments.

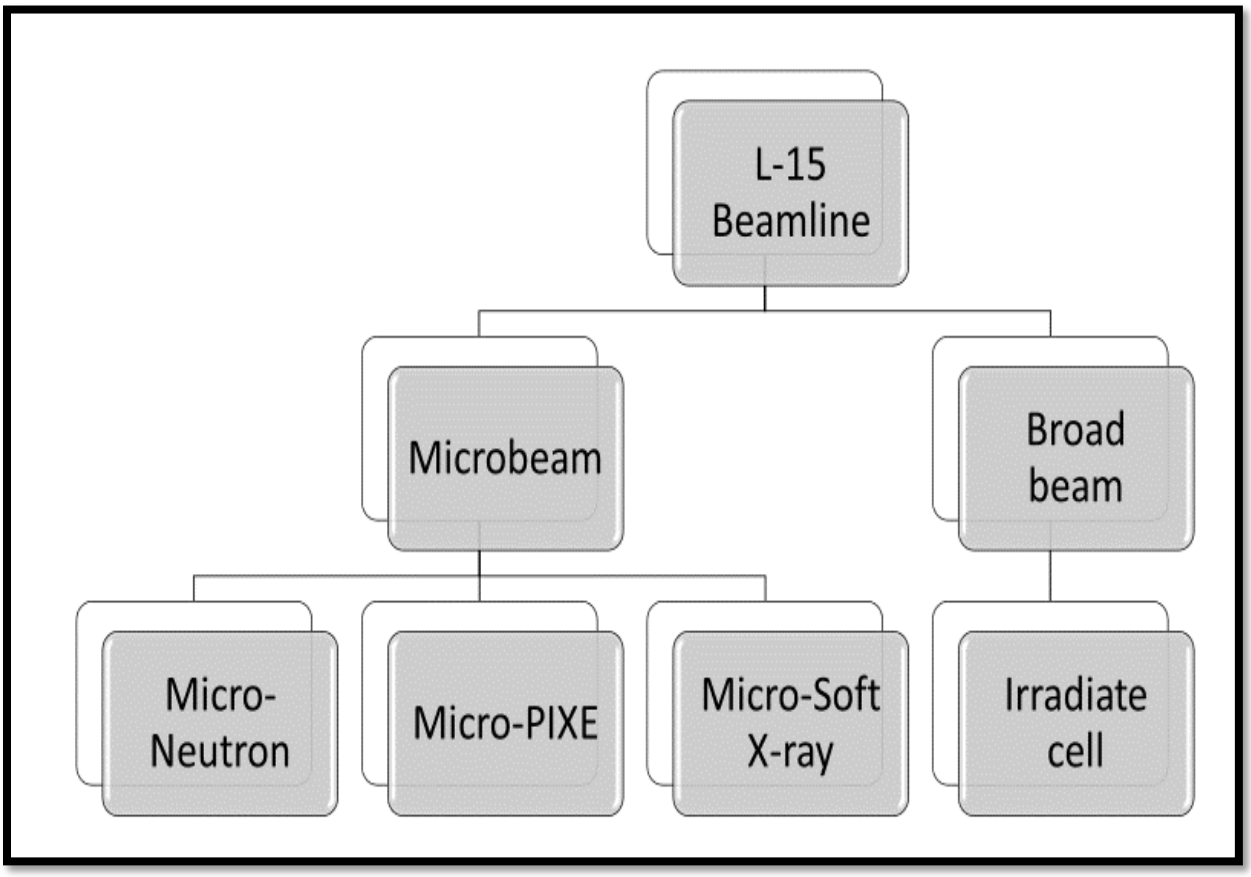

3.2 Proton Beam Creation using Pelletron accelerator:

A 2 MV tandem Pelletron accelerator can generate ion beams with different energies and charging states to search for irradiation effect and its analysis at East Carolina University accelerator laboratory. The ion beam facility consists of several component systems to deliver ion beams to specified targets. Therefore, it is appropriate to start with a consideration of how an ion beam is created. At East Carolina University, a horizontal multi-purpose microbeam and broad-beam system have been developed with a single electrostatic quadrupole quadruplet focusing lens. It has been combined with the 2 MeV tandem Pelletron accelerator to generate a micrometer-sized beam and broad-sized beam for cell irradiation research. It will also be used as the primary beam for a microPIXE (particle-induced x-ray emission) and neutron microbeam experiment, as shown in figure 3.1.

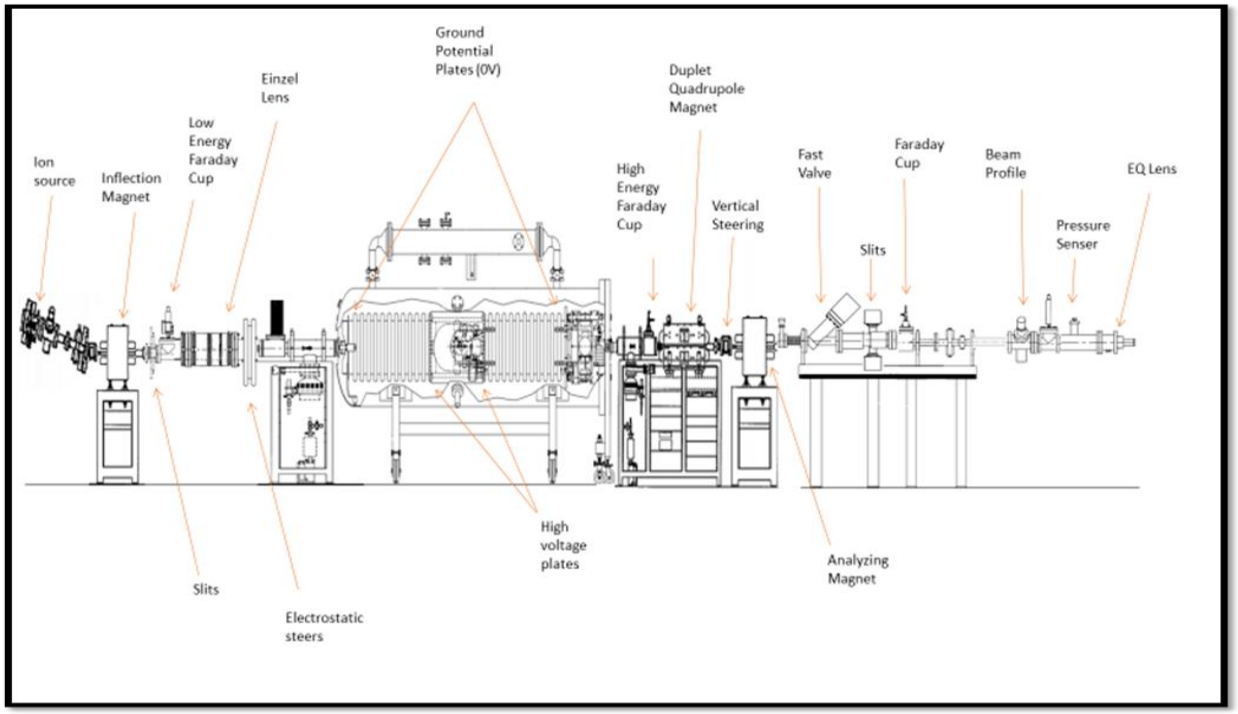

Figure 3.1: Diagram of the ECU's particle accelerator and L-15 beamline.

3.2.1 The Ion Source:

The ion source is the negative ion source of a Middleton pattern cesium sputter. See figure 3.2. A cesium reservoir is heated to vaporize a tiny cesium quantity that flows through a canal to the ionizer for this source. An electrical current flowing through the ionizer produces sufficient energy from the neutral cesium vapor to release an electron, creating one free electron and Cs+, which is attracted to the negatively charged cathode.

While this process occurs, atoms are removed from the solid target, creating collision cascades within the target matter due to the transfer of momentum between the energetic particles and the target atoms. Unless the particle has energy above the surface binding energy, atoms are freed from the material upon recoil of those cascades and upon arrival at the target surface. [6,38,41]

The heavy cesium ion is preferred over many other elements as a large amount of momentum is required for the reaction to occur. Besides, cesium has an abundance of free electrons available to be given to the sputtered atoms. The ion source, except noble gasses, can generate ions from almost all elements and can reach currents in the range of 100s of microamps.

East Carolina University uses the 860 A cesium sputter ion source, which Middleton founded in the early 1980s, as a high-Intensity from General Ionex Corporation. The generating proton beam (H^+) requires creating negative Hydrogen ions (H^-) with the source. [39,40,41]

A tiny amount of Titanium Hydride (TiH_2) powder is tightly packed into a copper target cathode to conduct this. The cathode is 12.5 mm long and 10 mm wide with a front cone-shaped 1.6 mm well penetrated 5mm into its center. As solid cesium is heated in an oven set at around 350 K, the sputtering process occurs.

The cathode is kept at a lower temperature so that more of the cesium vapor is condensed. By thermal emission, cesium vapor is ionized on the other side of the chamber when the tantalum coil boils electrons from the cesium vapor by thermal ionization. [6,41]

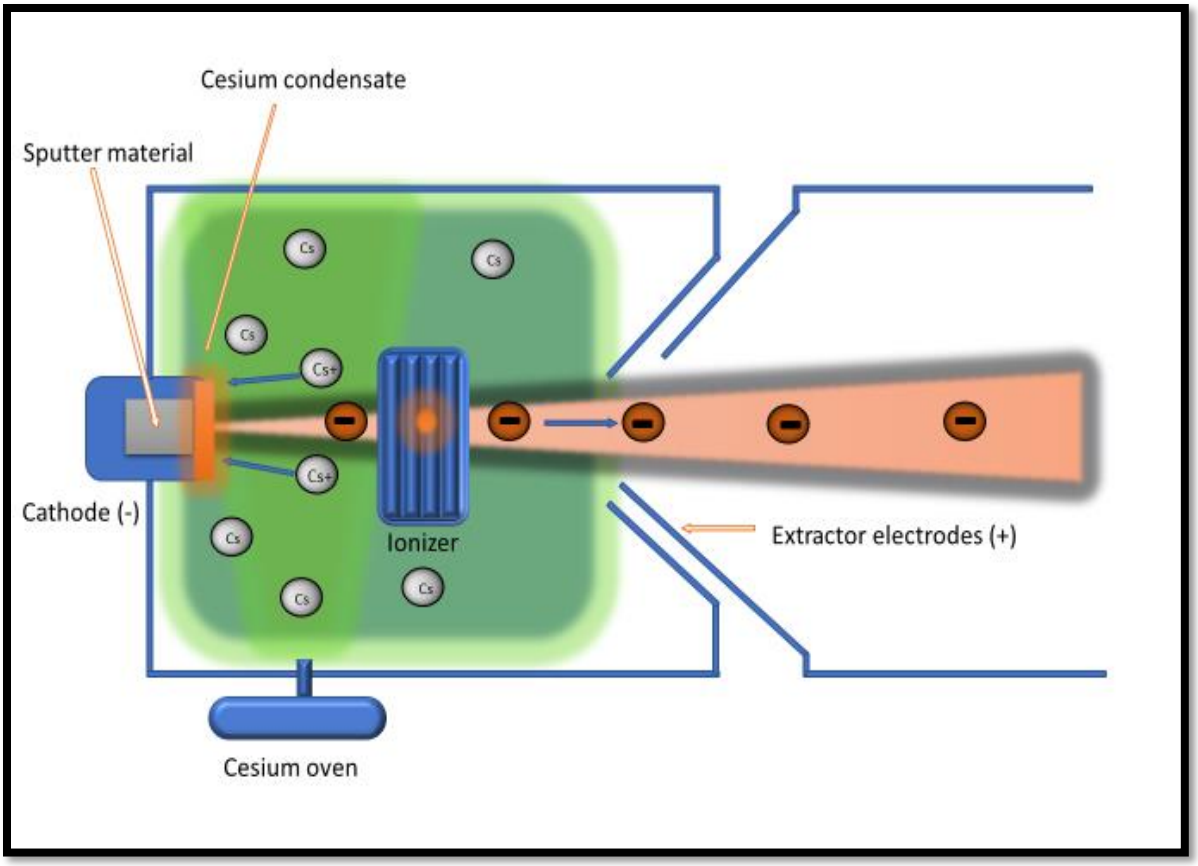

Figure 3.2: Diagram of Cesium sputter.

The positively charged cesium ions are accelerated through a potential difference and forced to bombard the cooled and negatively biased sputter cathode, while the cesium vapor is changed to a positive ion. Various molecular sorts are sputtered from the Titanium Hydride (TiH_2) due to bombarding positive cesium ions into the cathode sputter after ionized cesium is accelerated through the potential difference. [6,41]

Several of these sputtered particles are atoms that convert negatively charged when they collect electrons after collisions with cesium atoms previously condensed on the cooled surface of the cathode. The recently produced negatively charged ions accelerate away from the cathode while the cathode is maintained at a negative potential.

Utilize extractor electrodes maintained at a higher cathode voltage potential; consequently, at this point, the ions have approximate energy of several keV.

An Einzel lens consisting of connected conduction cylinders concentrates the H^- ions alternately at a high voltage and ground potential.

The resulting electrostatic fields deflect the beam, and the accelerating voltage then accelerates the H^- ions. The H^- ions pass via an inflection magnet after they leave the source. The inflection magnet is a dipole electromagnet with its coils oriented so that the resultant field is orthogonally turned into an ion beam trajectory, as shown in figure 3.3.

Therefore, the trajectory of the ions can be twisted around a radius predicted by the Lorentz power. [6]

$$F_L = q\,[E + (v \times B)] \quad \ldots\ldots\ldots\ldots\ldots\ldots\ldots\ldots\ldots\ldots \quad (15)$$

The Lorentz force is exercised on a charged particle q moving with velocity v through E and magnetic field B.

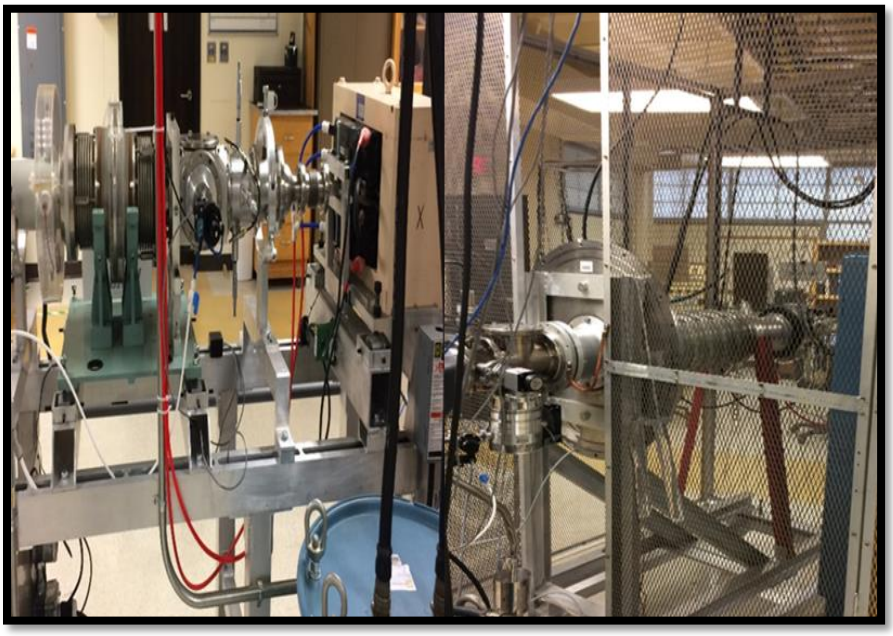

Figure 3.3: Ion source and collimation system at ECU accelerator lab.

The magnetic field's magnitude is controlled by modifying the current passing through the coils, allowing the operator to adjust the ion's path's curvature's radius and choose the wanted negative ion to inject inside the accelerator. The beam current in the low energy beamline measures using the remotely Faraday cup can provide feedback on the ion beam intensity to the operation control station.

The Faraday cup readings monitoring allows the best adjustment to the voltage of the Einzel and the current of the Inflection magnet to make sure the ion beam is accurately focused. The beam is focused by another Einzel lens exceeding the Faraday cup and could be deflected by a set of low energy steerers.

The low energy steerers contain sets of parallel horizontal and vertical plates. An electric field formed by the plates' charge will deflect the ion beam and direct it along the beamline by adjusting the plates' voltage. The beam will be deflected and focused with a set of low energy steerers and another Einzel lens, respectively. An electric field provides by the plate's charge can deflect and lead the ion beamline via manipulating the plate's voltage.

A Turbomolecular pump into the low-energy beamline reserves the necessary high-vacuum circumstances. In addition, the gate valve provides insulation between the low-energy beamline and the accelerator so that other sections will keep under vacuum conditions during maintenance.

3.2.2 Pelletron Tandem Particle Accelerator and the High Energy Beamline:

East Carolina University has a Tandem 6SDH-2 Pelletron model 2AA072310 accelerator from National Electrostatics Corporation. It can accelerate various ion species over a wide range of energies for backscattering, proton-induced x-ray emission (PIXE), implantation, and nuclear physics applications accelerator comprises a high voltage insulating support structure, a high voltage generating charging system, and an evacuated acceleration tube into which the ion beam flows. [42]

The accelerator's center is the high voltage terminal, with low energy and high energy acceleration tubes on each side. Negative ion beams generated in a negative ion source are pre accelerated to subtle energies before injecting inside the accelerator. The beam enters the accelerator's low energy beamline, where the negative ions are attracted to the positively charged high voltage terminal will accelerate. [42]

The name of the Pelletron is taken from the chain that is fundamental to its operation. The construction of the Pelletron chain is superior to the charging belt. It makes for a more consistent charging distribution, allowing for increased terminal voltage balance and providing more stable particle energy. The chain of Pelletron consists of ties of metal pellets coupled with electrically isolating nylon connections. The charging mechanism starts as electrons are forced away from the metal pellets by the negatively charged inductor electrode when connected to the grounded drive pulley electrically. [42]

The negative ions enter a system known as the stripper within the terminal, where the ions are stripped of 2 or more electrons and converted to positive ions. The high voltage terminal repels and accelerates these positive ions as they leave the stripper and drift through the accelerator's second stage. This simultaneous acceleration provides singly charged ions with double the energy they can gain in a single-stage accelerator with the same terminal voltage, resulting in ions with a charge state n final energy (n+1) eV, where e is the electronic charge, and V is the terminal voltage. The 6SDH-2 accelerator is housed in a pressure vessel that was designed especially for it. [6,42]

The insulating gas sulfur hexafluoride (SF_6) is essential for optimal operation, and the tank's function is to store it. It also has a total vacuum rating, which is beneficial for gas transfer. SF_6 is a non-toxic, chemically stable gaseous dielectric that serves as a superior electrical insulator. The ECU's accelerator uses this gas to avoid corona discharges; arcing creates an unstable terminal voltage, contributing to internal component destruction. [6,42]

SF_6 provides excellent electrical insulation with a very high breakdown voltage, nearly triple that to air at standard temperature and pressure (STP). By pressurizing the gas, the breakdown voltage of SF_6 is raised even further. Care is taken to fully seal the ion beam tubes from the high-pressure SF_6; if the SF_6 pressure is too great, it may leak into the beamline vacuum. As a result of collisions with the SF6 molecules in the beamline, the ion beam will become scattered. In the accelerator

tank, the SF_6 heats up as used typically. Since an increase in the insulating gas's temperature reduces breakdown voltage, a water-cooling system controls the insulating gas's temperature. [42]

When a negative H ion beam enters the stripper gas assembly, it undergoes electron stripping. After being exposed to nitrogen gas, the negative ion beam becomes a positive ion or proton (H^+) beam. In the next acceleration step, the newly established proton beam is accelerated away from the positive terminal. That indicates the singly charged H ion will gain 2 MeV of energy during the first stage of acceleration because the terminal was changed to have a potential of 2 MV. The proton gains a further 2 MeV of energy during the second acceleration, with cumulative proton energy of 4 MeV as it emerges from the accelerator. [6]

The positive ion beam enters the high-energy beamline after exiting the accelerator. Like the low-energy beamline, another turbomolecular pump pumps this beamline down to the required vacuum level. The H^+ beam is focused on this segment of the beamline as it runs through a set of quadrupole electromagnets. The beam then passes through another set of electromagnets to provide vertical H+ beam steering before flowing through the analyzing magnet.

The analyzing magnet is a large dipole electromagnet that chooses the desired ions based on the ions' charge, mass, and energy. The magnetic field provides a simple means of using the charge-to-mass ratio and the velocity of each particle to steer it in the desired direction, only if it is a proton and only if the proton is moving at the desired velocity because the beam generated that so far does not be composed entirely of protons with the desired energy.

This process picks protons with the proper energy for an operation. Then the analyzing magnet (called a switching magnet) steers the beam to the beamline where the experiment is managed. It provides the beam, ensuring that the only charged particles that eventually arrive at the cells are protons, including the accurate energy.

3.3 The L-15 Beamline:

The proton beam enters the L-15 beamline through the gate valve and "fast valve." The L-15 beamline indicates beamline 15 degrees off the central (zero-degree) straight-through beamline. The valves isolate the L-15 beamline from all other beamline segments when it is not in operation.

3.3.1 Fast valve:

A fast-closing gate valve from National Electrostatics Corporation (NEC) is equipped with a pair of springs, a latching mechanism, and a solenoid trigger for quick operation (see figure 3.4). The result is a valve that closes and seals in less than 35 milliseconds when a pressure sensor operates the solenoid. This valve protects the accelerator or vacuum system from sudden exposure to atmospheric pressure due to vacuum window failure.[43]

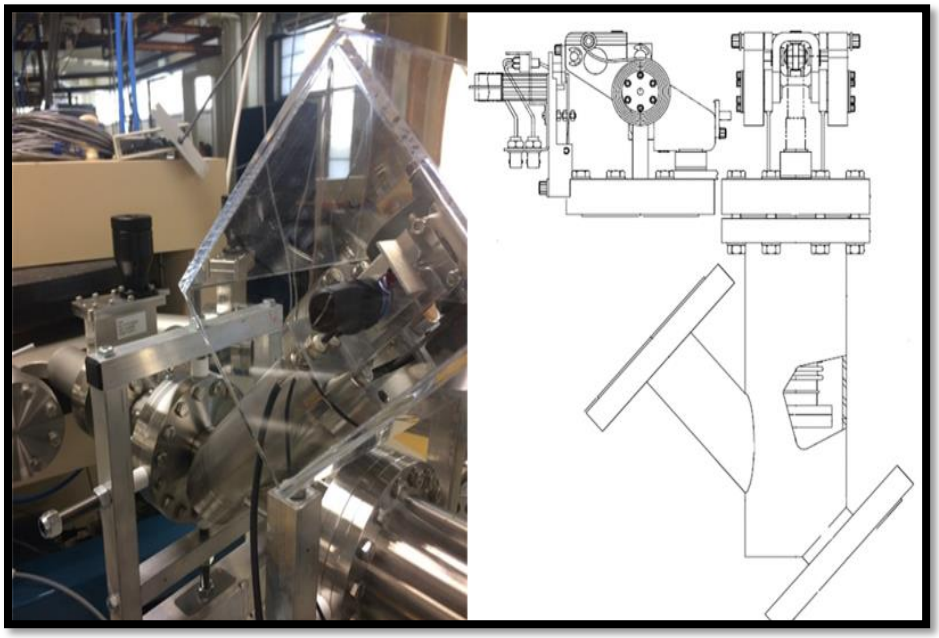

Figure 3.4: The gate and fast valve on the L-15 beamline. [43]

The handle of the fast valve is encased in an open position by a special valve handle. The solenoid (with very low inductance) receives a high voltage pulse from the pressure sensing circuit in an accident. It, therefore, acts as a hammer that knocks the latch arm out of position and releases the handle.

The springs compressed in the cocked position accelerate the handle through 180° such that the resulting momentum provides sufficient impact to push the valve seat against the knife edge and produce a tight seal. The trigger solenoid is rated at 12 volts, 3.6 ohms, 3.7 amps pulsed operation. The discharge of a capacitor can operate this. A 40 μfarad capacitor charged to -300 volts runs excellent with a low duty cycle for fast operation.[43]

3.3.2 Slit:

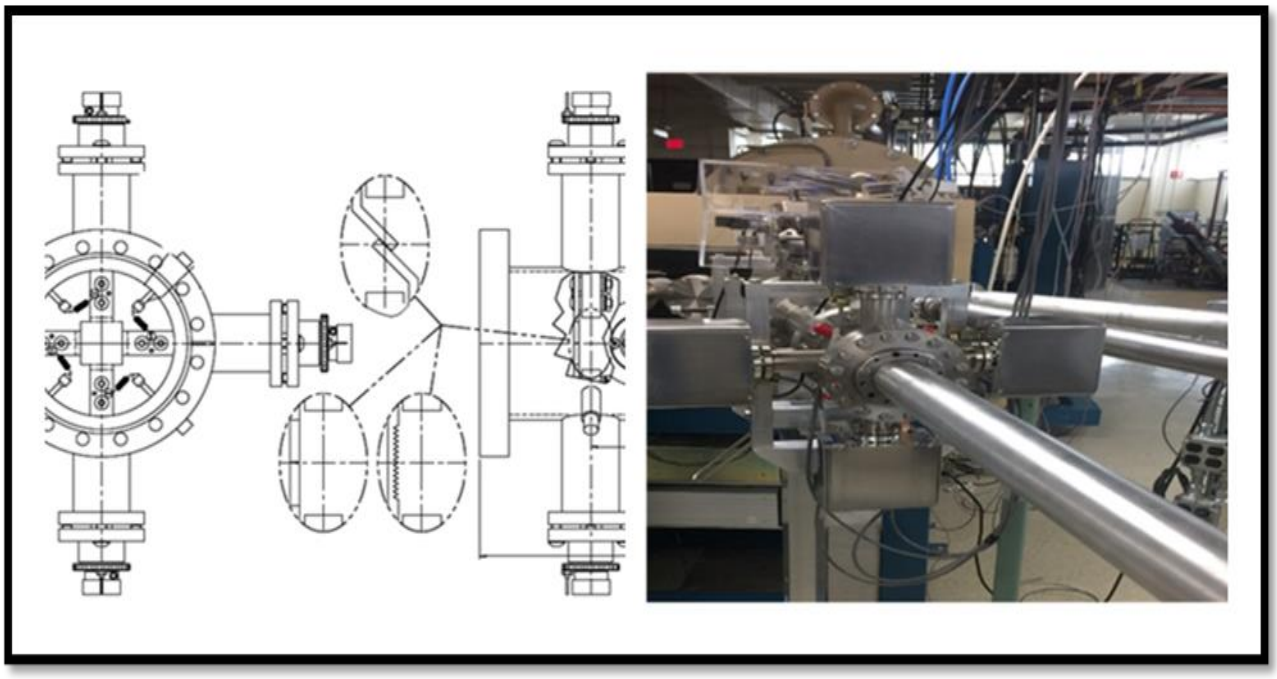

Figure 3.5: The slits on the L-15 beamline. [44]

NEC slits (figure3.5) are suitable for applications that involve precise beam size control, beam divergence determination, or beam current limitation. The NEC line of slits is intended to use the injection and high-energy beamlines of medium-to-high-current or high-energy electrostatic

accelerators. Combined with NEC's Terminal Potential Stabilization systems, they are also widely used for ion beam energy management.

The NEC line of slits is ideal for a wide range of applications for controlling ion beam energy, current, or scale, with power ratings ranging from 50W to 1000W. The NEC BDSR7 and BDSR8 slits are remotely operated metal and ceramic slit systems. The beam is described in the -X, +X direction by one of the two pairs of slit components and the -Y, +Y direction by the other pair. [44]

3.3.3 Steers:

The NEC magnetic ion beam steerer at ECU's L-15 beamline is regularly used with Pelletron accelerators to achieve simple deflection of proton beams with energies ranging from 2 to 3MeV. In addition, this simplistic, compact steerer is excellent for adding ion beam directional control to existing 2" or 4" O.D. beamlines.

Two X-Y steering units are required, as shown in figure 3.6. The control in one direction is possible for each unit independently. The magnetic pole separation is appropriate for clarity over a marginal 2" or 4" stainless steel tube.

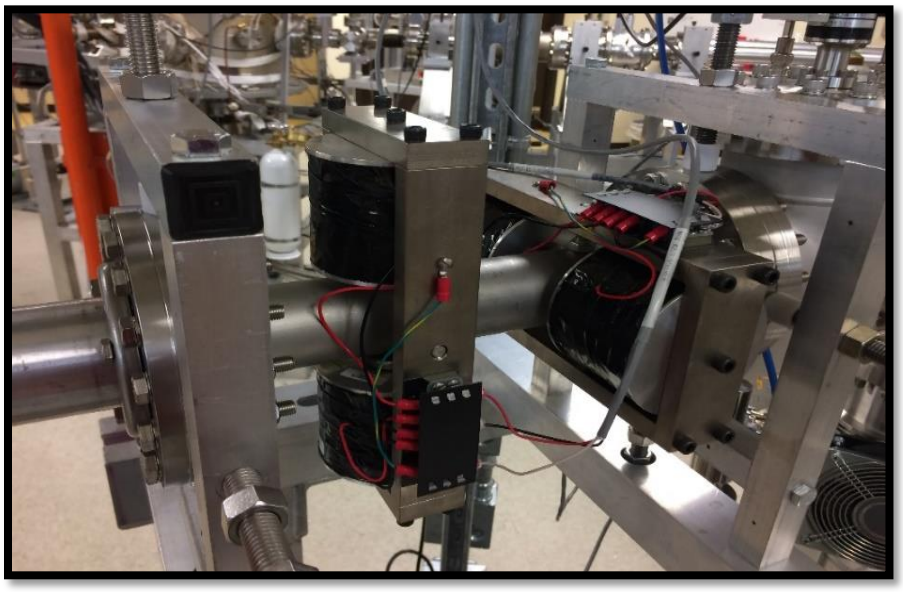

Figure 3.6: The ECU's magnetic ion beam steerers for use on stainless steel beam tubes.

3.3.4 EQ Lens:

The discipline of electron optics describes the creation, propagation, and focusing of electron and ion beams. The term electron lens refers to a device that manipulates charged particle beams using electric and-or magnetic fields, with the term electron referring to any charged particle. There is a relative analogy between light rays and charged particle beams, as indicated by the concept of optics. Charged particles, like light rays, can be reflected, refracted, and focused. As a result, an electron optical system should be capable of being characterized using light optics concepts. Electron lenses can be governed by the same rules and principles that govern light optics. Snell's law is another essential optical law that demonstrates the similarity between light and electron optics.[58] The path of a charged particle traveling with uniform velocity w through a space of constant potential V, then passing a potential stepping into a space of constant potential V", will be suddenly altered, as shown in figure 3.7.

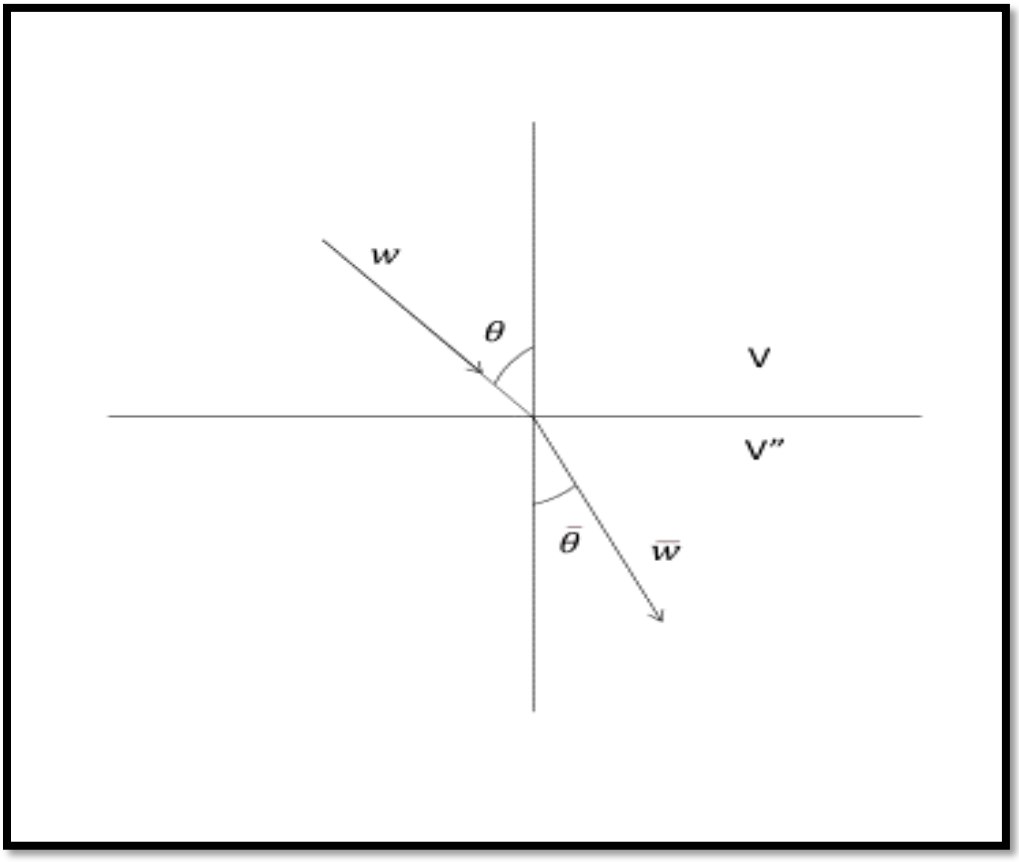

Figure 3.7: The path of a charged particle traveling with uniform velocity.

Since the tangential component of w_x will continue unchanged so that $w_x = w_x'$.

$$\sqrt{\frac{V}{V''}} = \frac{\text{Sin}\,\theta'}{\text{Sin}\,\theta} = \frac{w}{w'} \quad \ldots\ldots\ldots (16)$$

The electron path across the field consequently coincides with the path of a light ray incident at an angle of a media whose refractive index is in the ratio $\sqrt{\frac{V}{V''}}$. [58]

The electrostatic lenses are constructed of two or more elements isolated by a small gap through which various voltages are applied. The equipotential lines around the gaps between the elements will be curved, analogous to a glass lens's curved surface. The curved equipotential forces a charged particle's path to bend, exactly how a light ray's path bends when encountering a glass lens. The electrostatic lens is an instrument for the transportation of charged particles. Electrostatic lenses can, therefore, readily magnify the electron trajectories or converge them.[58]

The electrostatic quadrupole quadruplet lens with a 2.25 mm aperture and a ± 5 kV element voltage rating is the EQQ5.5-5 lens on ECU L-15 beamline NEC. 2.0 mm is the diameter of the entrance aperture, as shown in figures 3.8 and 3.9. As a quadrupole singlet behaves as a converging lens in one plane and a diverging lens in the other, the quadruplet's focusing properties are particularized in terms of these two planes: the CDCD (converging-diverging-converging-diverging plane) and the DCDC (diverging- converging-diverging- converging plane).

The ECU lens is asymmetric quadruple. The first and fourth singlets are physically like the second and third singles. Voltage allocations are the same for the first, fourth, and second and third singlets; furthermore, they are rotated at 90°. The central lens elements are almost twice the end lens elements, physically.[45]

The focal length of a quadrupole singlet produces by:

$$f_c = \frac{1}{K \sin LK} \quad \text{Converging plane} \ldots\ldots\ldots\ldots \quad (17)$$

$$f_d = \frac{-1}{K \sinh LK} \quad \text{Diverging plane} \ldots\ldots\ldots\ldots\ldots \quad (18)$$

Where L is the element length and K is a parameter that characterizes the lens strength and is given for the electrostatic case by:

$$K^2 = \sqrt{\frac{Nv}{A^2 \emptyset}} \quad \ldots\ldots\ldots (19)$$

Where:

N: is the charge state of the particle.

v: is the absolute value of the voltage on the singlet elements.

A: is the aperture radius.

∅: is the potential drop-through in which the incoming particle has been accelerated.

The microprobe lens is designed to compose the same position on an analysis end-station where a beam collimator will usually be. Most microprobe systems necessitate a long object distance and a short image distance.[45]

The NEC recommended for demagnification the beam size that a target has located about 4.2 m from the object with the image position at 152 mm beyond the lens exit. The object is formed, including a micro-quad aperture segment containing four accuracy drilled apertures of various sizes. The lens setup has focused 3 MeV proton ions on a beam spot in the air or specimen with a few mm or um diameter. The quadrupole electrodes can resist voltages high enough to focus protons ions. [45]

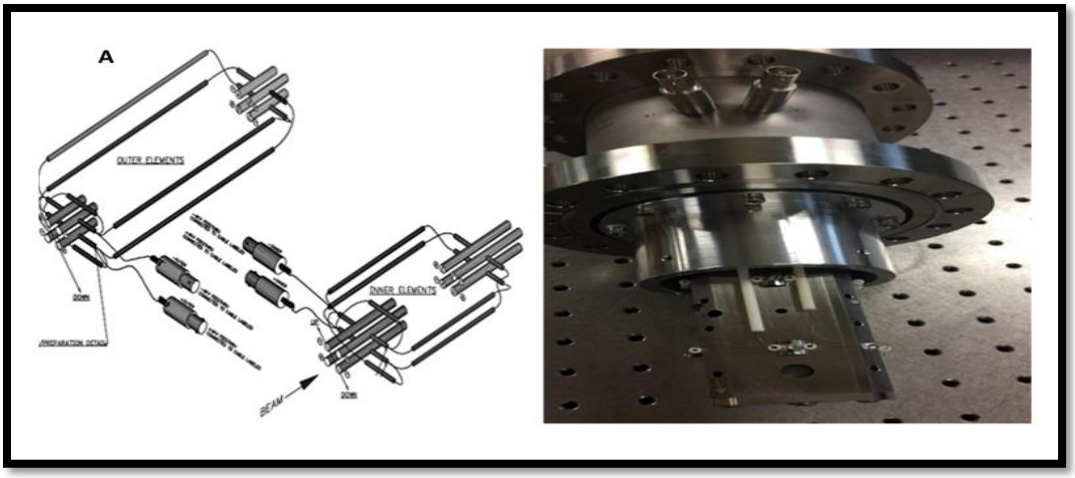

Figure 3.8: The ECU's electrostatic quadrupole quadruplet from NEC.

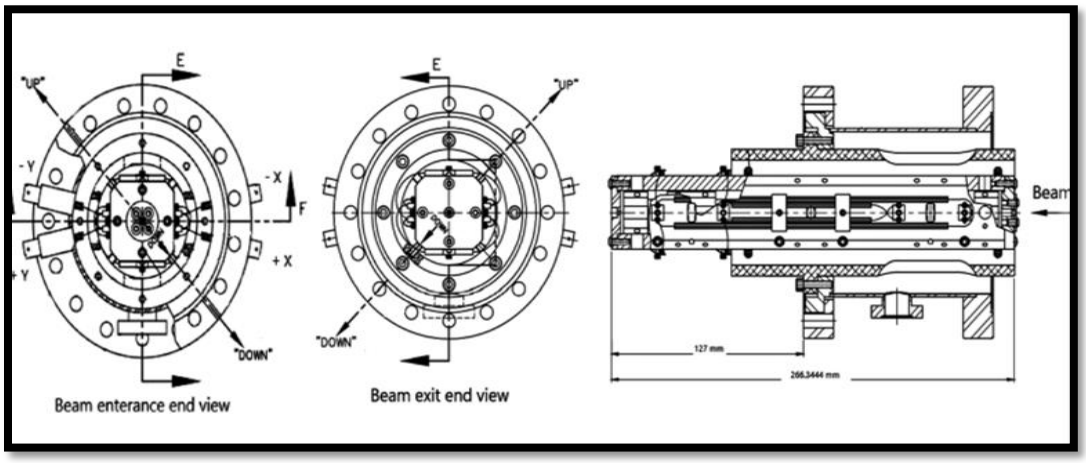

Figure 3.9: The schematic ECU's electrostatic quadrupole quadruplet from NEC.

3.3.5 Pressure sensor:

The sensor and control unit utilizes a fast trigger for emergency operation protection with the NEC Fast-acting valve. The NEC Coaxial Pressure Sensor (see figure 3.10) senses the pressure and increasing the pressure rate in the range of 10^{-4} to 10^{-3} torr. The control unit is also designed for fail-safe operation, which means that if power is lost, the circuit will trigger. The sensor comprises a cylinder with sealed ends. A turbomolecular pump in the L-15 beamline controls the necessary high-vacuum conditions. The turbomolecular pump is positioned on the downstream side of the Faraday cup position and serves to keep that section of the beamline pumped down to approximately 10^{-8} torr.

An anode wire of a small diameter (50 µm) is hung coaxially within the cylinder, come out from small holes in the end caps. A high D.C. voltage is foisted on the anode. At a threshold, the current pressure from the anode begins to pass to the cathode. The electrons orbiting the anode wire provide the current. The threshold effect of the accompanying recording is shown at approximately 0.4×10^{-4} torr. The current raised almost linearly with pressure till the trigger circuit fired at approximately 0.7×10^{-4} torr. That denoted as a completely clockwise sensitivity on the controller.[46]

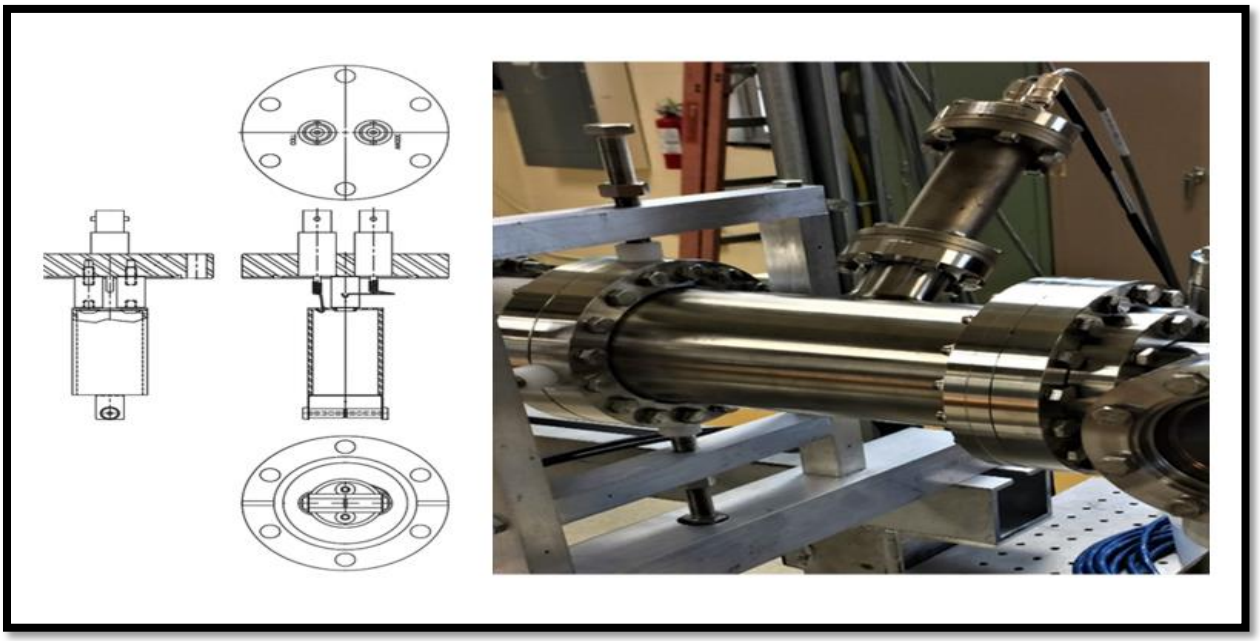

Figure 3.10: The ECU's Coaxial Pressure Sensor from NEC.[46]

3.3.6 Exit window:

The exit window aims to provide the proton beam to leave the L- 15 beamline to bomb the target. A particular exit window needs to allow the proton beam to pass by controlling the pressure variation and not allowing air to leak into the beamline. Certain species of windows are frequently composed of thin alloy foil. Silicon nitride (Si3N4) and Havar alloy foil (see figure 3.11) are the most widely used foils. Havar alloy foil comprises Be 400 ppm, Co 42.5%, Cr 20%, Mn 1.6%, Mo 2%, Ni 13%, W 2.8%, C 2000 ppm, Fe balance. It is classified as a non-magnetic high-strength alloy that preserves its strength even at relatively high temperatures. Havar foil thicknesses 10 µm and 10 mm diameter is used in the ECU L-15 beamline exit window.[47]

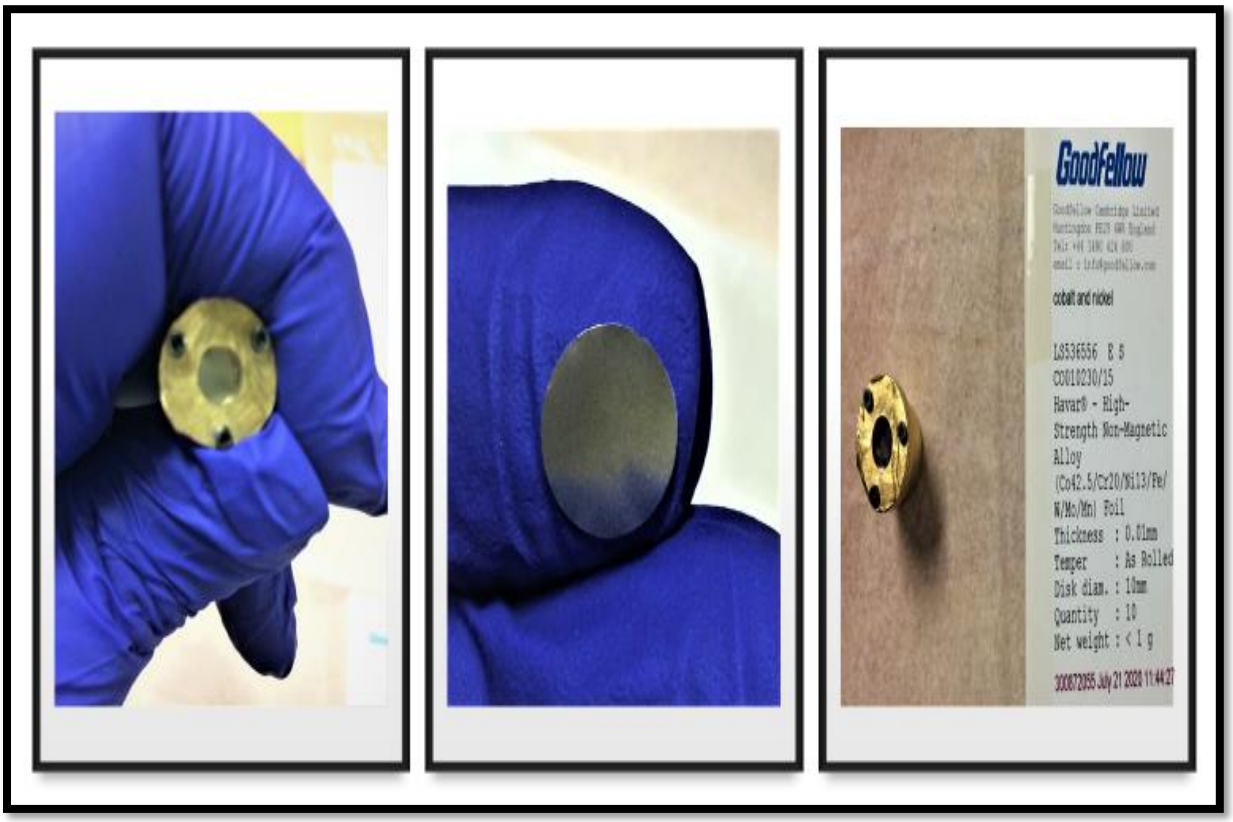

Figure 3.11: The Havar foil.

3.4 End station:

The end station (see figure 3.12) is the entire supporting segment for performing various experiments in the L-15 beamline, i.e., microbeam, micro PIXE, micro-neutron, micro-X-ray, and broad beam irradiation.

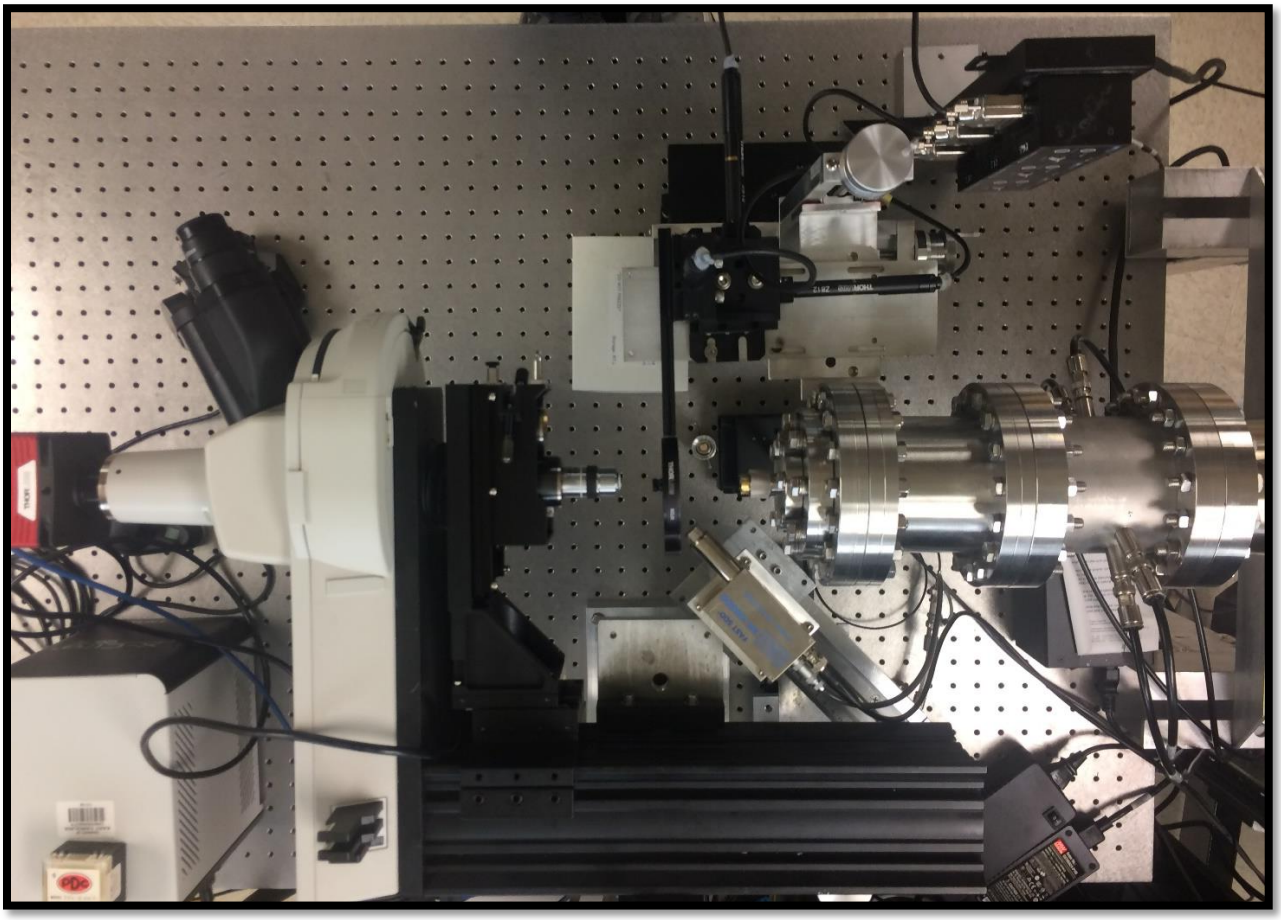

Figure 3.12: The L- 15 End station.

The passive isolator table from Thorlabs (see figure 3.13) is designed to eliminate floor vibrations in the critical frequency range of 10 Hz to 50 Hz. The passive air mount system provides Low-frequency isolation and excellent stability in both horizontal and vertical directions.

The thick wall construction provides complete safety and overload protection. The air mount continues to support and isolate even with no air pressure. Each isolator is composed of a cylinder-shaped rubber air mount mounted on top of a cylinder-shaped steel leg.

The top plate is bolted to the rubber mount, and the tabletop is held in place by an aluminum plate molded to the air mount. The tabletop's height can be adjusted using a standard Schraeder valve on each isolator's side to admit or release the air inside the mount.[48]

The passive isolator table in the L-15 beamline is necessary for stable the target on the table to perform single-cell irradiations.

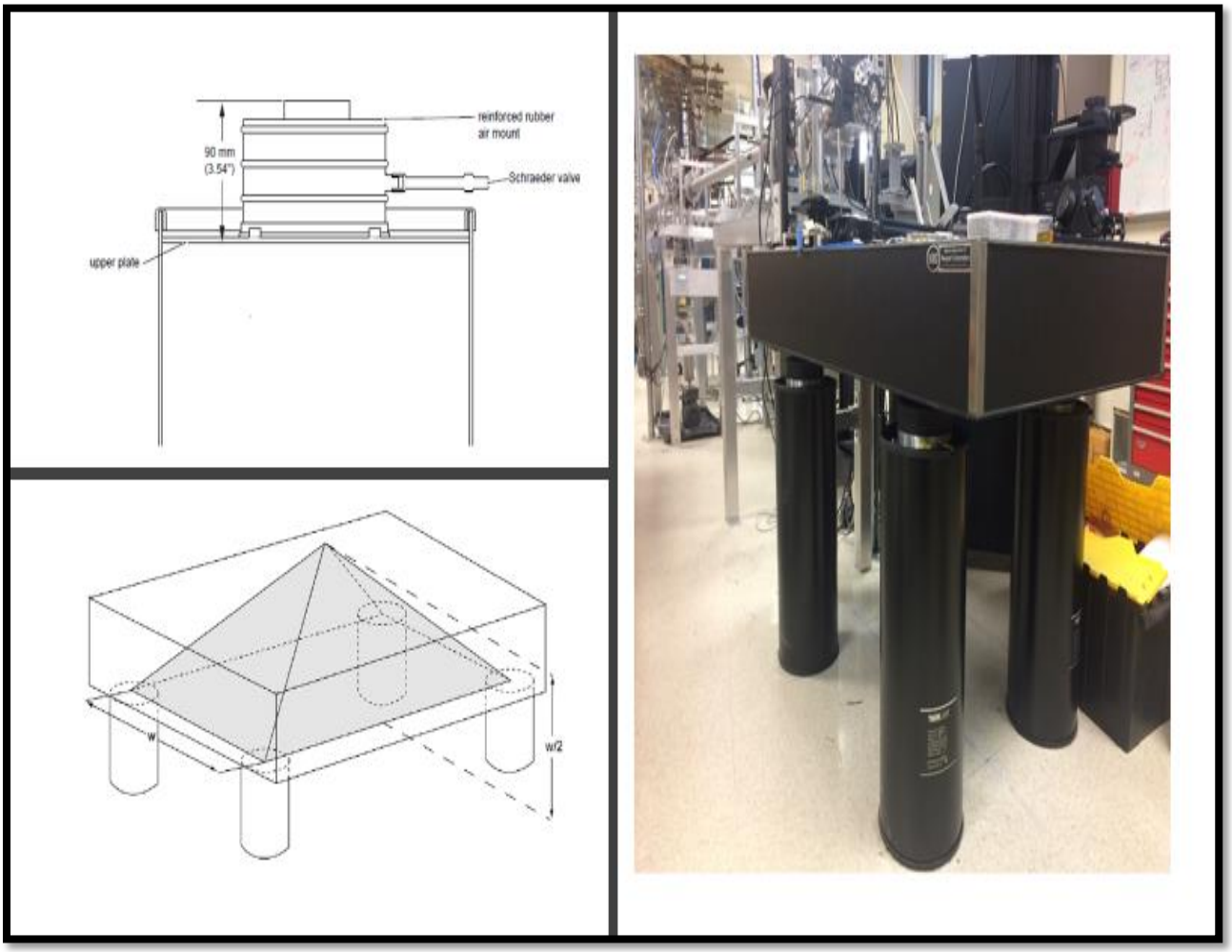

Figure 3.13: Passive isolation optical table.

Two radiation detectors have been constructed for variety utilizing from the beam. The first detector is a surface barrier detector used to record counts to measure the beam size. The second detector, the XR-100, is a fast silicon drift diode detector capable of better resolution, especially for low-energy x-ray spectra.

The imaging system consists of adjusted horizontal microscopy coupled with a fast camera. The USB manages the 3D motorized stage-controlled sample dishes.

3.5 Microprobe tuning equipment needed:

To tuning the microbeams focusing performance, a set of types of equipment have been used.

These equipment are:

3.5.1 Three-Axis precision movement Stage:

A series of high-resolution motorized actuators are used in high-precision applications. These motor drives meet even the most demanding specifications, ranging from drop-in replacements to custom mounts.

The travel length accessible is 12.0 mm and 0.05 µm minimum incremental movement, as shown in table 3.1. A 6V DC servo motor (see figure 3.14) is used in the Z800 series motorized actuators to provide enough torque for high load capabilities.

The actuators allow small steps through the entire range, providing greater versatility with negligible backlash and satisfactory resolution. The optical encoder allows for closed-loop operation, while the DC servo motor allows for continuously variable speeds. When the actuators exceed their mechanical limits, they have built-in hard stops that automatically cut the control. [49]

Specification	Z806	Z812/Z812B	Z825B
Travel Range	6 mm	12 mm	25 mm
Gear Reduction	67:1		
Lead Screw Pitch	1.0 mm		
Feedback	Motor-mounted rotary encoder 512 counts/rev of the motor 34,304 counts/rev of leadscrew		
Limit Switches	Electromechanical		
Motor Type†	6 V DC Servo		
Backlash	<8 µm		
Axial Load Capacity	9.0 kg		
Speed Range*	50 µm/sec to 2.6 mm/sec		
Calculated Resolution‡	29 nm		
Phase to Phase Resistance	33.0 Ω		
Phase to Phase Inductance	0.6 mH		
Operating Temperature	41° to 104° F (5° to 40° C)		
Cable Length	1.6 ft (0.5 m)		
Connector	HDDB15		
Compatible Controller	KDC101 K-Cube DC Servo Controller		

Table 1: showing the specification of the motorized actuators.[49]

The linear displacement of the motorized actuator per encoder count is calculated:

67 count encoder x 512 gear head = 34,304 encoder counts per revolution of the lead screw (high resolution optical encoder). The linear displacement of the lead screw is per encoder count:

1.0 mm / 34,304 counts =29 nm.[49]

Figure 3.14: Three MT1-Z8 single-axis stages mounted into an XYZ configuration via an MT402 right-angle bracket.[49]

3.5.2 Data acquisition:

A surface barrier detector, preamp (EG&G ORTEC 142), and MCA 527 L have been used to record the number of counts per second of the proton beam that passes through the Havar exit window.

The surface barrier detector is an ORTEC silicon-charged particle detector. It is a p-n type silicon diode wafer characterized by a relatively thin depletion layer. Surface barrier detectors are used essentially for α- and β-spectroscopy. The detector is biased with a +50 V floating power supply.

The MCA 527 L (see figure 3.15) is a battery-powered high-performance 16 K multi-channel analyzer / multi-channel scaler module. The integrated high voltage power supply for the detector and preamplifier, the internal coarse amplifier, an analog-digital converter, and digital signal processing are supplied. It forms a pocket-size gamma spectroscopy system and timer/counter when combined with a small detector.

It is well appropriate to the requirements of field measurements for international safeguards, radioactive transport control, nuclear waste treatment facilities, and environmental controlling. Moreover, the MCA 527 L is compatible with a wide range of detectors, and its 16-k resolution is adequate for high-resolution gamma spectrometry with HPGe detectors. The Mini MCA software provides the device to operate as a multi-channel general-purpose (WinSPEC) analyzer and multi-channel scaler analyzer (WinMCS).[50]

The MCA527L is a self-contained module. The MCA527L has its battery and provides power to radiation detectors; it also designs an alpha spectroscopy system with a detector and a computer. The spectra are stored in the MCA527L's memory and transferred to the computer regularly through a connection interface. The computer sets up the MCA527 L, presents the measured data, and saves the information. The MCA527L's design concept also includes a multi-channel scaler mode.[50] The MCA527L characterization is shown in figure 3.16.

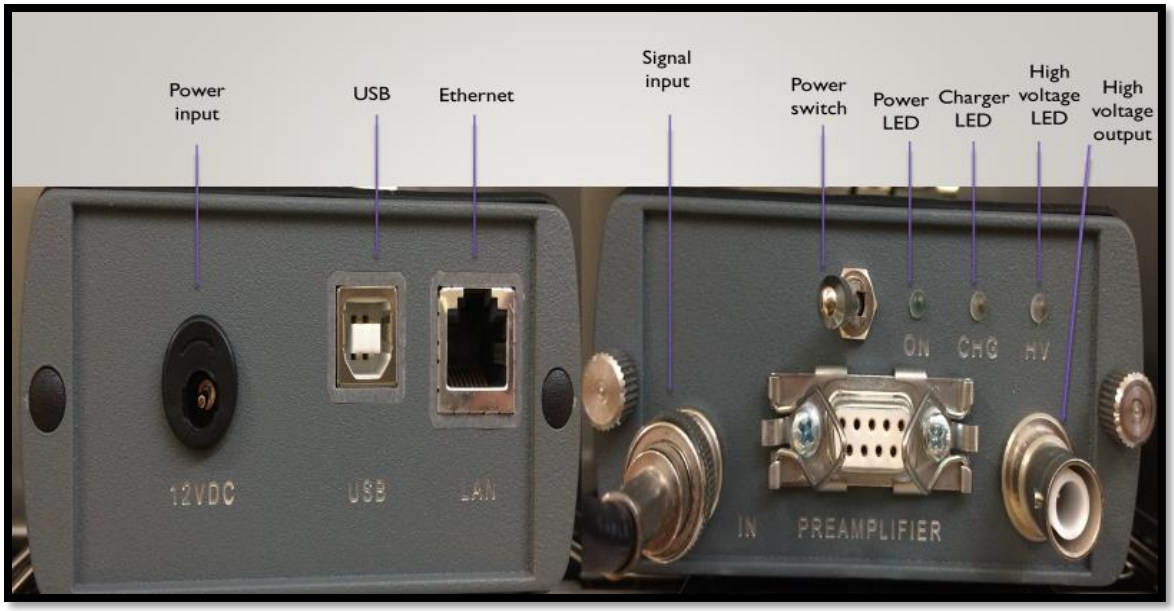

Figure 3.15: MCA527L connectors and control parts.

Trigger Filter	single and double differential trigger filters are selectable
Pile-Up Suppression	yes
Pulse Pair Resolution	~400ns, depending on trigger filter
Trigger Threshold Adjustment	automated (default) and manual
Shaping Time	0.1µs to 2µs 0.1µs steps
Flat Top Time	0µs to 5µs, changeable in steps of 0.1µs
Fine Gain Adjustment	0.5 to 6.5, changeable in steps of 0.01%
Channel Splitting	128, 256, 512, 1024, 2048

Environmental	
Operational Temperature Range	0°C to 50°C with batteries -20°C to 50°C with stationary power supply
Humidity	≤90%, non-condensing
Protection Class	IP42

Preamplifier Power Supply[1]	±12V, ±60mA
High Voltage Supply[2]	±1200V, 0.5W[4]

Input Voltage	9V to 14V DC	
Input Power	9W max. (charging empty battery)	
Power Consumption	1W typ. (no detector connected) 2W typ. (detector supplied by MCA)	
Battery capacity	31.2Wh	15.8Wh

Spectroscopic Performance	
Resolution (FWHM) for typical 500mm² planar HPGe detector (count rate ≤10.000cps)	≤510eV at 1µs shaping time (Am241 source at 59keV) ≤460eV at 2µs shaping time (Am241 source at 59keV)
Usable Spectral Range	0.13% to 100% (e. g. 3keV to 2300keV) with optimized system
Throughput in Memory	≥75kcps at 140kcps input rate and 0.5µs shaping time ≥35kcps at 50kcps input rate and 2µs shaping time

Figure 3.16: MCA 527L operational ratings.[50]

An Am-241 alpha source is used to generate control data for the initial energy calibration. As a result, the expected energy spectrum is shown in figure 3.17.

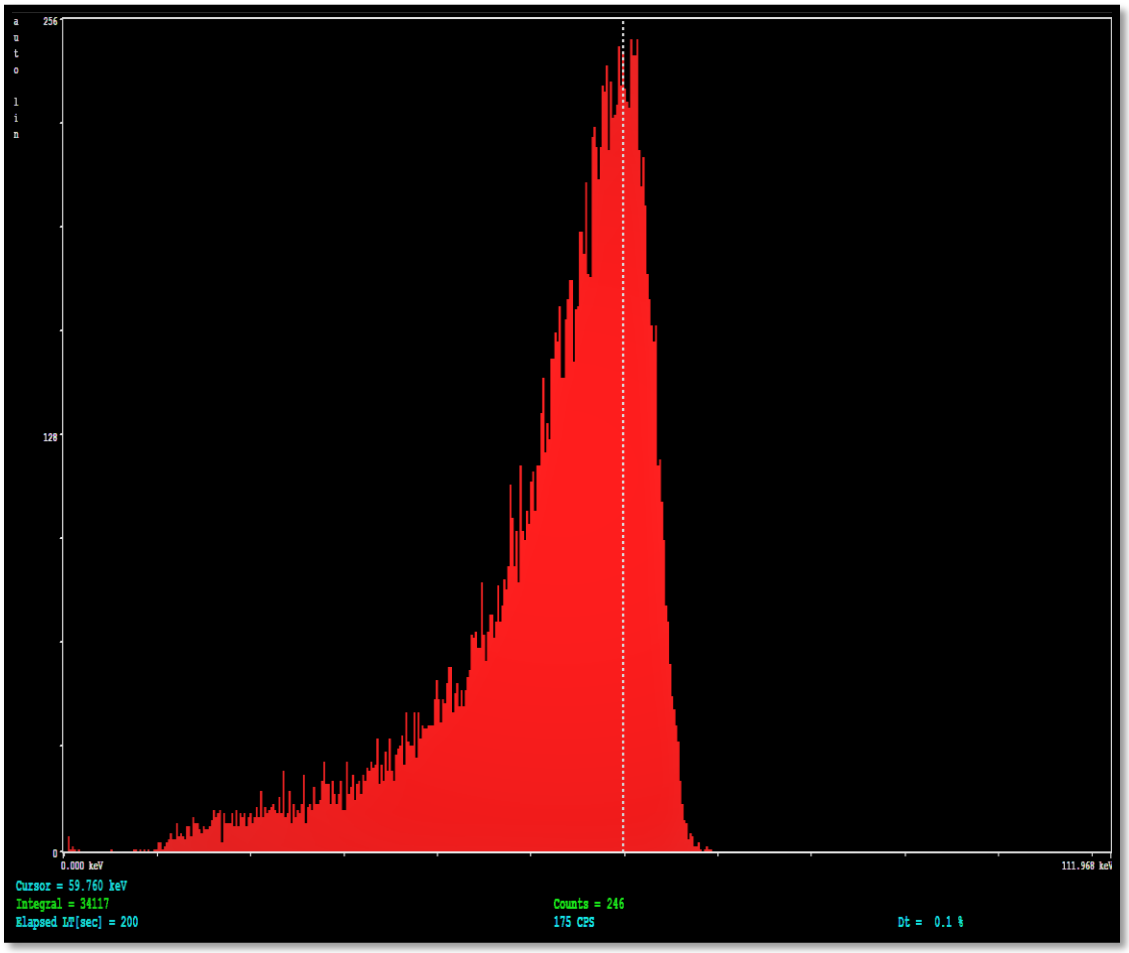

Figure 3.17: Energy spectra of the 241 Am alpha source obtained from MCA 527L.

3.5.3 Imaging system:

As shown in figure 3.18, a microbeam imaging system has been set up at the L-15 beamline end-station, approximately 5cm in front of the exit window. It consists of a microscope and a CCD Camera. The microscope was custom-built and conformed to the geometrical constraints of the irradiation end-station, which has a Nikon and Thorlabs microscope at the end of a horizontal ion beam. The microscopy on microbeam end-station has become a routine technique for visualizing specimens previously, though, and the following irradiation.

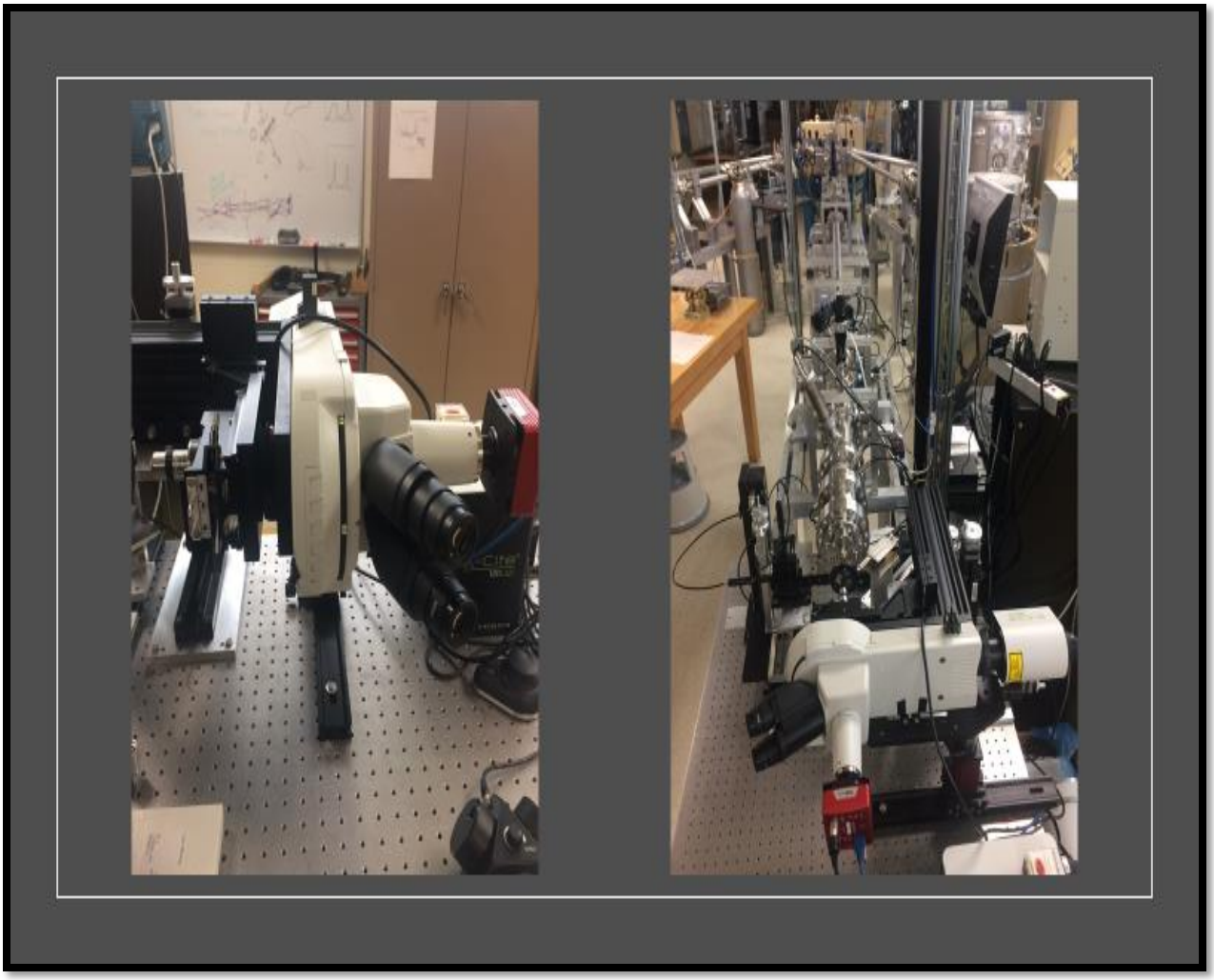

Figure 3.18: Imaging system on L-15 beamline.

The microscope will adapt a Nikon M Plan 40x ELWD objective with a 10.1 mm working distance or more.

The imaging system includes Thorlabs' fast frame rate scientific CCD camera, with 640 x 480-pixel (VGA) resolution and up to 200.7 frames per second at 40 MHz dual-tap readout designed explicitly for microscopy other demanding scientific applications. The monochrome camera is typical for the application of microscopy fluorescence and flow cytometry. The UV version of the camera has a sensor with a quartz faceplate to permit higher UV light transmission and applications at UV wavelengths, with a peak QE of 10% at 485 nm. The CCD specifications and the curve of the quantum efficiency of the camera sensor are shown in figure 3.19.[51]

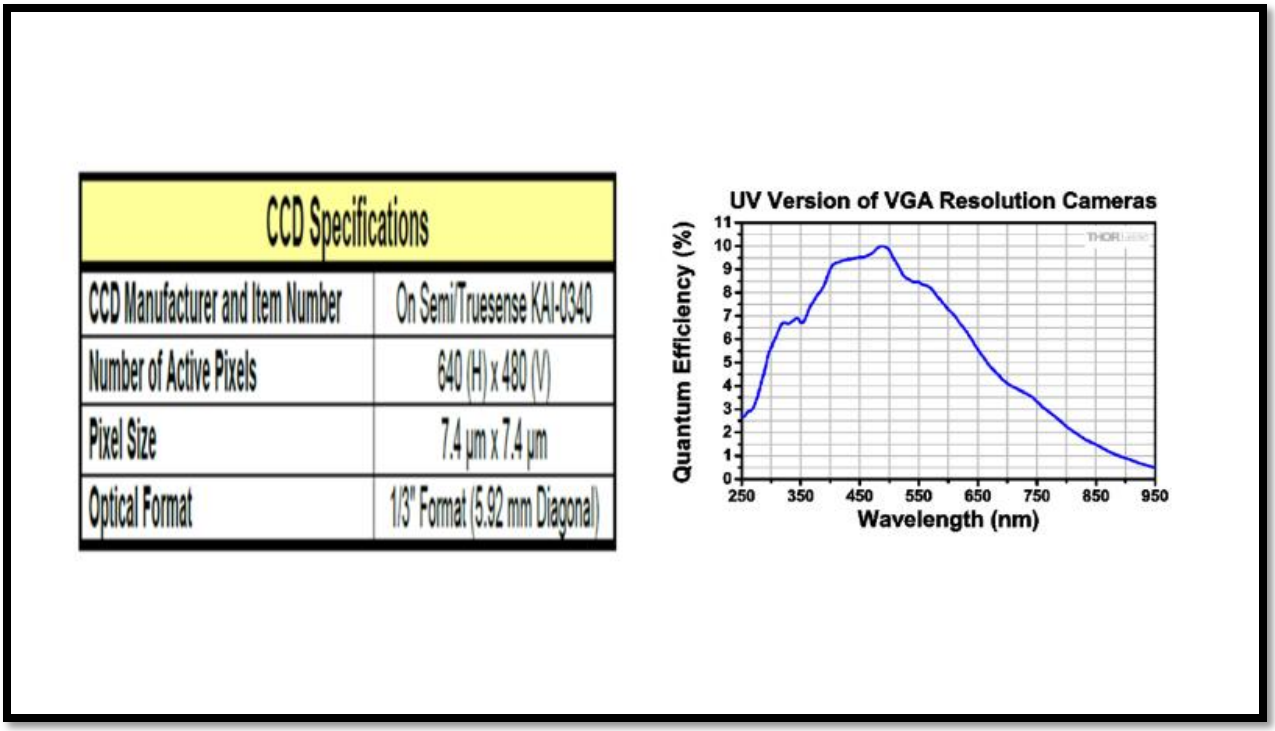

Figure 3.19: The CCD specifications and the curve of the quantum efficiency.[51]

3.5.4 MicroPIXE detector:

The resolution and efficiency of detectors are the most important factors to consider while comparing devices. The detector's performance is the count rate ratio to the rate at which photons impinge on the detector surface. The resolution of a detector refers to its ability to distinguish between spectral peaks. The detector must overcome these peaks for elements whose characteristic X-rays are close in energy to determine the presence and, more importantly, the concentration of the element. The detector will use the ECU's microPIXE (see figure 3.20), a silicon drift detector made by Amptek. The XR100 Fast SDD is located at an angle of 135° from the beam exit window. It comprises the detecting crystal and associated mounting hardware and wiring, digital pulse processor multi-channel analyzer (DPPMCA), Digital Acquisition software, and a thermoelectric cooler. [53,52,6]

Operation theory of the SDD detector:

In the direction of the detector, photons with energy E emitted by the irradiated sample will first confront a 12.5 µm thick beryllium window. Most photons with energies less than 1.3 keV are filtered out by attenuation within the window—the window filters out visible light. The SDD detector (see figure 3.21) has a front implanted P+ cathode with cognitive bias (-50 V), a region that intercepts incident x-rays, and an anode just a small plate with exceptional low capacitance. Pink noise is a common type of noise in silicon x-ray spectroscopy. [53,52,6]

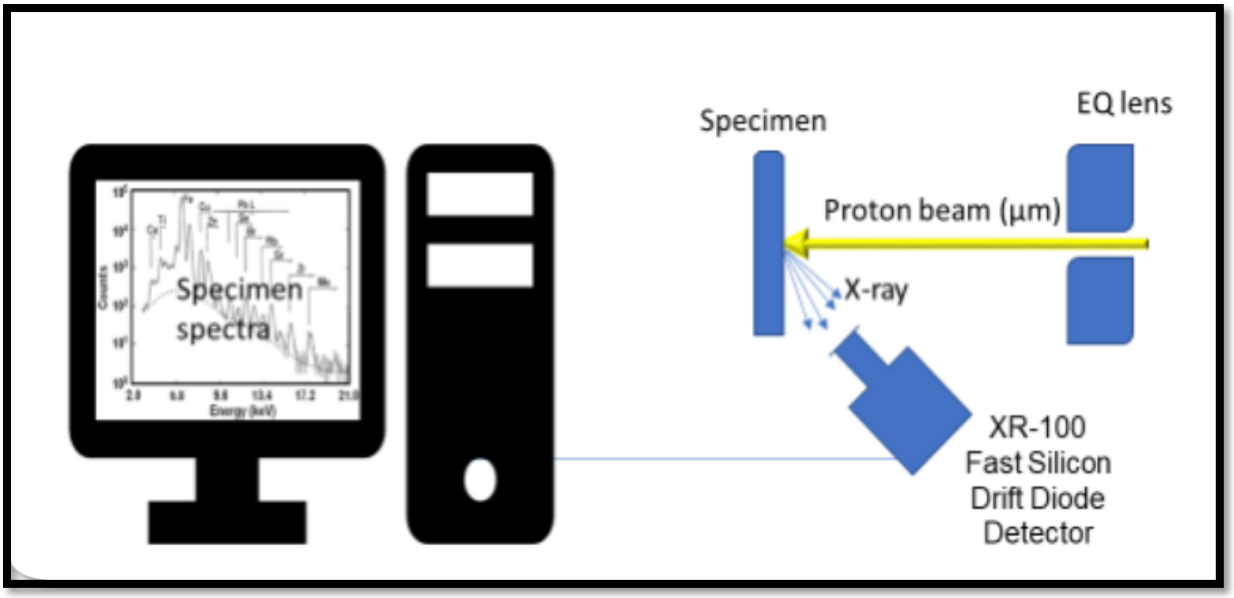

Figure 3.20: Schematic of X-ray detection.

High-frequency shaping times and input capacitance increase the noise; however, the low capacitance silicon drift detector provides lower noise at fast shaping times. The p+ implanted electrode rings are negatively biased; the outer ring is held at -100 V, with resistive dividers in between. The voltage gradually decreases by 10V increments until it reaches the inner ring held at virtual ground.

A diffusion current occurs as holes and electrons travel from higher to lower concentrations, generating the charge cloud to expand. An electric field will create and sweep the charge carriers radially to the anode. A current is induced within the diode as electrons drift for several

microseconds. That raises the collection time for interactions happening at the outer edge of the active volume of the drift diode, which leads to the rise time in the preamplifier fluctuating. Since the virtual ground electrode acts as a shield to the anode, the preamplifier rise time remains very fast; only drift movement happens after the final electrode can transmit the signal current to the anode.

Closed-loop temperature control regulates the temperature of the XR-100 FAST SDD. Lowering the detector temperature improves the energy resolution. As the detector operating temperature rises, so does the leakage current, resulting in a lack of energy resolution in the data. Maximum cooling can achieve temperatures ranging from 210 to 230 K. The SDD area does not significantly reduce resolution; the SDD has large surface areas with high resolution. For resolving peaks in the x-ray spectrum, a high-energy resolution is needed. The SDD is very low in electronic noise at short shaping times. At energies below five keV, lower noise at a high-count rate leads to improved resolution. [53,52,6] figure 3.22 shows the XR-100 fast silicon drift diode illustration of the operation and construction

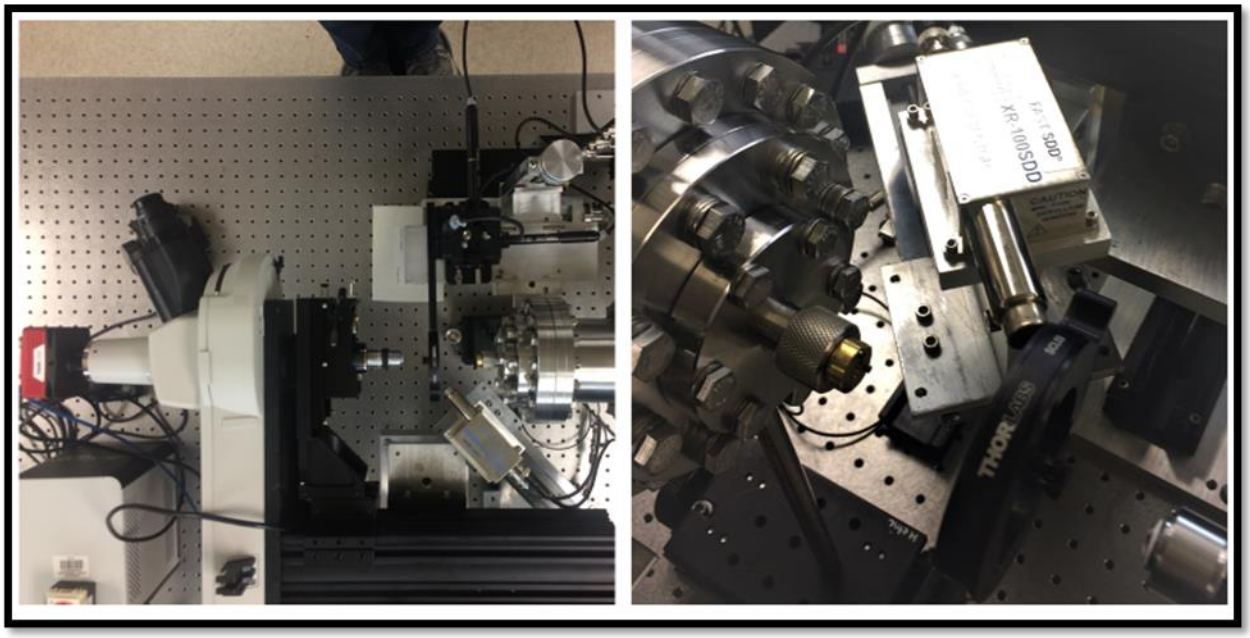

Figure 3.21: Fast SDD detector photograph XR-100.

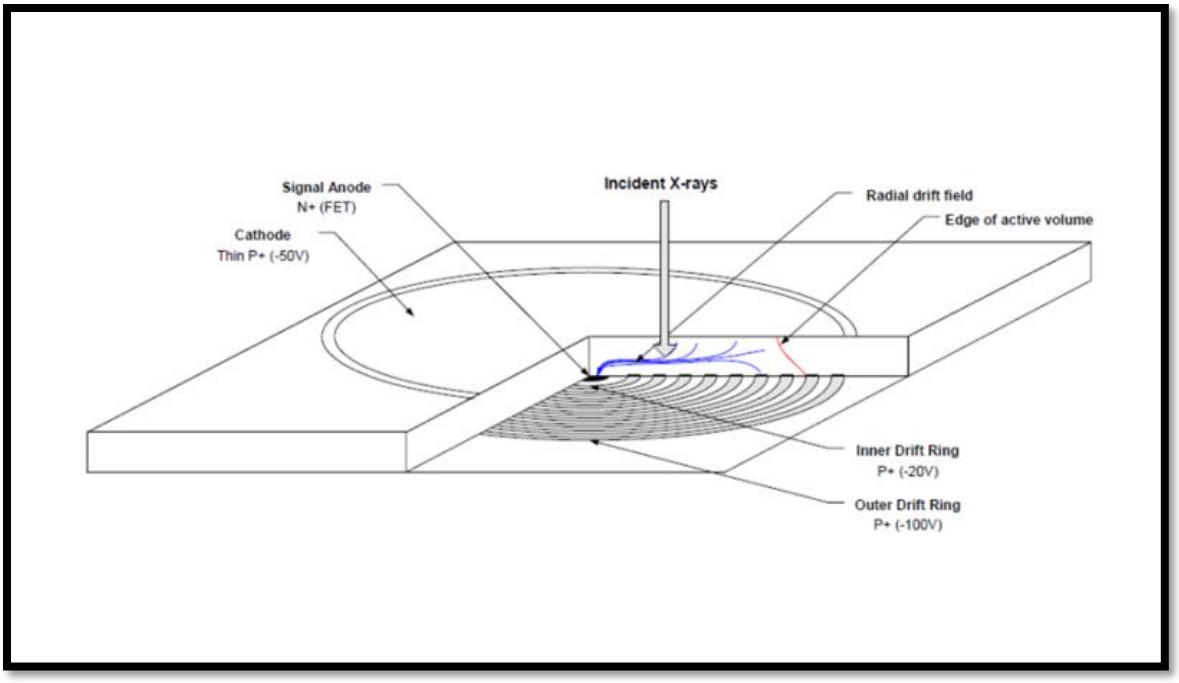

Figure 3.22: The XR-100 fast silicon drift diode illustration of the operation and construction [52].

The PX5 digital pulse processor provides superior resolution supporting higher count rates. It replaces the multi-channel analyzer and shaping amplifier located in analog detection electronics. Instead, the DPP digitizes preamplifier output, tracks peak amplitude, and bins data to send to the user interface. PX5 settings are all configured through the DPPMCA software.

A Fe-55 x-ray source is used to generate control data for the initial energy calibration. As a result, the x-ray energies emitted by Mn K_{α} (5.985 keV) and Mn K_{β} (6.49 keV) transitions were known, and the energy spectrum is calibrated with the expectation that the available manganese peaks will be visible in figure 3.23.

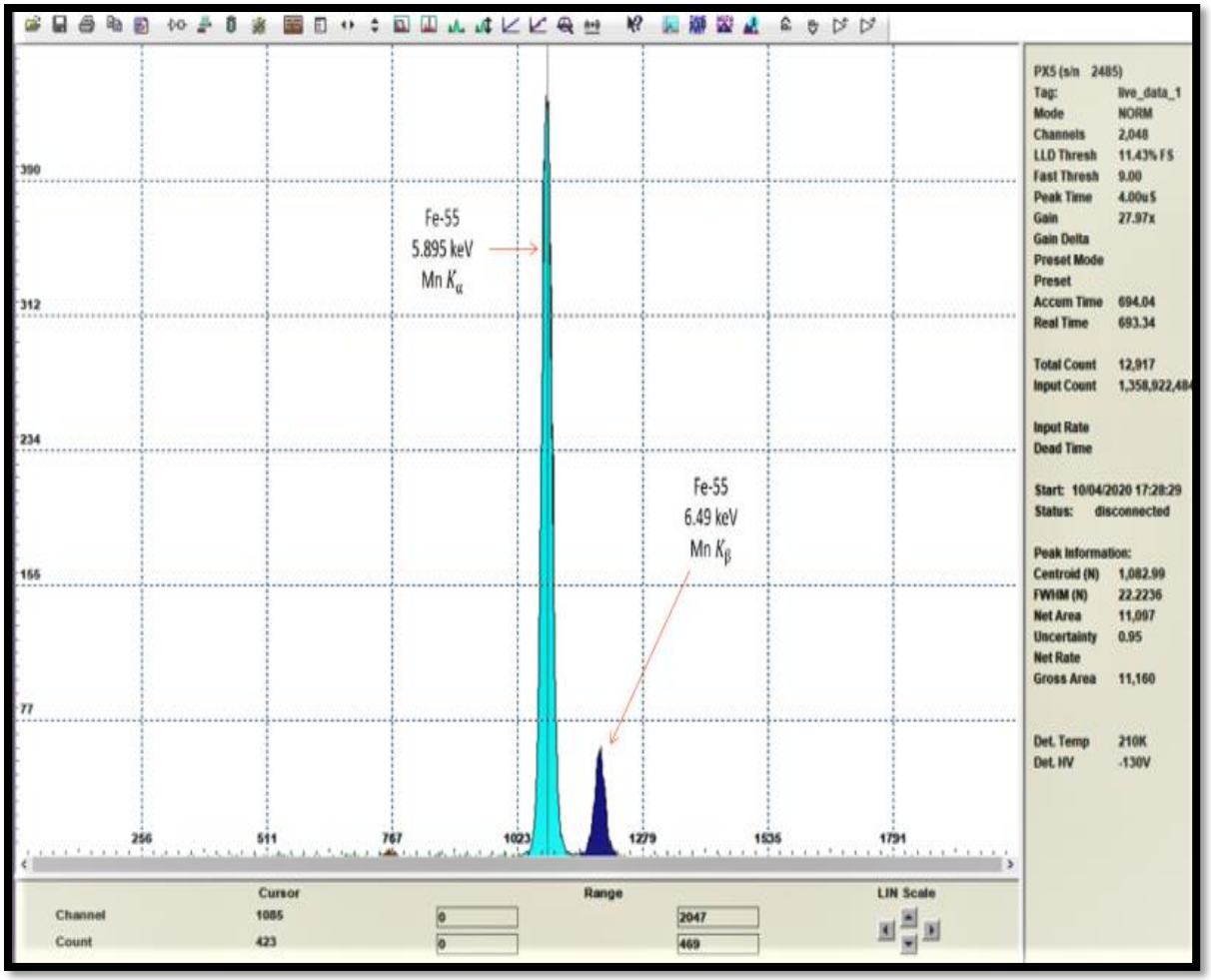

Figure 3.23: Fe-55 Energy Calibration Data.

Chapter Four
Microbeam Setup and Its Application

The L-15 beamline experiments start with the emission ions crossing the focusing and collimation systems. In this beamline, the experiments were performed using broad and microbeams.

4.1 Broad beam irradiation cells:

The beam must be profiled and characterized with information from the Faraday cup and the Scintillation Crystal (Yttrium aluminum garnet (YAG)) located directly in front of the Havar exit window in determining the correct cell dose. The dose rate is calculated with the stopping power predicted by the Stop-and-Ion Range (SRIM) code and the proton beam fluence measured with the F.C using equation (20). SRIM is a series of programs that use a quantum mechanical treatment of ion-atom collisions to measure the stopping and range of ions (up to 2 GeV/amu) in the material. Statistical algorithms allow the ion to make jumps between measured collisions and then average the collision results over the gap, making this calculation very efficient. [54]

The ion and atom have a Coulomb collision during collisions, including exchange and association interactions between the overlapping electron shells. Thus, various materials, including those used for Havar, air, and human cells, can be supported by the SRIM program when the beam left the 10 μm thick Havar window traveled into around 1.176 cm of air shown in figure 4.1.

Also, many simulations using the SRIM program were used for the fittest beam characterization that will cover the whole well in the plate, as shown in figures 4.2,4.3, and 4.4.

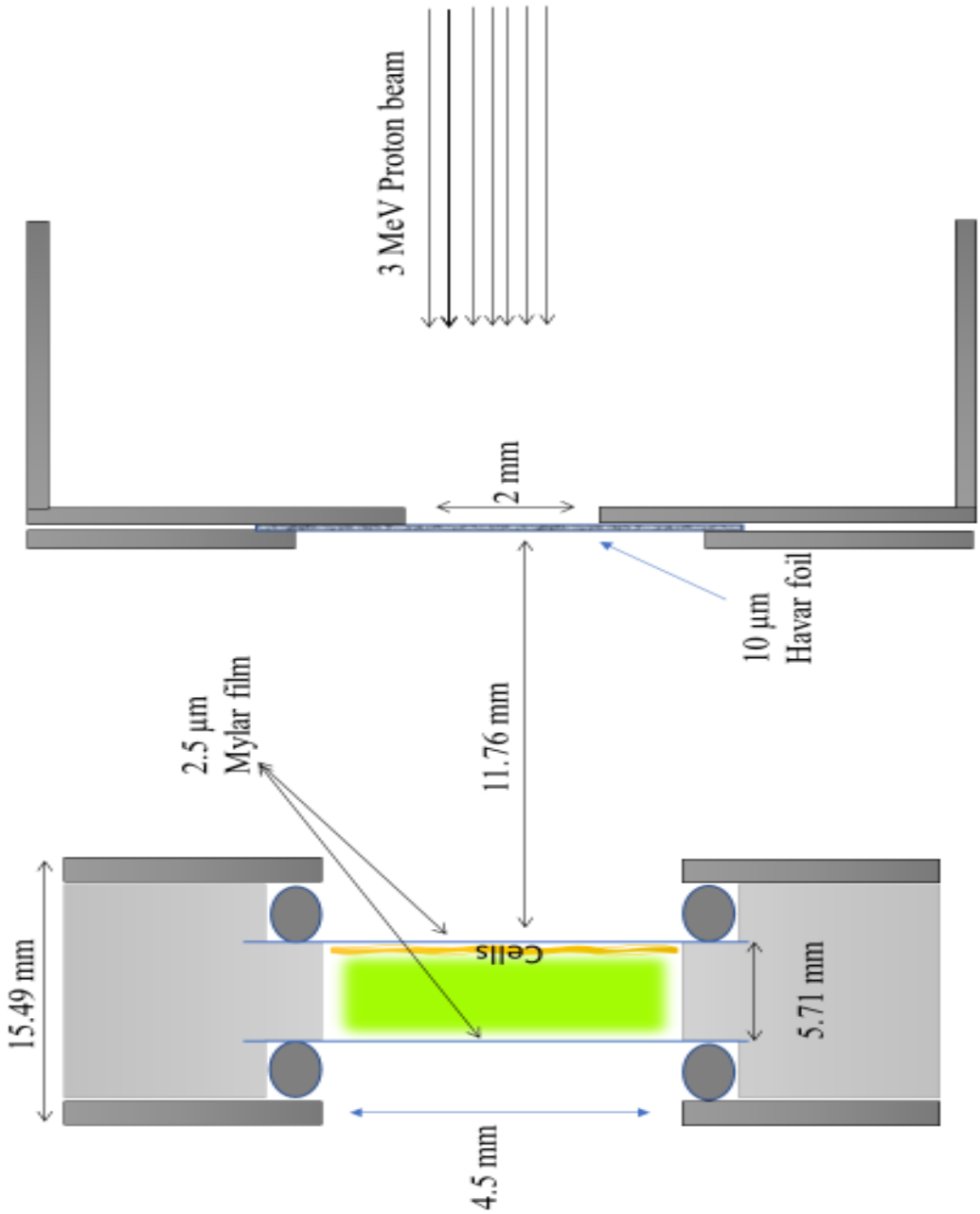

Figure 4.1: A representation of the design and precise measurements at the end of the L-15 broad beamline.

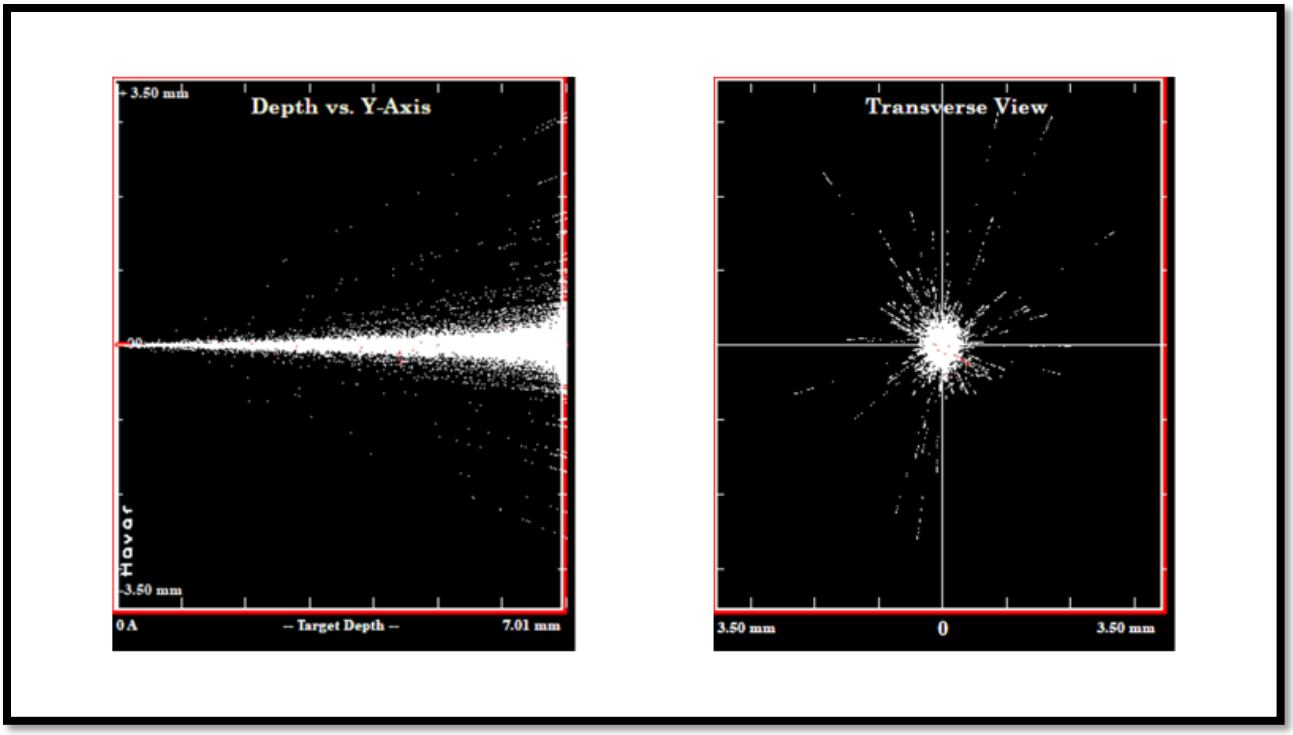

Figure 4.2: SRIM simulation for the 3 MeV proton beam 7 mm from the exit window.

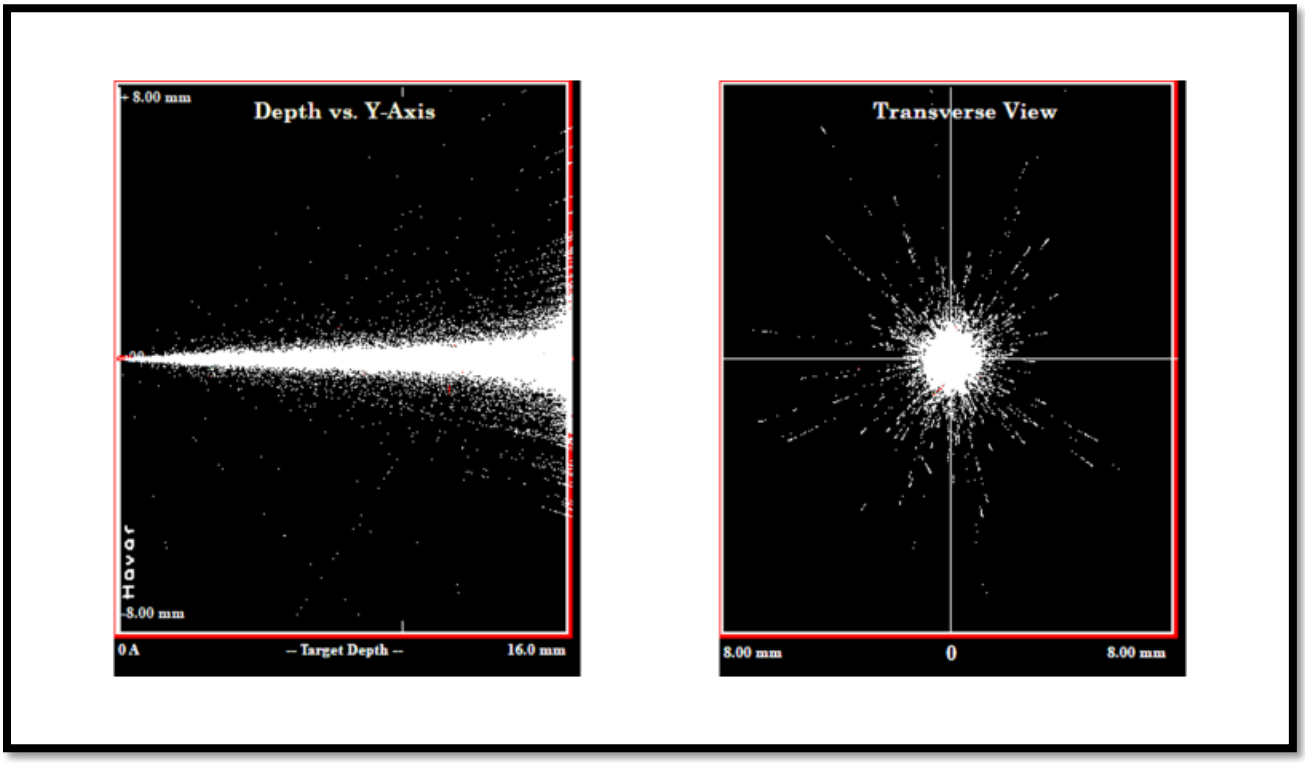

Figure 4.3: SRIM simulation for the 3 MeV proton beam 16 mm from the exit window.

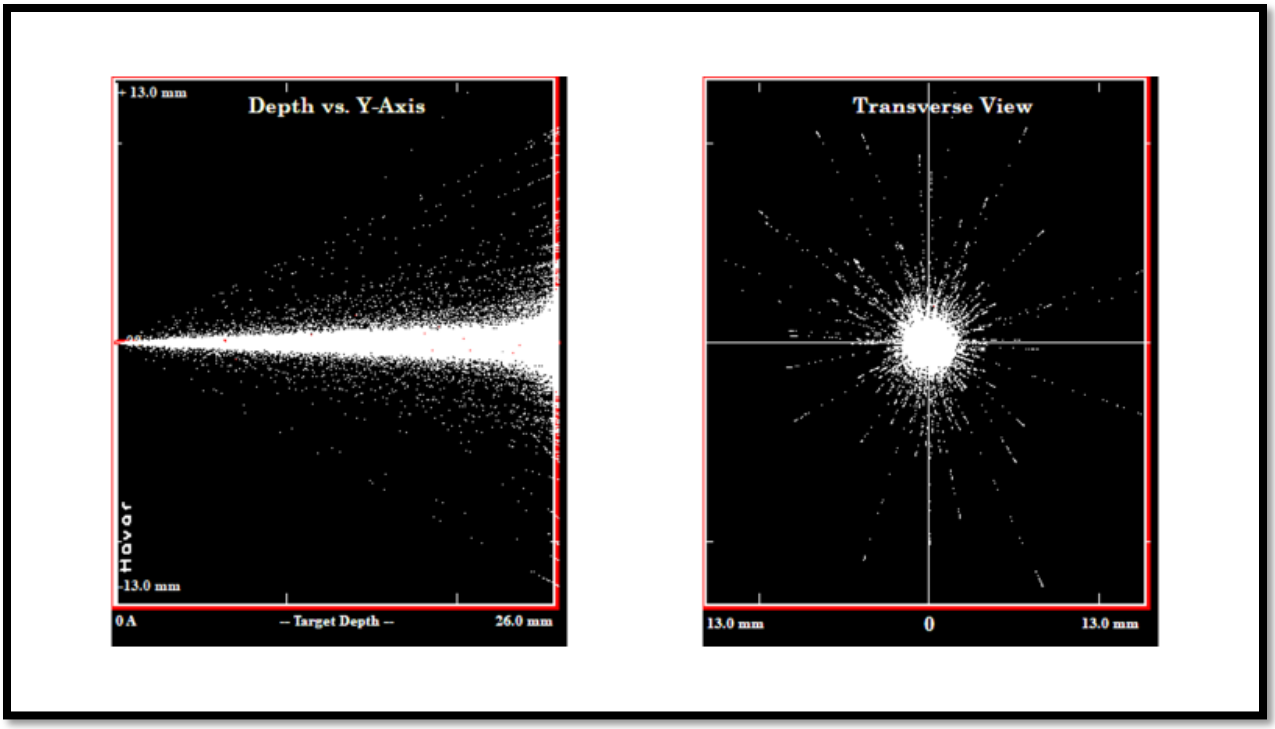

Figure 4.4: SRIM simulation for the 3 MeV proton beam 26 mm from the exit window.

The beam was characterized using an yttrium aluminum garnet (YAG) crystal to ensure our cell sample's accurate irradiation. The crystal gives the spot position concerning the cell sample when exposed to charged particles. The YAG crystal is held and moved in front of the exit window using the x and y movement stages. A fast frame rate scientific CCD camera was mounted directly behind the cell plate holder, focusing on the well-containing YAG crystal, which recorded an image using windows, characterized by ImageJ. The image has been processed and reproduced in a 3D image showing the YAG crystal beam flux variability. The beam is modified with quadrupole magnets and remotely slits till the beam adjustments consistently across the YAG crystal. Several beam size measurements with different distances from the exit window aimed to determine beam uniformity and allow the beam's convenient adjustment. The beam current has also been measured for these distances. Figures (4.5, 4.6, 4.7) represent the intensity profile of the cerium-doped crystal YAG, which has been bombarded with uniformity-adjusted protons for different distances from the exit window. These images were taken using a camera at the end-station of the beamline and processed with ImageJ software.

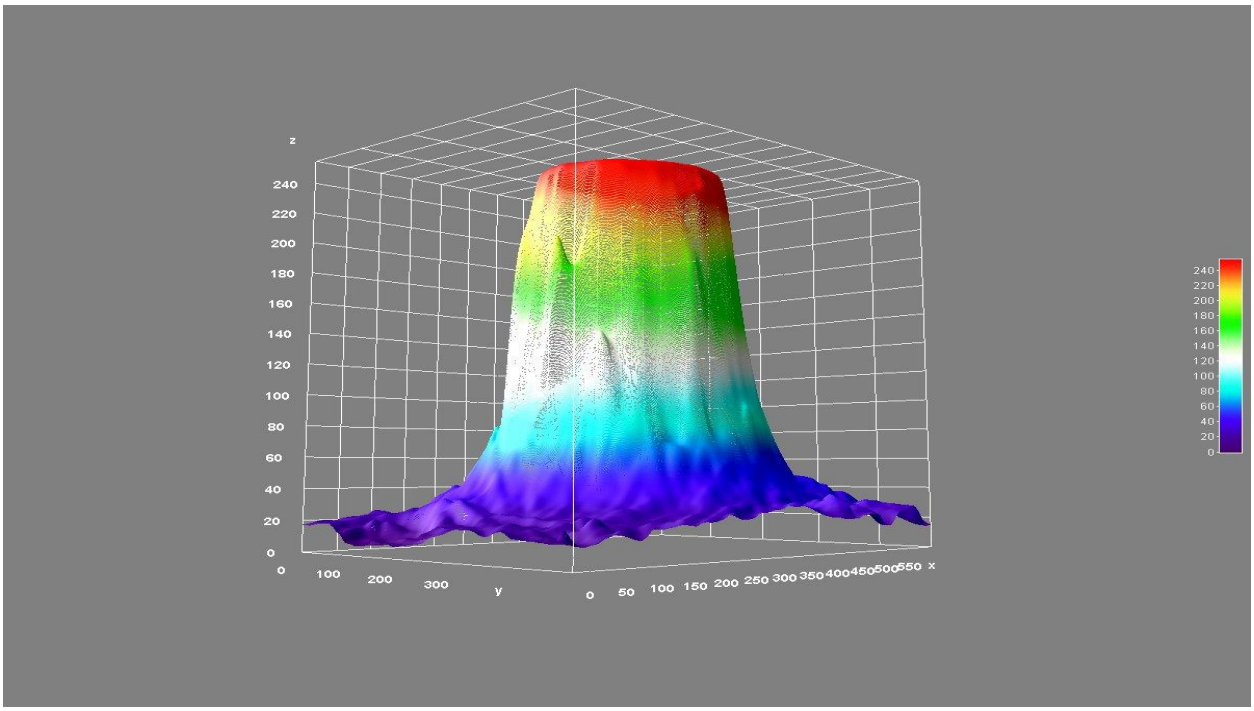

Figures 4.5: A beam profile analysis image was created by ImageJ.

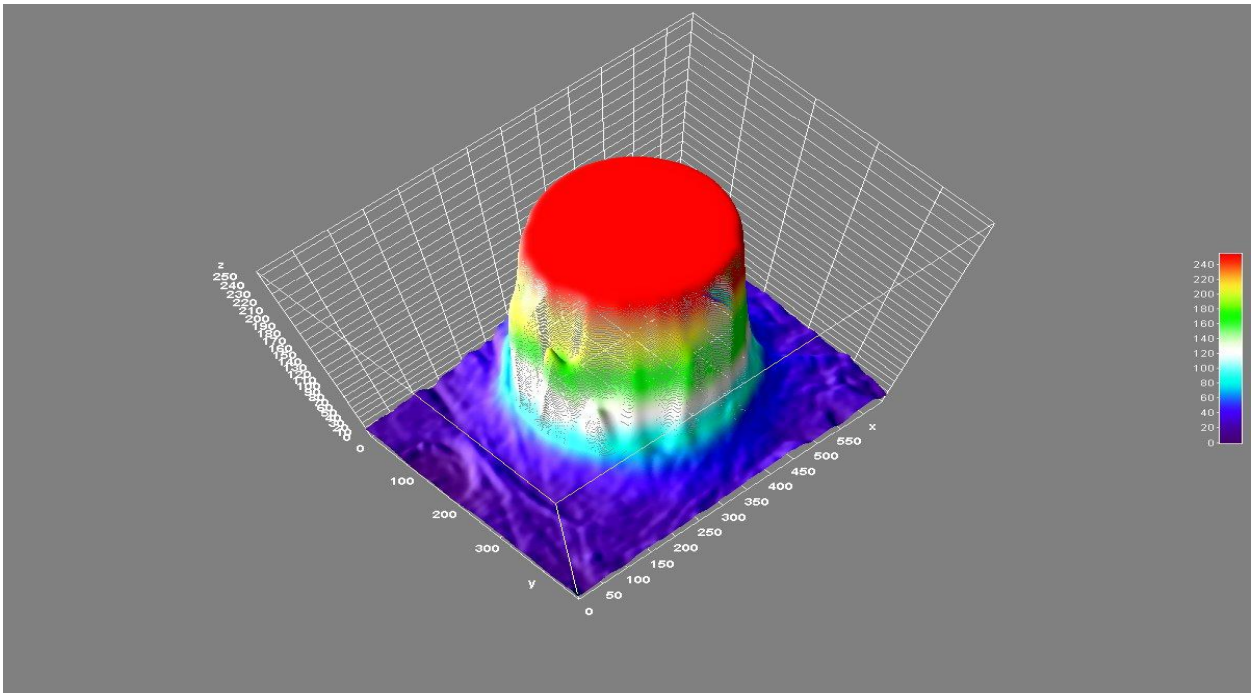

Figures 4.6: A beam profile analysis image was created by ImageJ.

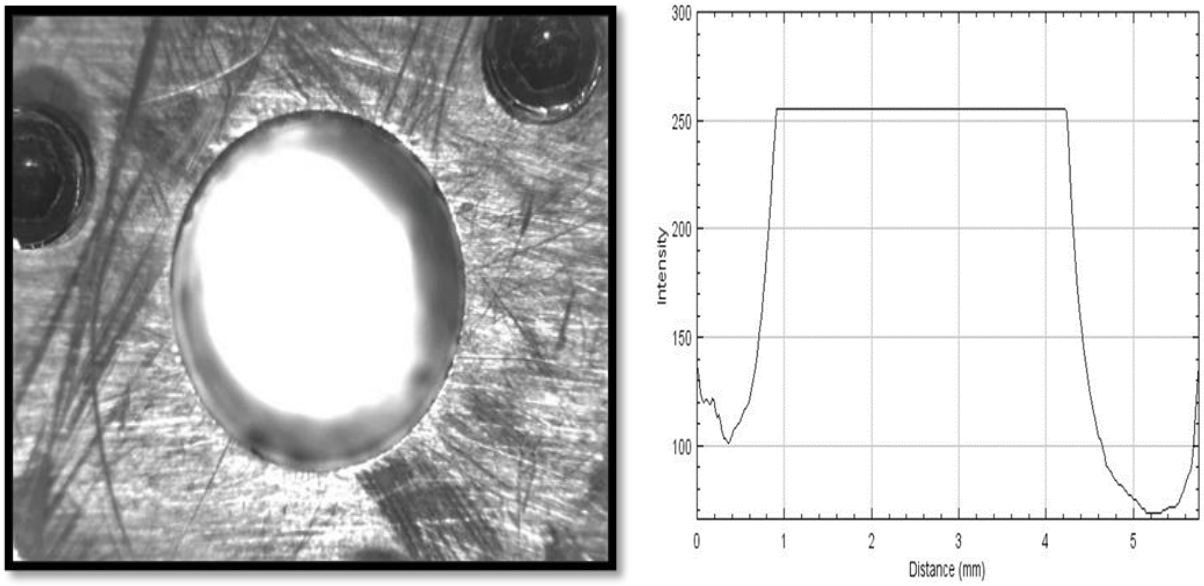

Figures 4.7: A visual of the scintillation process and capture of an image to characterize the beam intensity profile and schematic plot of the beam size.

Depending on the ImageJ processing analysis, the best determining beam uniformity beamline distance chosen for the cell sample's accurate irradiation is 1.176 cm from the exit window. To obtain a small penumbra:

1- Source diameter has a small diameter of 2-3 mm. For the L-15 beam line, the exit aperture diameter is 2 mm.

2- Distance between the source and the collimator as large as possible for L-15 beamline distance from source to the target is 11.76 mm, which is the best that we got depending on the beam energy measured depending on the stopping power LET in the air and Mylar film.

A special cell culture plate has been developed to keep the cells in their nutrient medium during irradiation. The main aim of the design is to create a cell culture plate that is as like traditional cell culture conditions as possible while still satisfying the requirements of beam irradiation. The cell culture plate for beam irradiation must consider many factors:[62]

First- mammalian cells must be able to be cultured in the dish.

Second- to minimize the beam's divergence, the front film must be thinner as possible.

Third- to reduce the loss of the dose pass through the long-distance of media or air (approximately 1.5 cm), the well must have reasonably well depth.

The new cell culture plate was manufactured in the ECU physics department, dependent on keeping the cells in their growth media, increasing the number of cell wells irradiated, and ensuring the wells' safety distance from twice irradiation.

The plate has 15 wells with a well inter diameter of 4.5 mm. The front and back of the cell wells are sealed by a Mylar film (Chemplex Industries Inc. - FL-USA) with a thickness of 2.5 μm, the thinnest commercially available and stretched tighten and smooth, which compression by black O-rings (inner diameter 5.5 mm, outer diameter 9.5 mm, and ring diameter 2 mm), as shown in figure 4.11.

The plate dimensions are long 114.8 mm, width 15.5 mm, and high 76.25 mm, as shown in figures 4.8, 4.9. The cell plate is handled using the X and Y movement stage to move the required well (up, down) or (left, right) precisely to the exit window to irradiate, as shown in figure 4.10. The movement stage was programmed to control accurate moving distance.

Figure 4.8: The custom cell culture plate with the 2.5 μm Mylar film covers the wells.

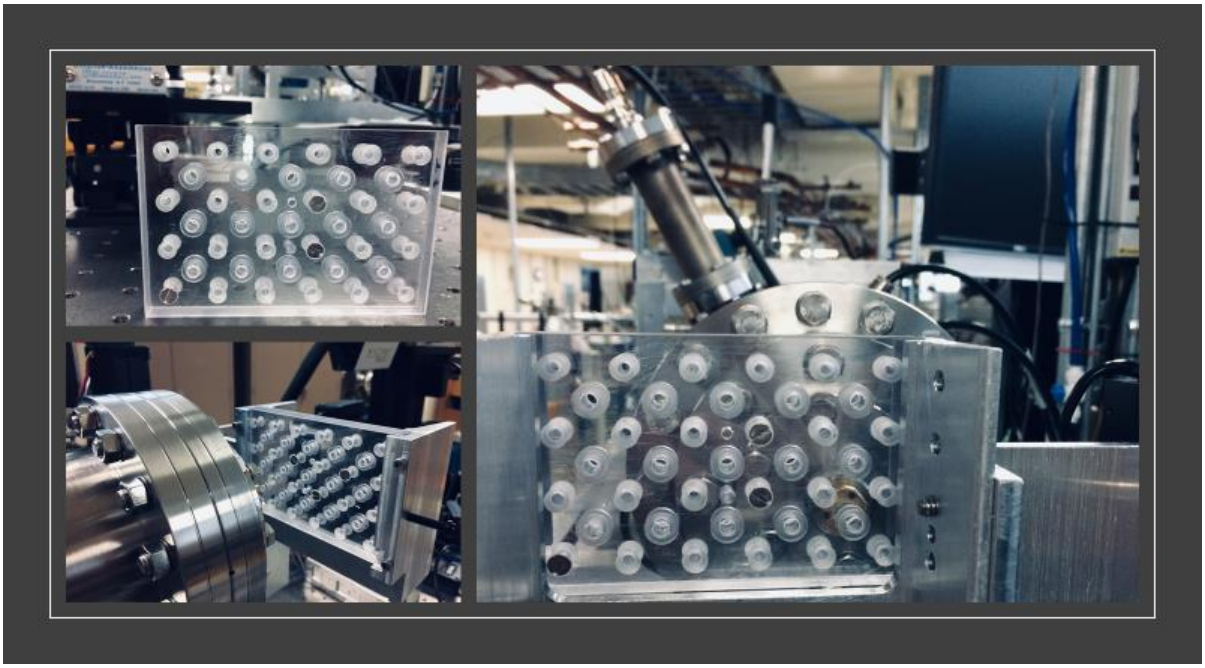

Figure 4.9: The custom cell culture plate.

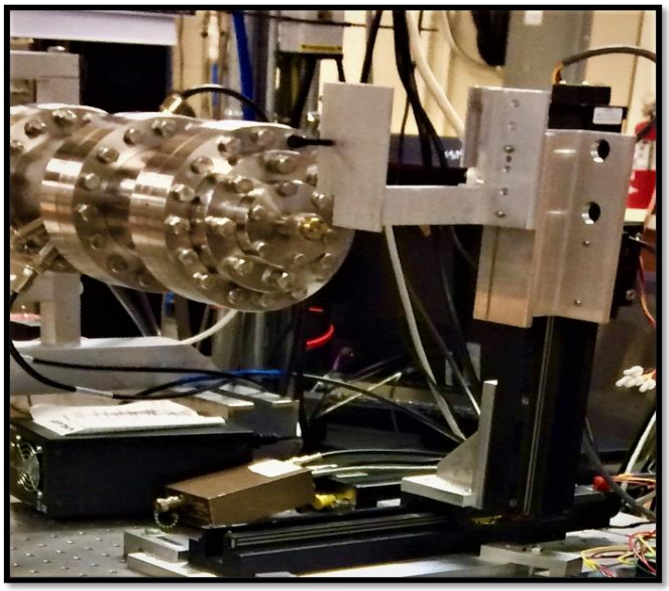

Figure 4.10: The X and Y precision movement stage.

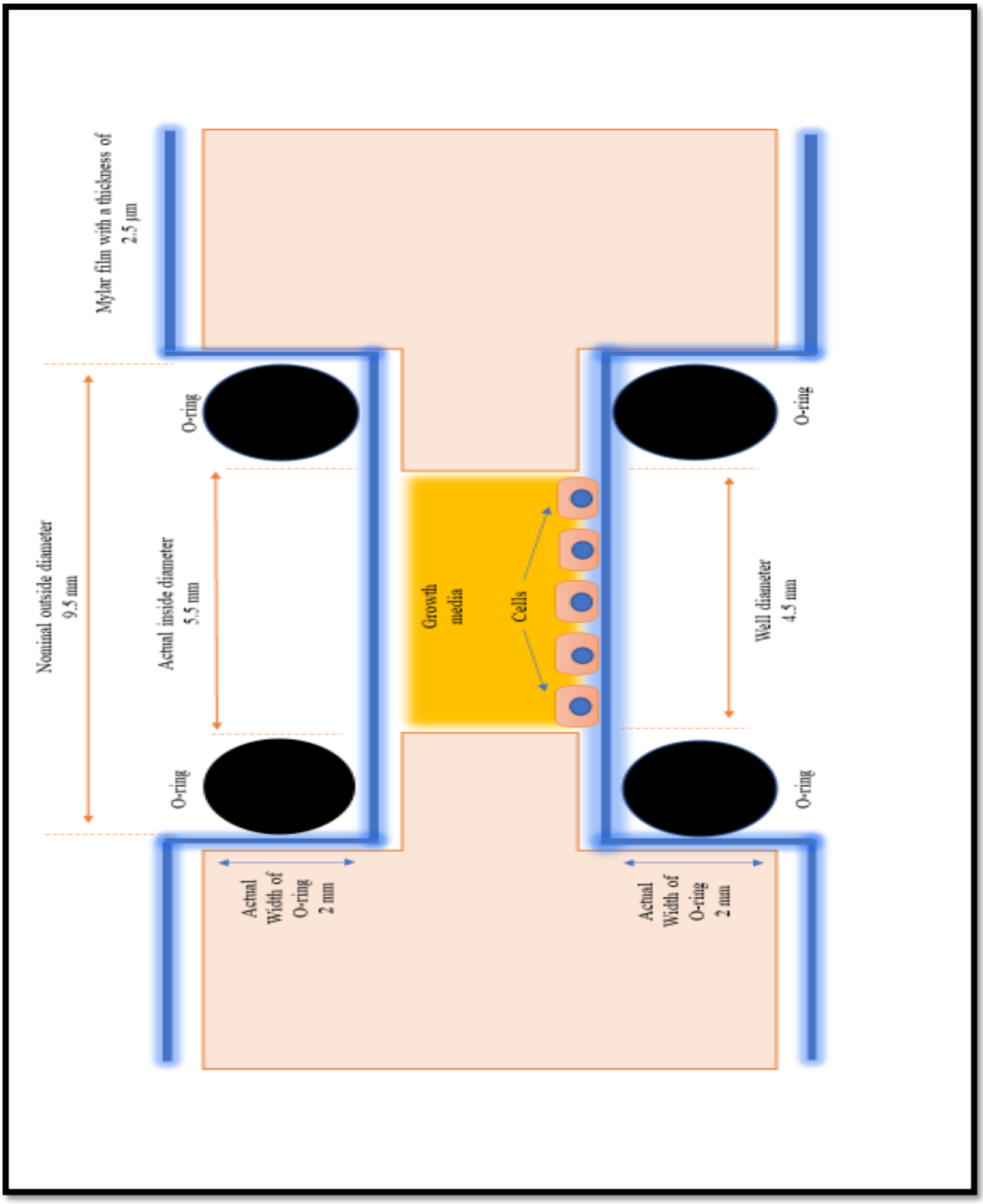

Figure 4.11: A schematic diagram of the cell well.

4.2 Cell culture and irradiation procedure:

The start of each experiment with cells were seeded using typical plating protocols to ensure the cells' survival and well-being throughout the experimental run and to ensure that planned sections of cells from the initial sample are viable for later studies, phenomenal attention must be used in the initial thawing, subculturing, and seeding of cells.

The Cell culture procedure started with the plates sanitized using alcohol and UV light and used the mylar and O-rings to seed and seal the cell in the plates, as shown in figure 4.12. The MCF7 cell lines were used in this experiment. MCF7 is an epithelial breast adenocarcinoma cell line derived from a metastatic pleural effusion (ATCC® Cat. No. HTB-22™).

The day before irradiation, count and measure cells for density and viability and plate 20000 cells / well in one ml of complete growth medium ATCC® Eagle's Minimum Essential Medium (EMEM) complete media supplemented with 0.01 mg/ml human recombinant insulin and 10 % FBS. A 69-year-old woman's breast tissue was used to establish the MCF7 malignant cell line.[63] The cells are incubated overnight at 37°C with 5% CO_2.[59]

The carbon dioxide CO_2 is a substrate in the bicarbonate buffering system present in the media, which controls the pH. Generally, the cells are susceptible to pH fluctuations and should be regulated at about 7.4 pH, the average pH of the human body's blood. [57,60,61] Once the proton beam has been stabilized on target, every setting has been optimized to create uniformity, and the dose is calculated, then the cells are ready to be irradiated.

The cells are then carried to the accelerator laboratory in these well plates. The beam current is checked to ensure stability during this procedure. When a slight variation occurs, the dose time is re-calculated to ensure that the relative doses of all specimens are the same. The cells are promptly returned to the cell culture laboratory after the irradiation is complete. After that, the plates are returned to the incubator, where the cells can recuperate for 24 hours at 37°C (5 percent CO2).

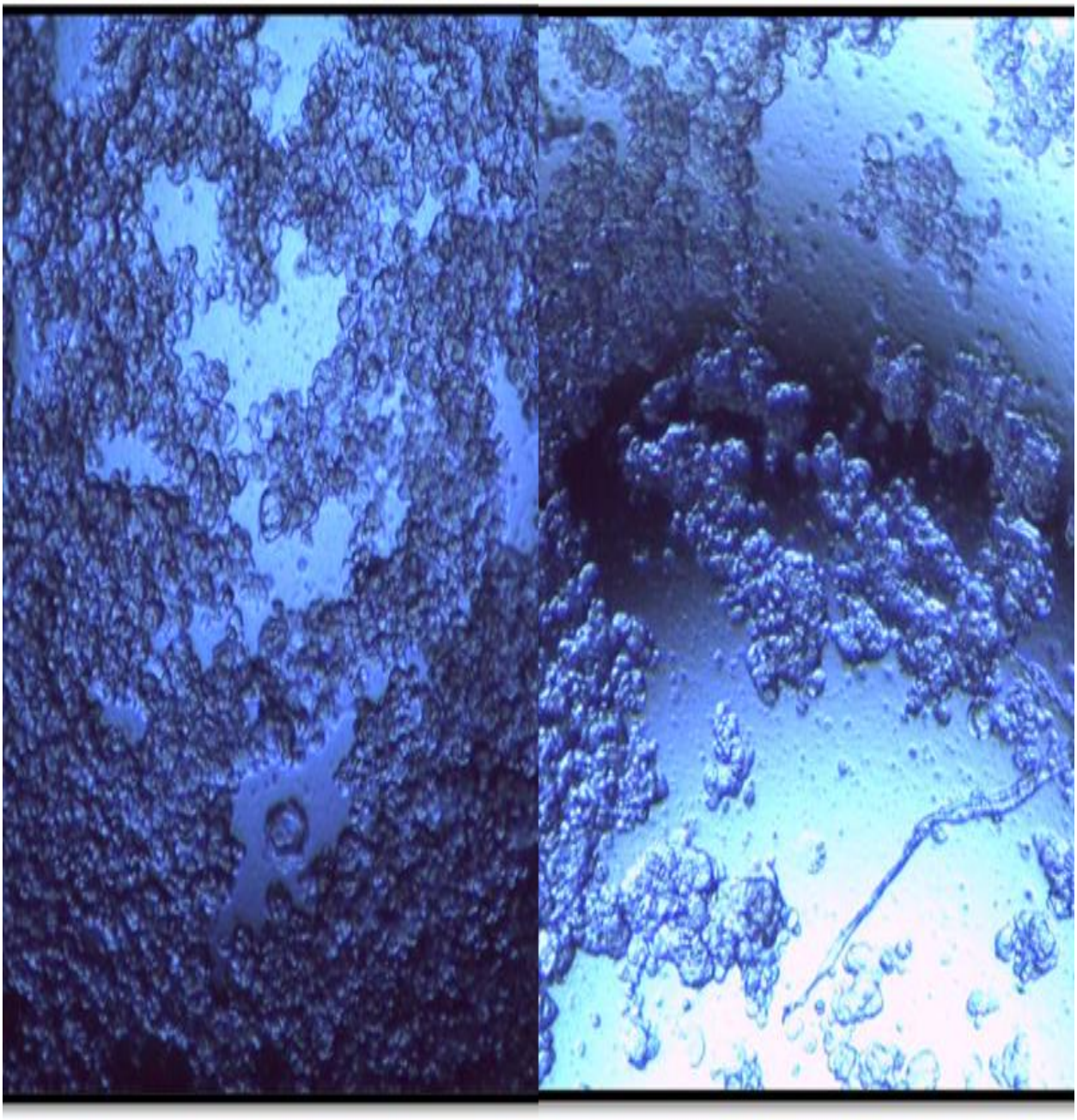

Figures 4.12: A photo of the cells after they have been seeded in a new plate.

4.3 PrestoBlue Assay (PB):

PrestoBlue is a resazurin-based compound that converts to a reduced form in the tested systems by mitochondrial enzymes. It is a cell-mediated cytotoxicity detection assay that was designed in vitro. The reagent undergoes a color change and a shift in fluorescence resulting from the reduction, which may be evaluated using either a fluorometric or spectrophotometric technique. With a 10-minute incubation step, PB is the fastest live assay for measuring cell viability. It is also a highly sensitive assay, capable of detecting as low as 12 cells per well.

PrestoBlue was used to determine cell viability following irradiation. The presto blue (10%) and base growth media (90%) mixture is prepared 24 hours before the assay (with no additions like FBS or insulin), which is mixed in a 50mL conical and stored in the refrigerator once combined. Because this mixture is light sensitive, it is recommended to wrap the conical in foil before storing it. Next, the customized plates must be seeded. The aim is to seed the plate with approximately 20,000 cells and see roughly 70% confluency.

The existing media was washed from the cell well on the assay day and washed with warm presto blue solution PBS. Allow the presto blue solution to steady on the cells for a few minutes before removing them. The PBS with the presto blue and base media solution was replaced after removing the presto blue from the warm bath.

Next, replace the cell plate lid and let it incubate for 2 hours. During these 2 hours, the presto blue solution on the cells was changed color from dark purple to fuchsia. The color will depend on whereby confluent the cell wells are to start. After the two-hour incubation, the presto blue solution was replaced in a sterile 96 well plate placed in the plate reader to assess the color. The absorbance should be measured at 535 nm or 615 nm while setting up the plate reader. The presto blue assay should be performed on the cell before irradiation, 24 hours afterward, and 48 hours later. The cells will still be alive, allowing the assay to be performed on them at each interval.

The Multiskan FC is a high-quality filter-based microplate photometer. It measures absorbance in 340 to 850 nm wavelength using a 96 or 384-well plate format. The source of the light is a tungsten halogen lamp, and the optical system is based on one-channel optics, as shown in figure 4.13. Interference filters are used to select the wavelength. [65]

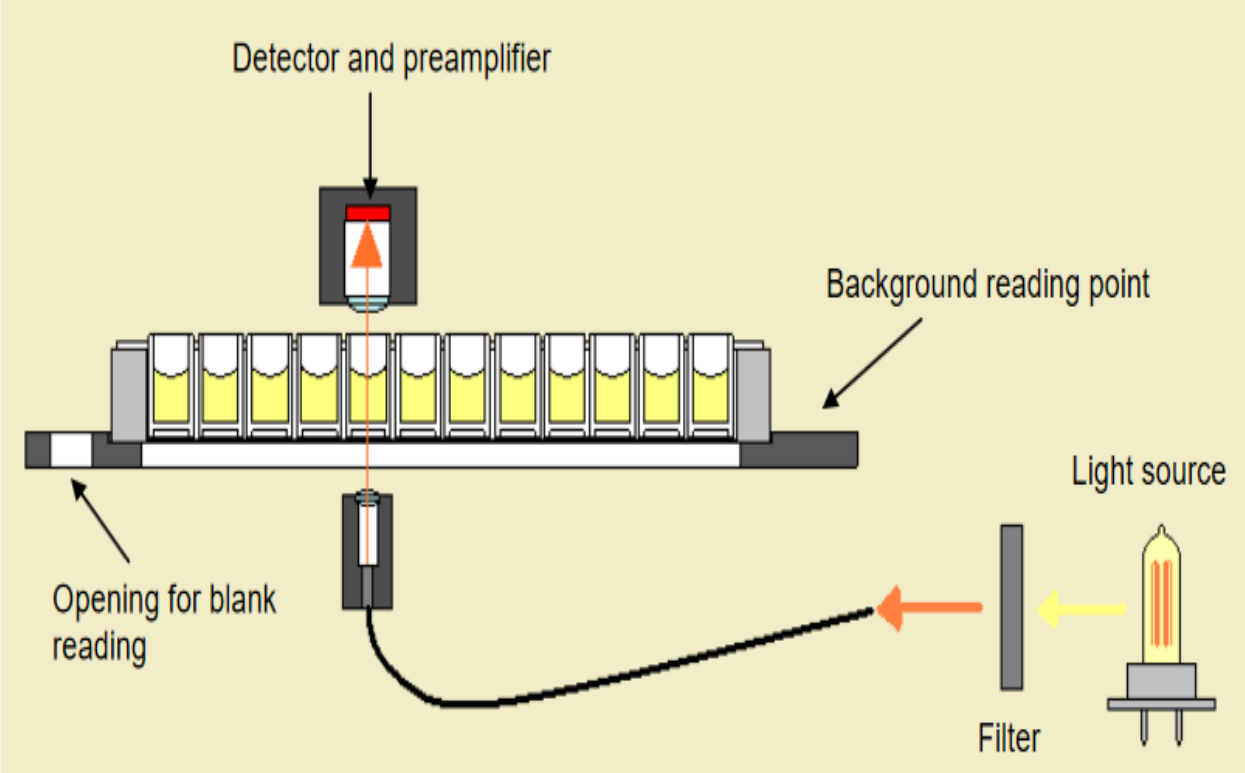

Figure 4.13: The optical system of the Multiskan FC instrument.[65]

Figures 4.14 and 4.15 depict plate one and plate two, respectively, in which the blue circles represent cell wells irradiated by 0.5 Gy (plate 1) and 1 Gy (plate 2) while orange ones are non-irradiated (controls). Approximately 10,000 cells were seeded each well, which was imaged before and after irradiation for the confluence of approximately 60%.

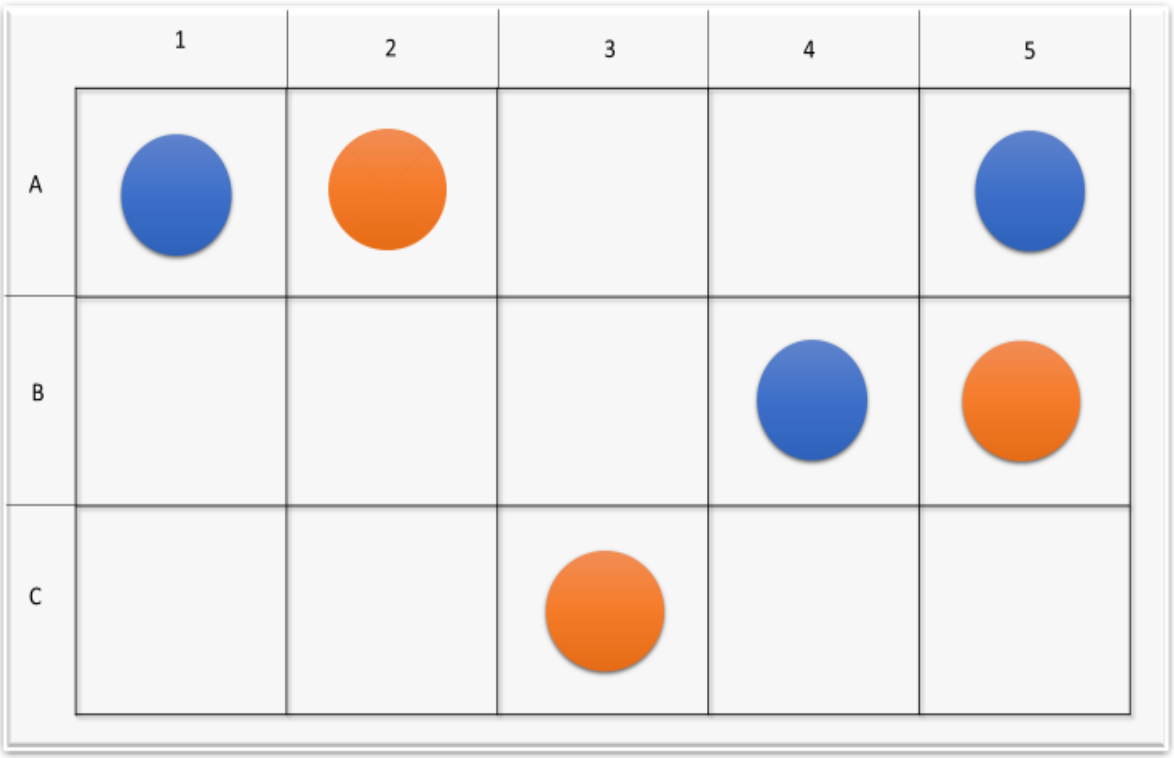

Figure 4.14: Plate one in which the cell is exposed to 0.5 Gy of the proton beam.

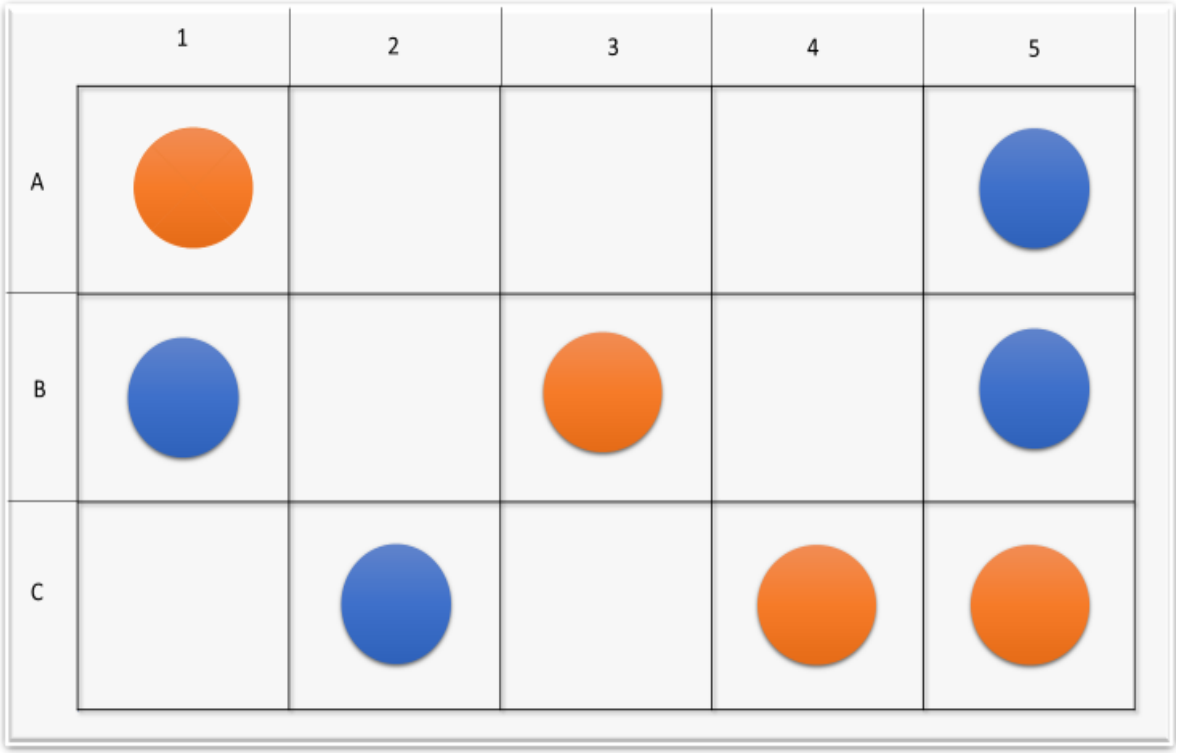

Figure 4.15: Plate two in which the cell is exposed to 1 Gy of the proton beam.

4.4 Cell Survival Curve:

A cell survival curve describes the connection between radiation dose and the proportion of cells that survive. Cell survival values have been determined using 3 MeV irradiated controls to identify whether cell doses are correct and fitted with the linear/quadratic model. The cell survival curve expression is:

$$S = e^{-(\alpha D + \beta D^2)} \quad \text{..... (20)}$$

Where S denotes the fraction of cells surviving, α and β are constants, radiosensitivity coefficients, in which α predominating at a low dose and β at high dose, while D represents the dose measured in Gy. The linear-quadratic model proposes that cell killing by radiation has two segments: proportional to dose, and the second is proportional to the square of the dose.

The linear portion dominates for higher LET radiation such as proton radiation, and a straight fit is observed. As a result, the survival curves in this experiment were perfectly straight. Two distinct segments typically have these curves for low LET radiation, with an initial linear portion transmitting them into a subsequent quadratic portion that creates a shoulder region that connects them.

4.5 Microbeam experimental:

The horizontal microbeam system is located inside the ECU accelerator lab. From object aperture to the Havar vacuum exit window, the whole beamline length of the ion beam is approximately 7.72 meters.

The focusing lens is an electrostatic quadruplet that produces a symmetrical beam spot. The individual electrodes are connected via wire connectors to four 5 kV high voltage feeds. The voltages at the quadrupoles are set in the -Y (inner elements), +Y (inner elements), -X (outer

elements), and +X (outer elements) configuration, which can balance the beam's convergence and the divergence of both horizontal and vertical axes.

The object distance is approximately 7.5 m, representing the distance between the beam object aperture and the front surface of the quadruplet lens. The image distance is approximately 15.24 cm, representing the distance between the end of the lens and the focal spot, as shown in figure 4.16. Thus, the lens and the vacuum brake sensor are only 1 cm apart.

A surface barrier detector has been installed to detect particles that have passed through the Havar exit window. The imaging system includes horizontal assembly microscopy coupled with a fast frame rate VGA monochrome scientific camera with UV-enhanced CCD sensor, USB 3.0 (Thorlabs, Inc.).

The alignment of the beamline focusing components is one of the essential aspects of the microbeam. These components must be in alignment with each other within less than a millimeter. Also, essential to align is the micro aperture. For a good start, vacuums should be about 10^{-8} torrs.

There are different producers to measure the beam size:

1- Knife-edge method.
2- CR-39 plastic nuclear track detector.
3- 50 µm Tungsten wire.

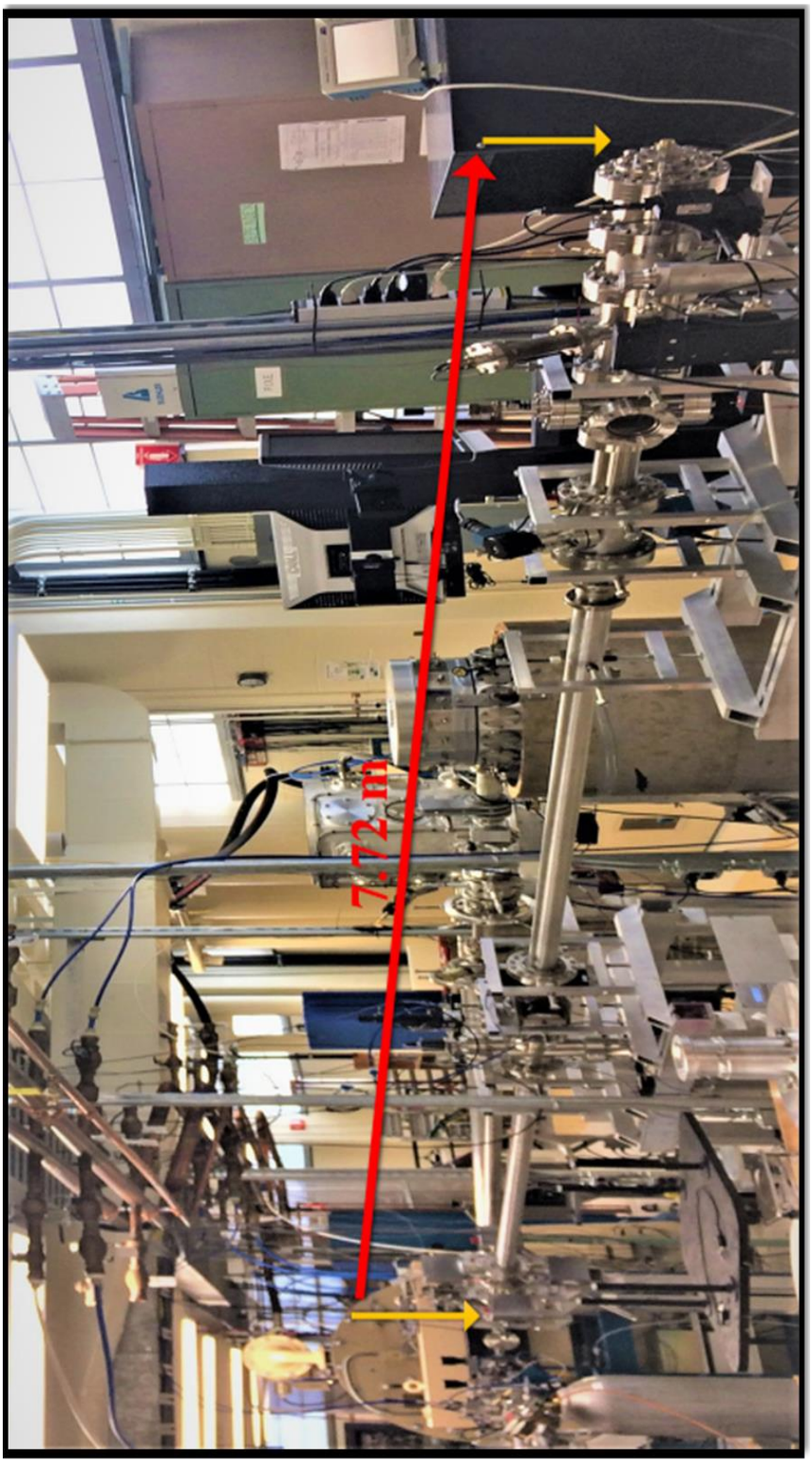

Figure 4.16: The total length of horizontal microbeam system.

4.6 The knife-edge technique:

It is a process that provides rapid, reasonable, and accurate beam size. For decades, the knife-edge technique has been widely used to describe Gaussian laser beams, and it is now regarded as a standard Gaussian laser beam characterization method. It is often used to characterize the beam profiles, focused optical spots, and optical surfaces. [64]

The sharp knife edge plate scans the beam, and the beam blockage rates are counted at each step. The strips move perpendicular to the direction of the generation beam. The total count per second is measured as a function of the knife-edge position. The beams' sizes were measured using the knife-edge technique. The material must be dense enough to affect the beam measurably while remaining thin enough to distort the beam characteristics. [55]

The measurable change in detection rate determines the number of counts of the beam enclosed. The knife-edge is crossed through the beam, and the beam blockage rates are counted at each step. The accurate stage movement with 0.1 μm per step was exploited to scan a thin copper metal strip with a sharp edge vertically and horizontally across the beam at the focal plane spot. As the thin metal knife-edge strip moves to eclipse the beam, particles that impinge on the surface are stopped so that the detected particle signal changes to a single-dimensional beam profile, as shown in figure 4.17.

For a Gaussian beam, the equation is:

$$\text{Gaussian beam} = \frac{e^{-\frac{x^2}{\sigma^2}}}{\sqrt{2\pi}\sigma} \quad \ldots\ldots\ldots\ldots\ldots\ldots (21)$$

The knife-edge measurement would be:

$$\text{Knife} - \text{edge} = \int_{-\infty}^{x} \frac{e^{-\frac{x'^2}{\sigma^2}}}{\sqrt{2\pi}\sigma} dx' \quad \ldots\ldots\ldots\ldots\ldots\ldots (22)$$

The slope of the knife-edge is:

$$\text{Slope} = \frac{e^{-\frac{x^2}{\sigma^2}}}{\sqrt{2\pi}\sigma} \quad \ldots\ldots\ldots\ldots\ldots\ldots\ldots\ldots\ldots\ldots (23)$$

By finding the slope of the knife-edge, the beam size can be calculated.

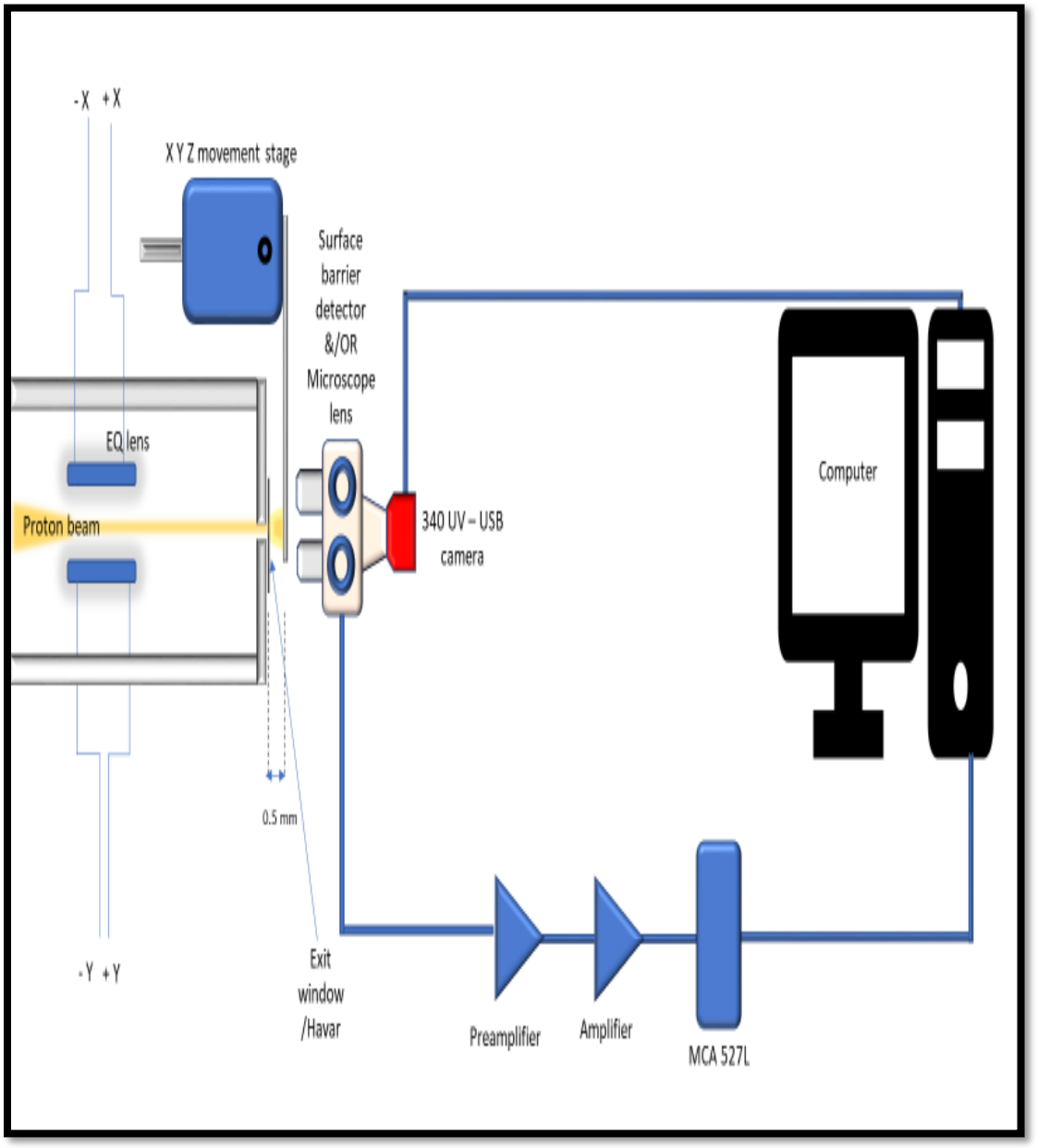

Figure 4.17: Schematic of the particle counter system for detecting particles passed through the microbeam exit window.

4.7 Exit windows:

Two exit windows designs were used with different diameters and distances from the lens's aperture to the exit beam aperture. The first one has a 2 mm diameter and 63.5 mm distance from the lens's aperture to the exit window aperture, and the second one has a 1 mm diameter and 152.4 mm distance, as shown in figure 4.18, 4.19.

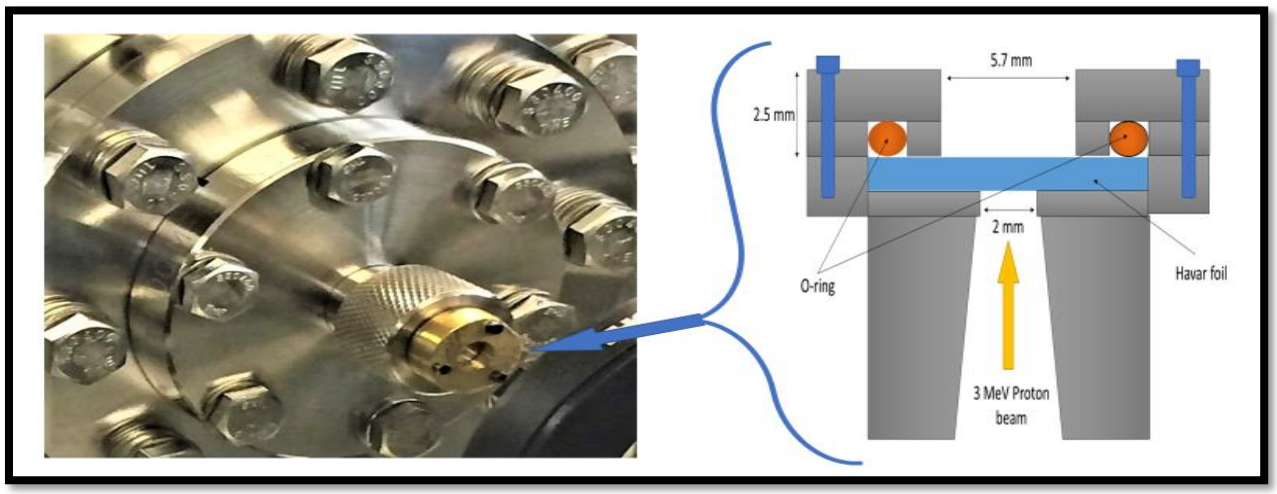

Figure 4.18: The first exit window.

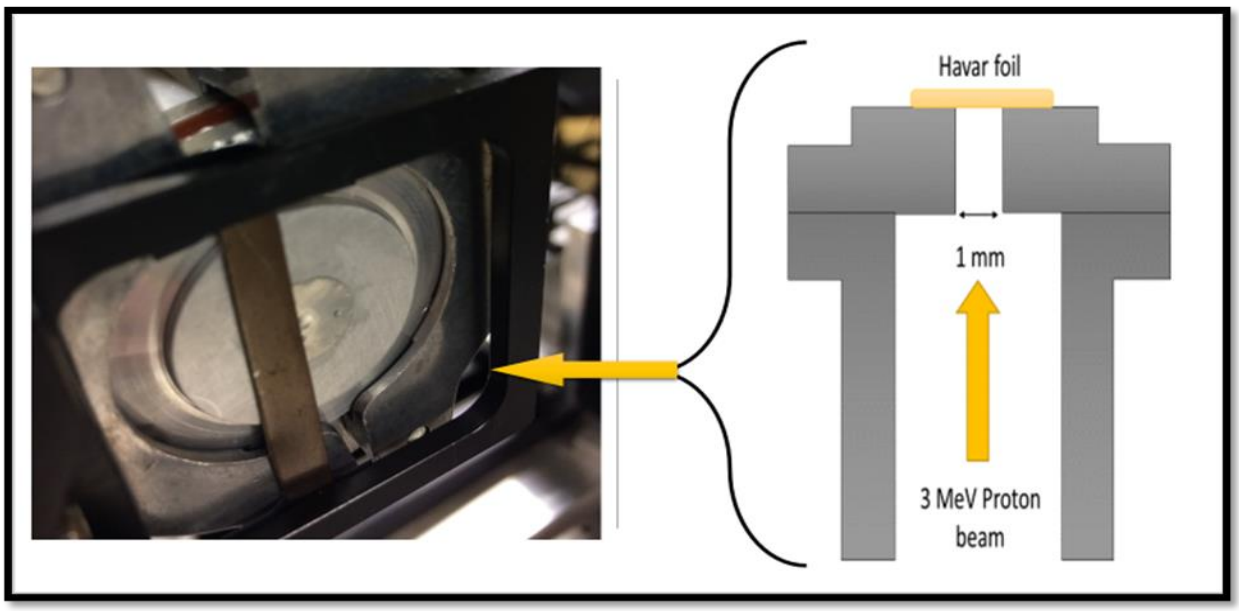

Figure 4.19: The second exit window.

Chapter Five
Results and Conclusions

5.1 Dose Result:

The dose is calculated with the cell's midpoint after calculating energy loss through the different materials. The dose rate is calculated with the following equation at the cell middle point.

$$\dot{D} = \textbf{Mass Stopping Power} \times 1.6 \times 10^{-7} \times \textbf{Fluence Rate} \quad \ldots\ldots\ldots (24)$$

Dose rate measures in the unit of (Gy/sec), mass stopping power measures in the (MeV x cm^2/mg) unit, fluence rate is measured in 1/ (cm^2 x sec), 1.6 x 10^{-7} is a conversion factor to convert (MeV/mg) to Gy (J/kg), the standard unit of dose as shown as an example in tables 2 and 3.

	Energy (MeV)	Density (mg/cm^3)	Stopping power ($MeV.cm^2.mg^{-1}$)	LET (MeV/ cm)	Thickness (cm)
Havar	3	8.67E+03	6.32E-02	547.95	1E-03
Air	2.452	1.63E+00	1.01E-01	0.16463	1E+03
Mylar film	2.176	1.4E+03	1.417E-01	198	2.5E-04
Cells	2.13	1.09E+03	1.5E-01	170.04	2.5E-04
Midpoint	2.08	1.09E+03	1.50001E-01	170.04	2.5E-04
Fluence		6.13E+09 ($cm^{-2}.sec^{-1}$)			
Current		0.981E-09 A			
Dose Rate		1.53E-01 Gy/sec			

Table 2: Calculation stopping power and energy for Havar, Mylar film, air, and cells.

The Havar Foil's stopping power of 6.32 x 10^{-2} (MeV. cm^2/mg), applying 3.0 MeV proton energy, was calculated by the SRIM software. Havar foil and air are energy-dependent on their stopping power and thus LET. Therefore, by multiplying the stopping power by the density, the LET can be calculated from the stopping power.

The LET is multiplied by the foil thickness, which is 10 µm, to calculate the energy loss in the foil. Thus, the average energy lost by protons in the Havar foil was recorded to be 0.5479 MeV,

decreasing the proton's average energy to 2.452 MeV. The 2.452 MeV energy was applied using SRIM production and identical measurement techniques to measure the energy lost in the air. On entering the cells, these protons had average energy of 2.13 MeV. Thus, the average loss of proton energy in the air was 0.322 MeV for 1.176 cm. Figure 5.1 shown a **3** MeV proton beam transmits through Havar foil, Mylar film, air, cells, and growth media. The proton beam loses its energy in approximately 79 µm in the growth media.

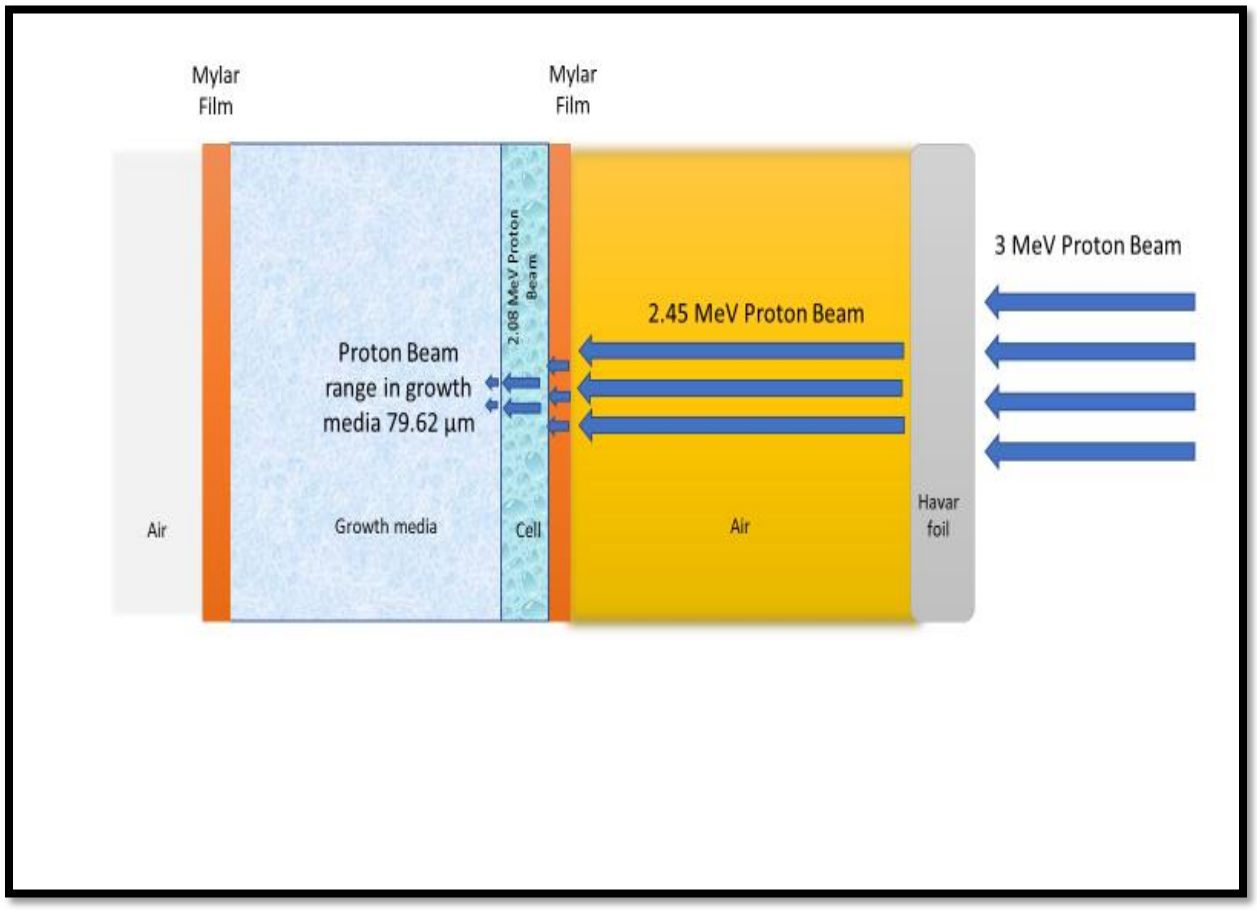

Figure 5.1: The 3 MeV proton beam transmits through Havar foil, Mylar film, air, cells, and growth media.

The particle fluence rate, which defines the number of protons per unit of cross-sectional area per time, is calculated using the beam current from the Faraday cup. Next, SRIM is used once more to calculate the proton energy and the mass stopping power in the midpoint of the cell. Finally, the dose rate in Gy per sec is calculated using the LET result on the cell's midpoint and the fluence

rate. Thus, the time required to irradiate the desired dose is determined by dividing the desired dose directly by a dose rate.

Together with the cell cultures, the custom plates are then transported to the ECU accelerator lab, where they are irradiated for the time required to deliver the target dose. Table 3 shows an example of the calculation of the total dose time for irradiated cells. The uncertainty of determining the dose is approximately 0.0001667.

Dose (Gy)	Total time (sec)
0.1	6.53E-01
0.2	1.31E+00
0.3	1.96E+00
0.4	2.61E+00
0.5	3.26E+00
1	6.53E+00
2	1.31E+01
3	1.96E+01
4	2.61E+01
5	3.26E+01
6	3.92E+01
7	4.51E+01
10	6.53E+01
20	1.31E+02

Table 3: Calculation of total time of the dose.

The dose is utilized to determine the correct period for beam exposure in the cells to the required radiation dose. The specimens could then be exposed via the Faraday cup, which controls the duration it stays open as an (open-close) shutter.

5.2 PrestoBlue assay result:

The PrestoBlue reagent has a blue-colored and virtually non-fluorescent cell-permeable compound. When applied to the cells, the PrestoBlue reagent alters the viable cell environment, turns red, and converts highly fluorescent. This modification can be detected by measuring absorption.

The absorption rates of non-irradiated MCF7 cells and irradiated MCF7 cells are displayed in Figure 5.2. By normalizing the fold, the absorption rate is determined. The fold compares the non-irradiate cells to the cells 24 hours after irradiation.

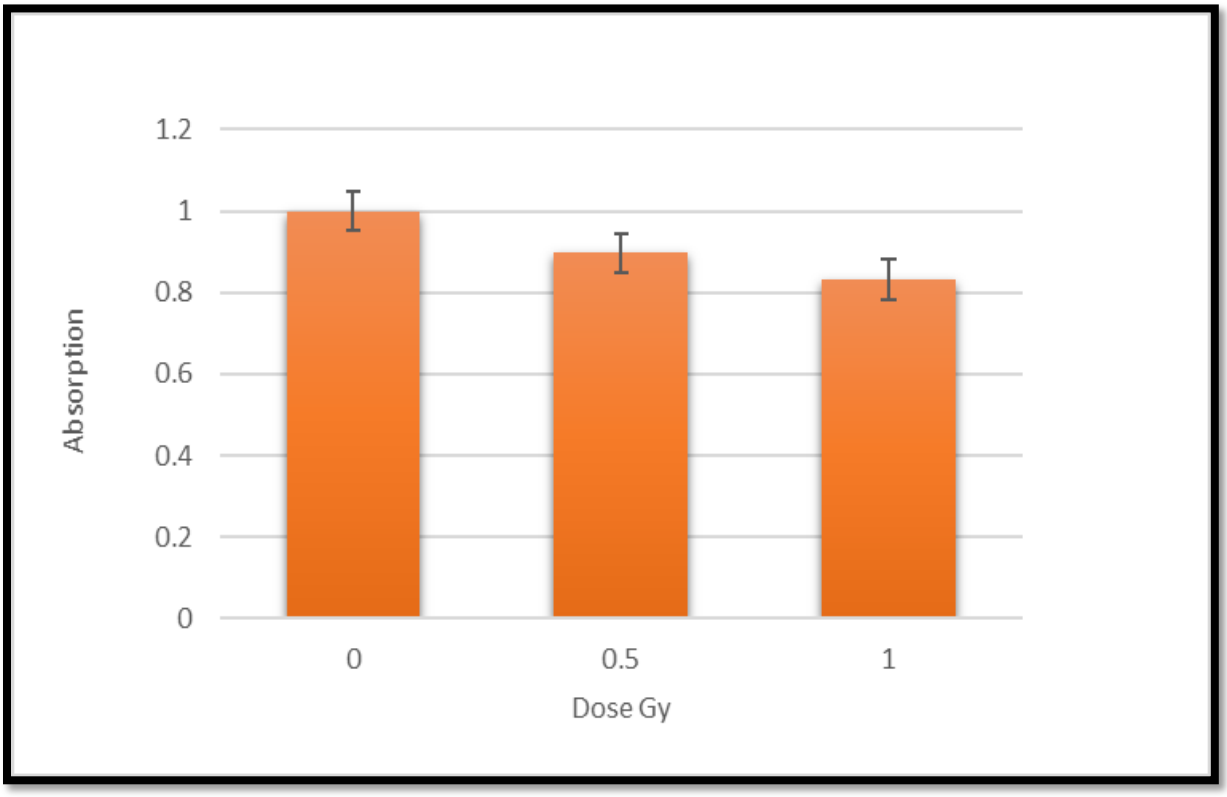

Figure 5.2: The absorption of the MCF7 cells.

Figure 5.2 also shows that increasing the radiation dose will raise the death of MCF7 cells. This can appear in 0.5 Gy and 1 Gy bars, depending on the normalization of the non-irradiated cell to irradiate cells, and the PrestoBlue reagent is little modified by the reducing environment of the viable cell and not turns red, and will not become highly fluorescent, due to reduction in the number of cells.

Figure 5.3 depicts the 3 MeV survival curve. The plot was fitted with a linear quadratic equation using the least-squares method, yielding an adjusted R^2 value of 0.981. Since the small number of trials (n = 3) for each data point, the adjusted R^2 value was used.

Previous studies with protection and sensitization of human cells to proton radiation and protons of relative LET show this similar straight fit characteristic using MCF7 cells and V79 cells [37, 66]. The LD_{50} was found to be 3.797 Gy, based on this curve.

This survival curve is not overwhelming, and it is enough to provide an estimated initial dose for this study. The decisions will occur based on the LD_{50} mark to expose the cell line to a level that is most marked by a graphical decline in survival due to sensitization from an experimental treatment.

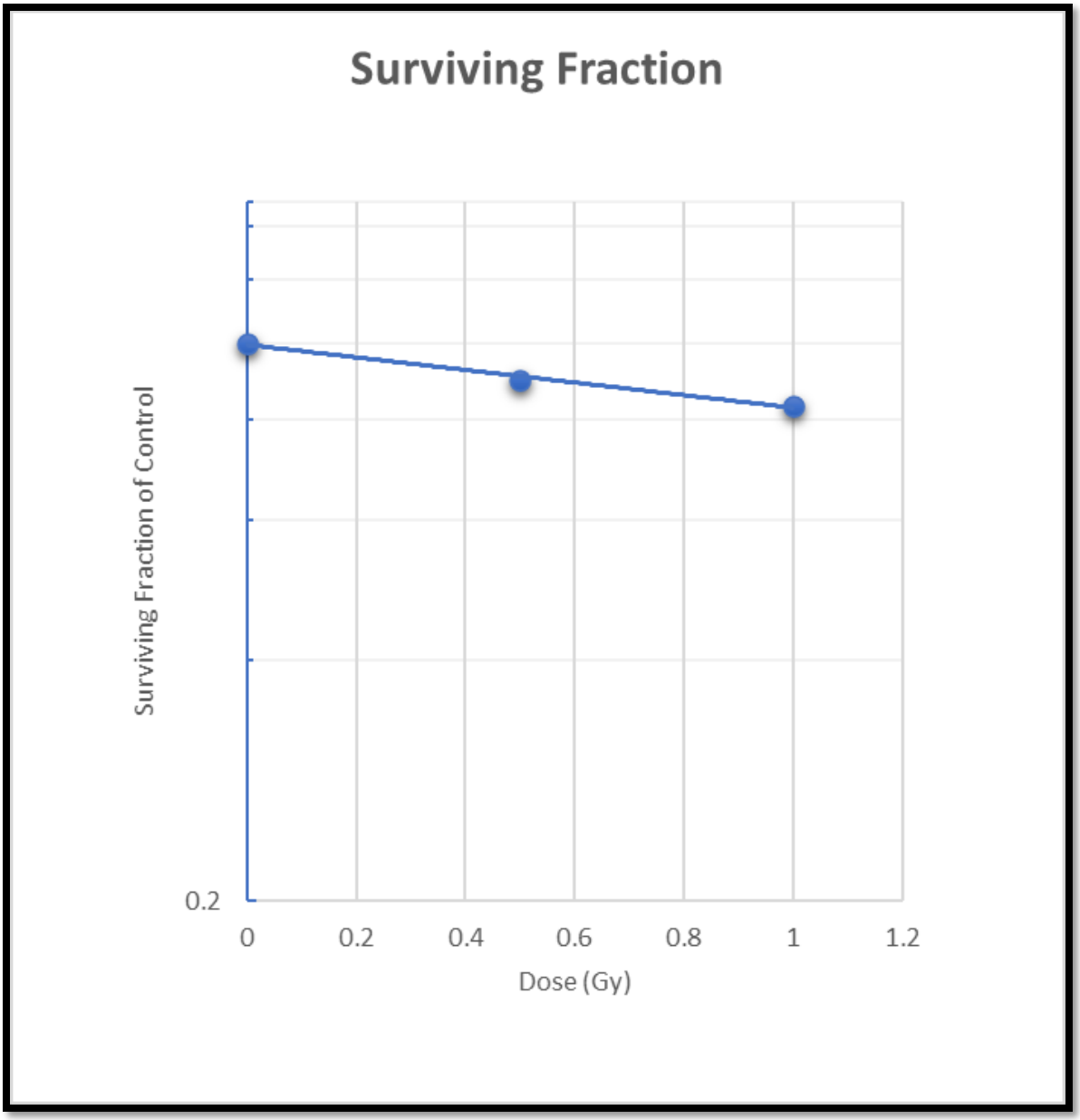

Figure 5.3: the survival curve of the MCF7 breast carcinoma cell line after being exposed to 3 MeV incident protons. The PrestoBlue assay was used to collect this data, then plotted on a semi-log plot using the linear-quadratic model (mean standard error).

5.3 Microbeam results:

5.3.1 The first exit window measurements:

The proton beam (3 MeV) spot profile was measured through the exit window with the surface barrier detector. The beam spot profile was measured using equation (23) with different voltage applications on the electrostatic quadrupole lens, as shown in table 4 and figures (5.4, 5.5, 5.6, 5.7, 5.8, 5.9, 5.10).

Strength KV	Balance	Beam size X mm	Beam size Y mm
0	0	2.442	2.615
1.75	20	1.133	1.261
1.75	50	1.122	1.4081
2.5	40	1.321	1.327
2.5	60	1.1733	1.406
2.5	70	1.74	1.98
2.8864	28.51	0.636	0.9623

Table 4: The beam size measured with various voltages.

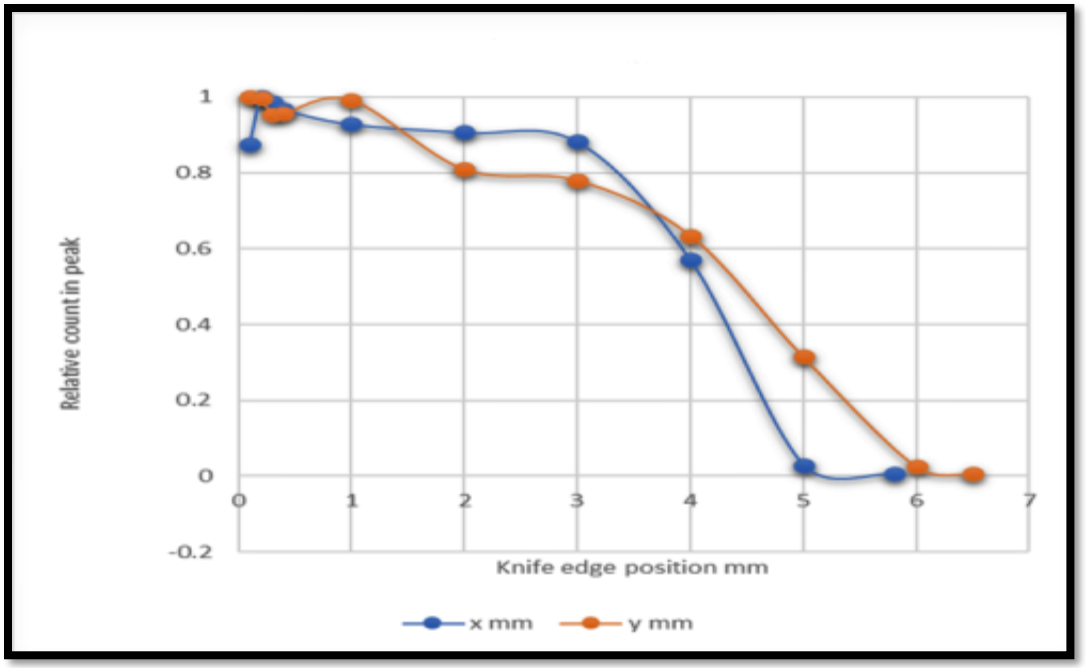

Figure 5.4: The voltage is 0 KV (Strength) and 0 Balance.

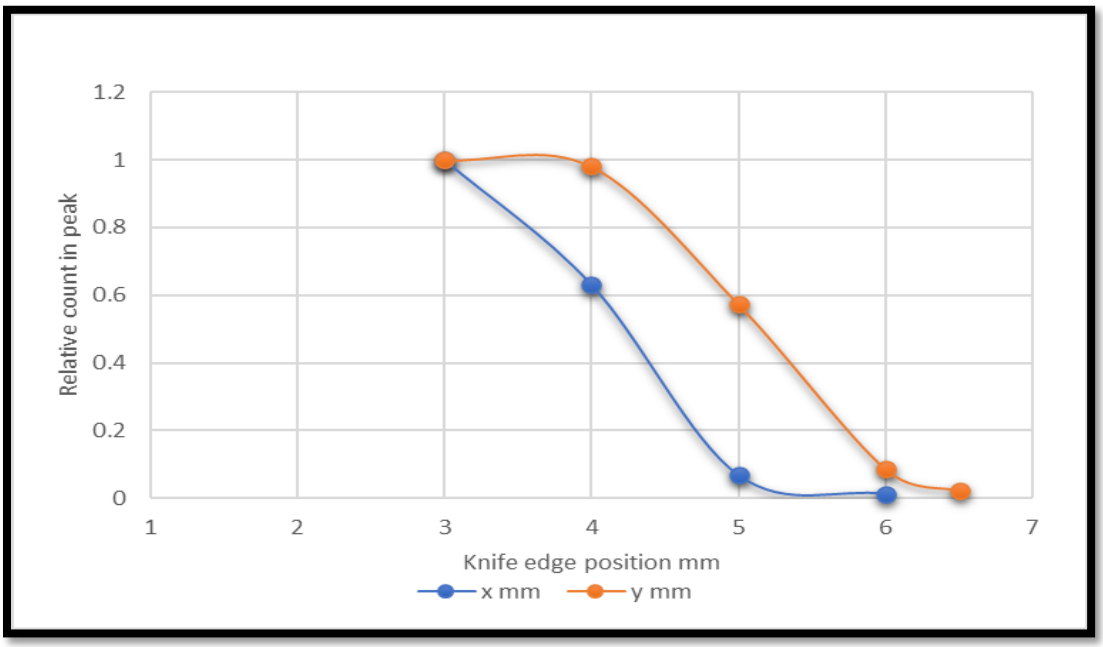

Figure 5.5: The voltage is 1.7 KV (Strength) and 20 Balance.

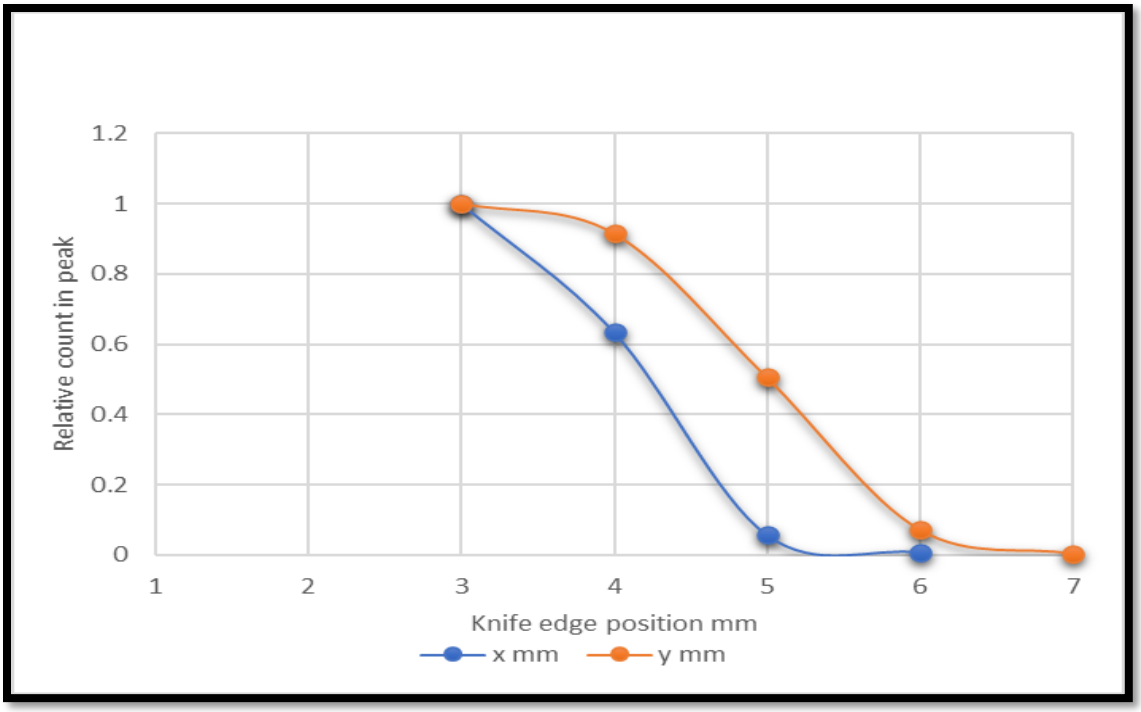

Figure 5.6: The voltage is 1.75 KV (Strength) and 50 Balance.

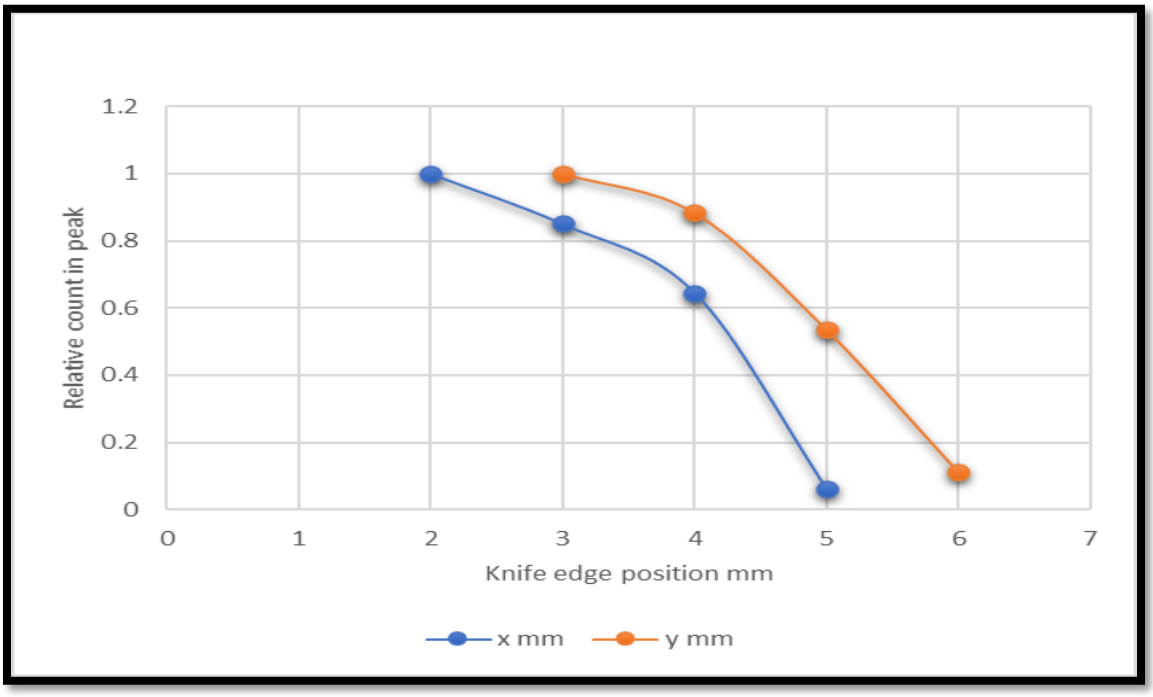

Figure 5.7: The voltage is 2.5 KV (Strength) and 40 Balance.

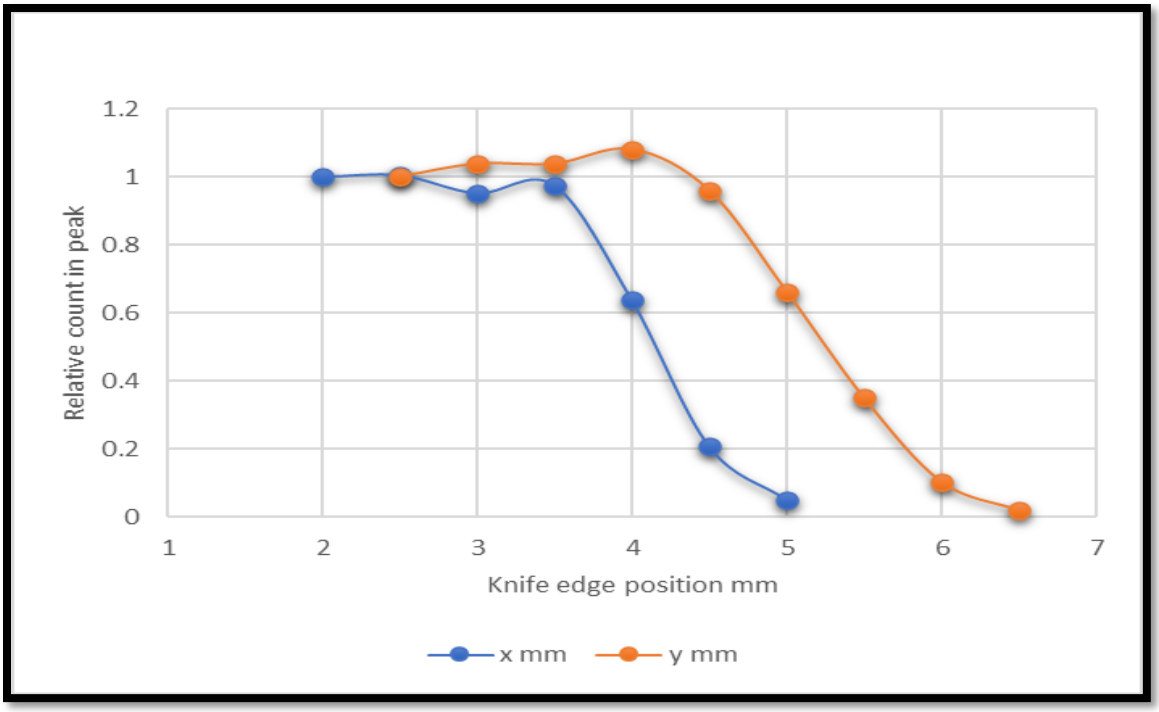

Figure 5.8: The voltage is 2.5 KV (Strength) and 60 Balance.

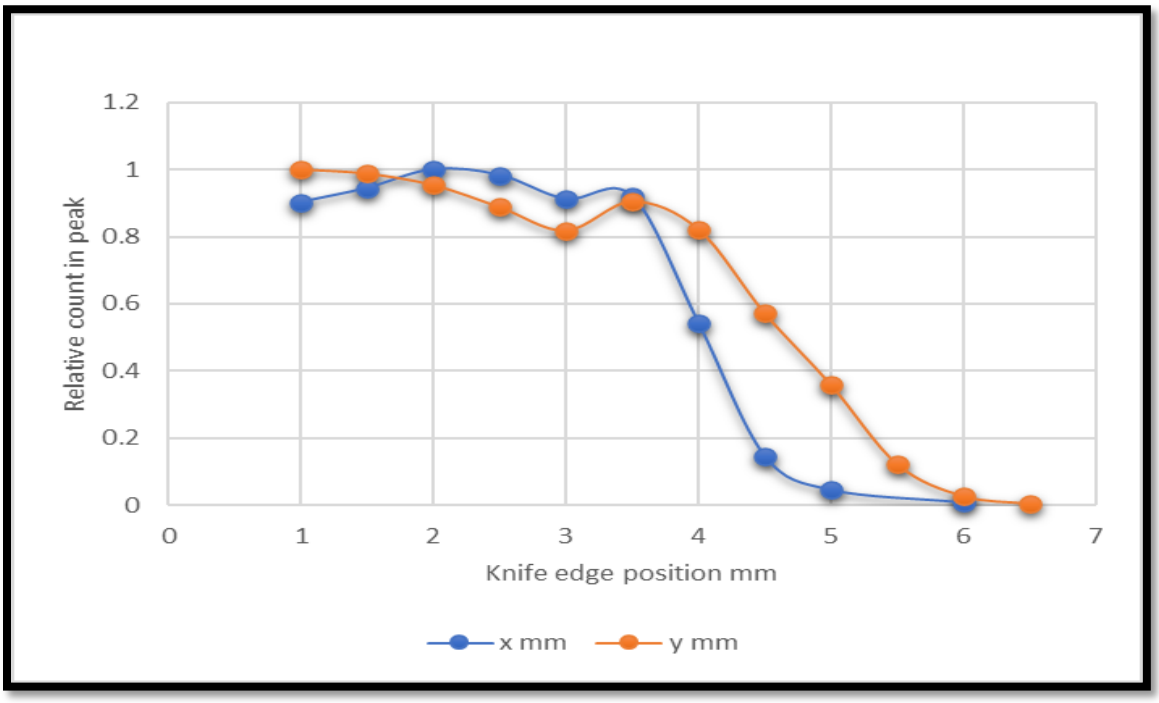

Figure 5.9: The voltage is 2.5 KV (Strength) and 70 Balance.

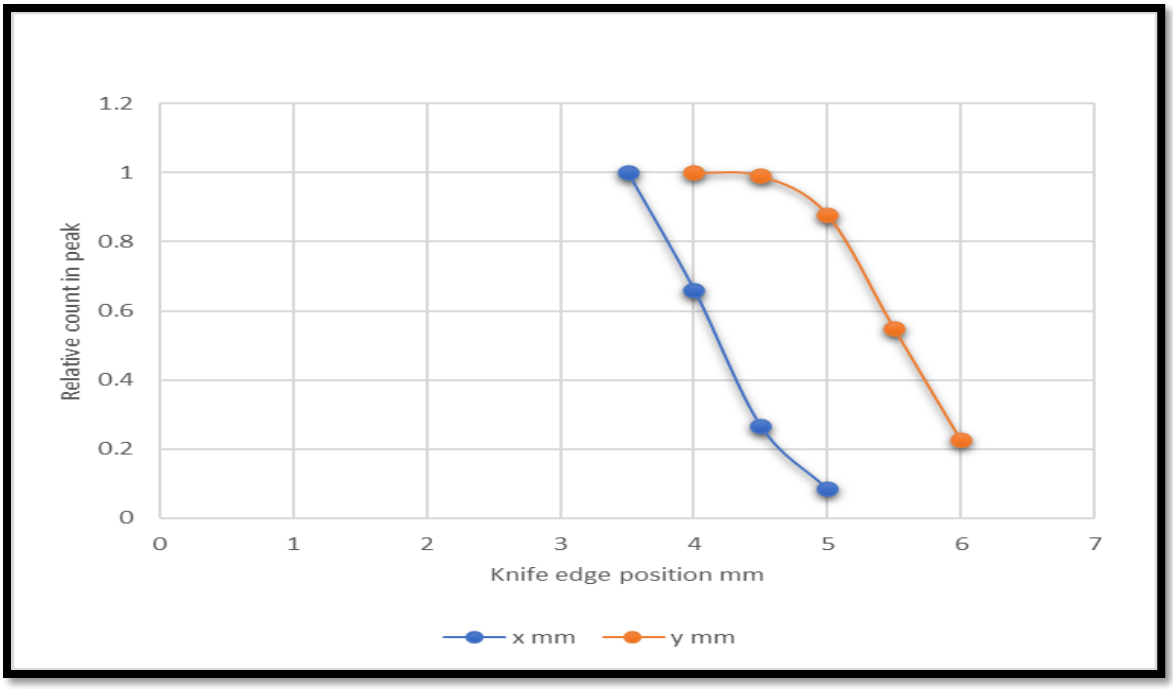

Figure 5.10: The voltage is 2.8864 KV (Strength) and 28.51 Balance.

Table 4.3 shows that the minimum beam size results from applied 2.8864 KV and 28.51 voltage the EQ lens was about 0.636 by 0.9623 mm.

Dependent on this result and the beamline simulation using SRIM code (figures 5.11, 5.12), explicitly, the required distance for getting proton beam in micrometer size from the exit window based on the exit window thickness should be less than 0.5 mm.

So, the microbeam in micrometer size will be lost within the exit window since the distance from the Havar foil to the end of the exit window holder is about 2.5 mm, as shown in figure 4.18.

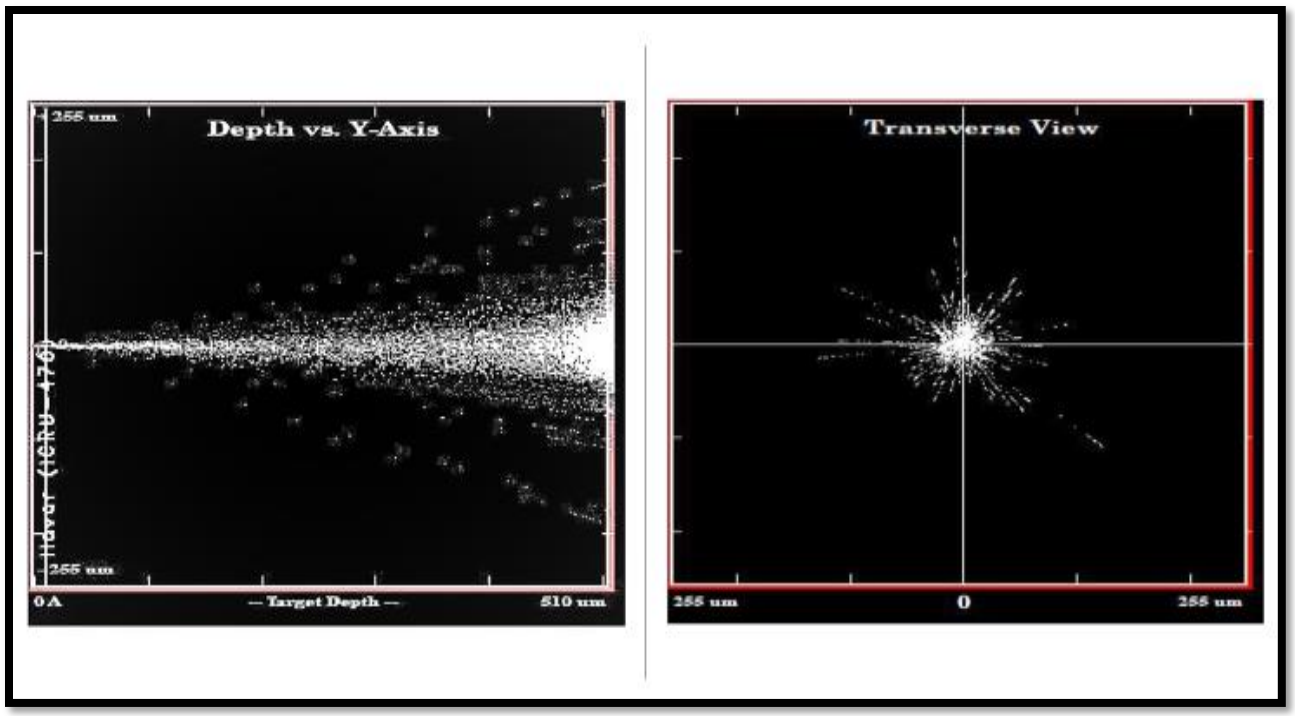

Figure 5.11: SRIM simulation for the 3 MeV proton beam 0.51 mm from the exit window.

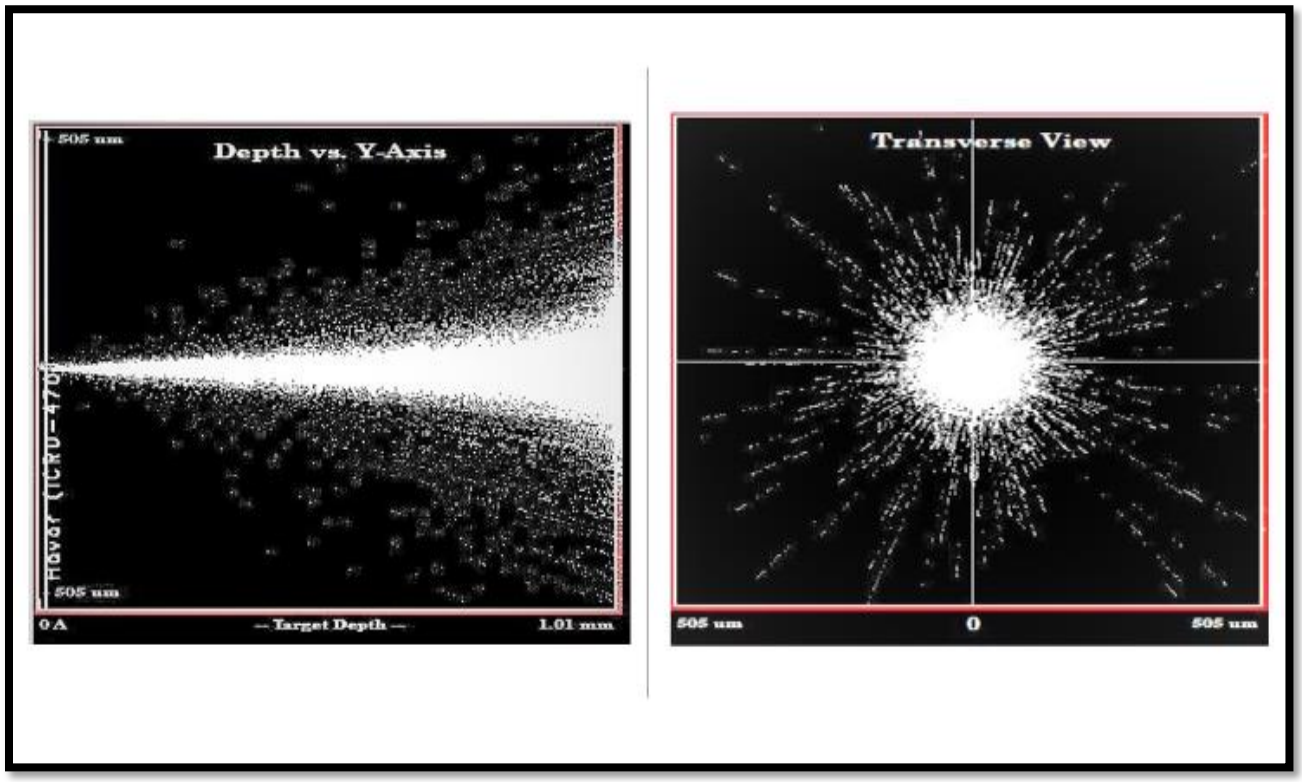

Figure 5.12: SRIM simulation for the 3 MeV proton beam 1.01 mm from the exit window.

5.3.2 The second exit window measurements:

The new exit window with a 1 mm diameter (figure 4.19) was replaced approximately in the lens focal point. The new design allowed a closer distance from the exit window to the target to be about 0.5 mm, as recommended by the SRIM code simulation. The beam spot profile was measured using equation (23) with different voltage applications on the electrostatic quadrupole lens and slits area, as shown in table 5 and figures 5.13, 5.14, 5.15, 5.16.

Voltage KV	Balance	Slits mm^2	Beam size (X mm)	Beam size (Y mm)
1.1124	50.96	5 x 5	0.8311	0.88
2.035	68.77	5 x 5	0.7532	0.74
2.45	68.73	5 x 5	0.739	0.73
2.4	68.73	1 x 1	0.14277	0.14655

Table 5: The beam size measured with various voltages and slits area.

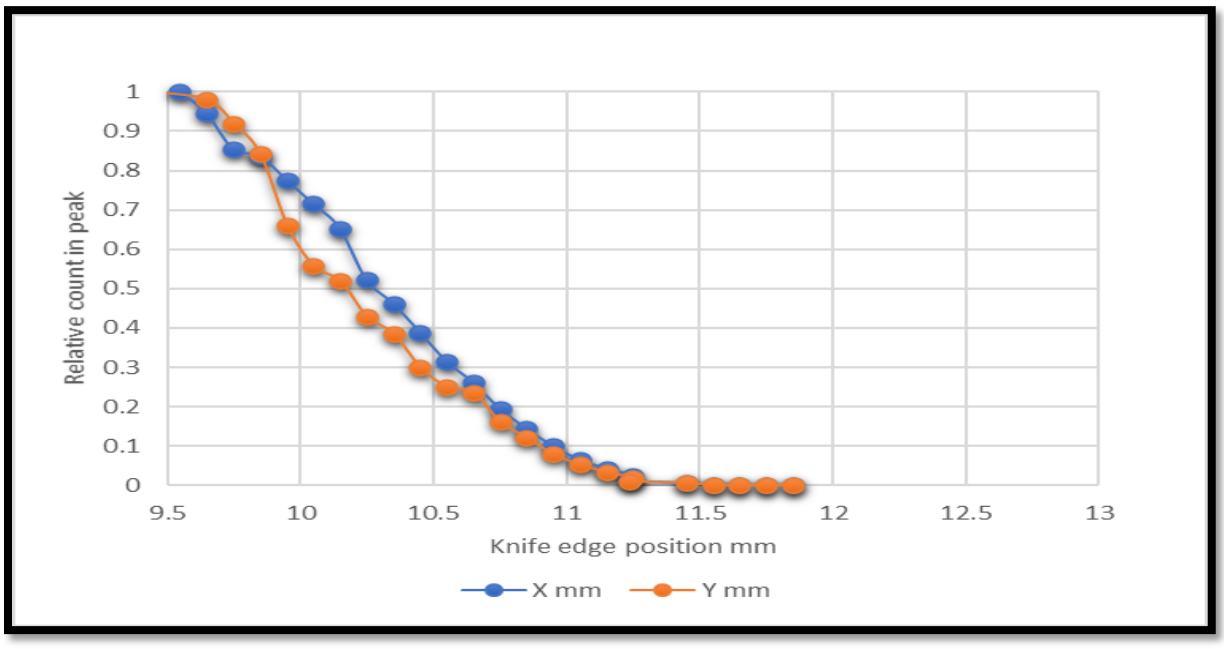

Figure 5.13: The voltage is 1.1124 KV (Strength), slits area 5x5, and 68.73 Balance.

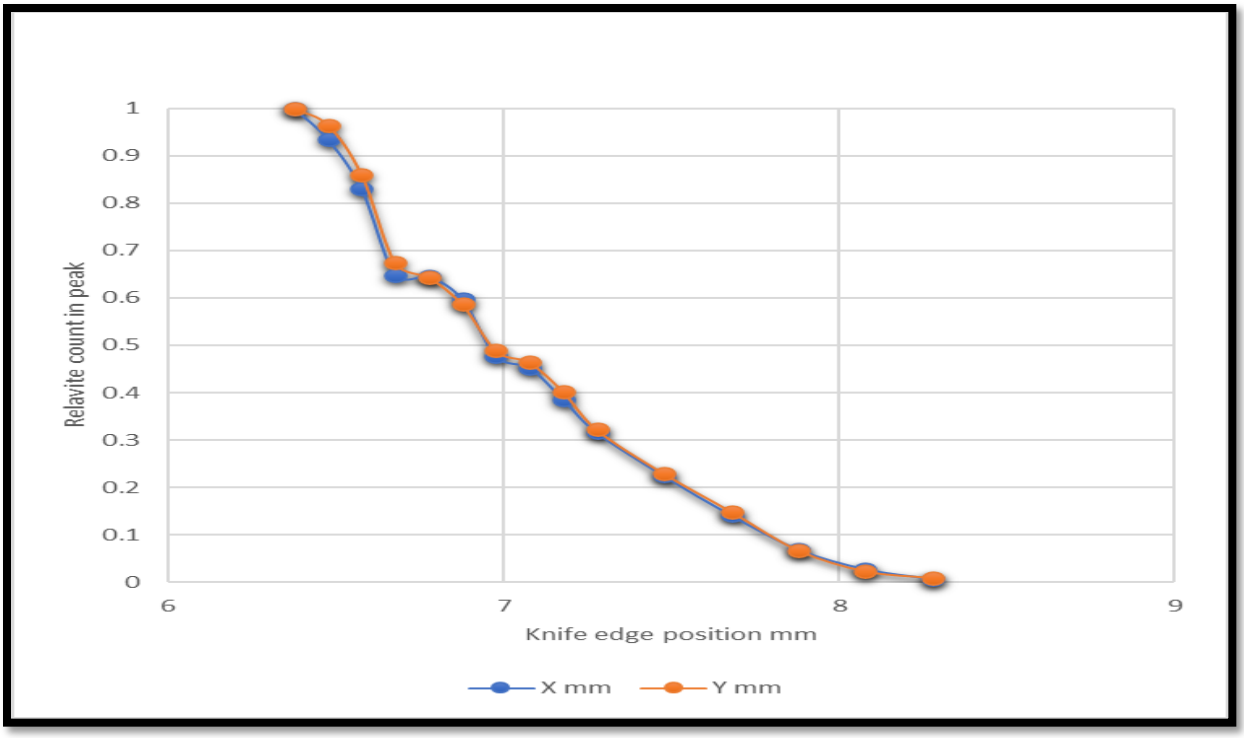

Figure 5.14: The voltage is 2.035 KV (Strength), slits area 5x5, and 68.73 Balance.

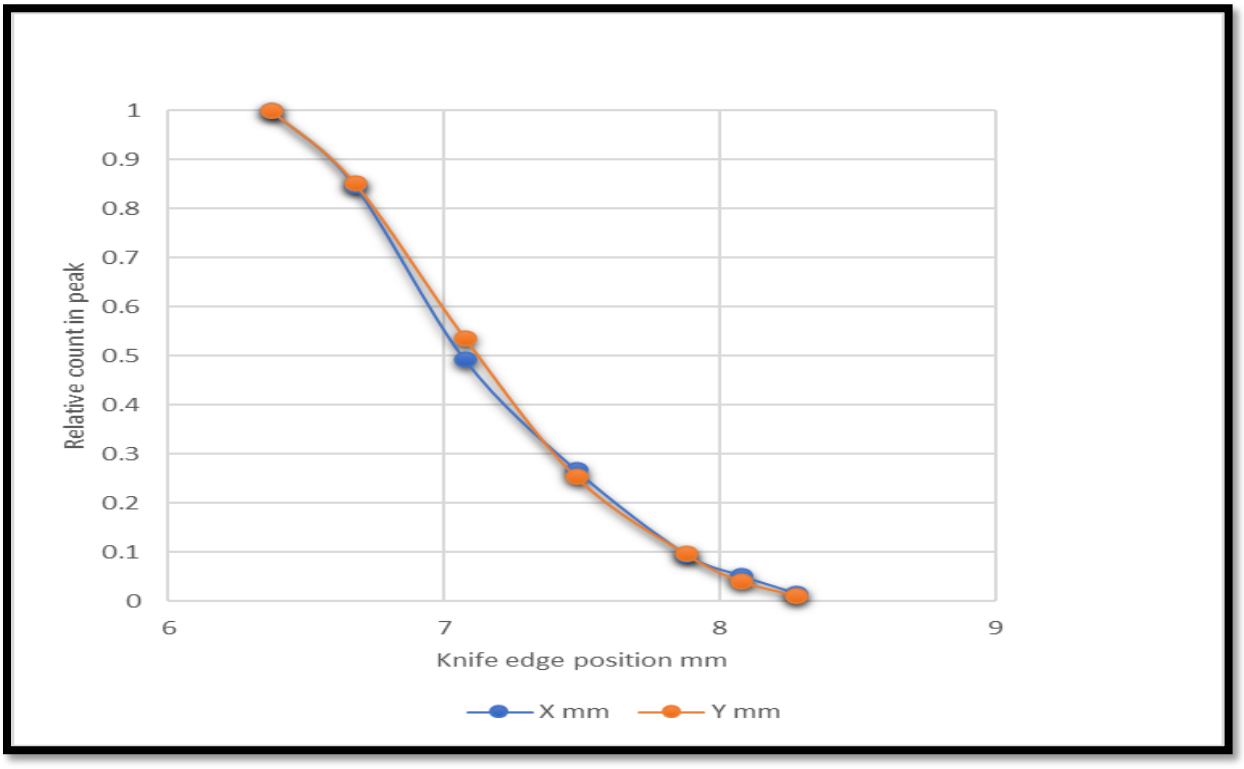

Figure 5.15: The voltage is 2.4451 KV (Strength), slits area 5x5 and 68.73 Balance.

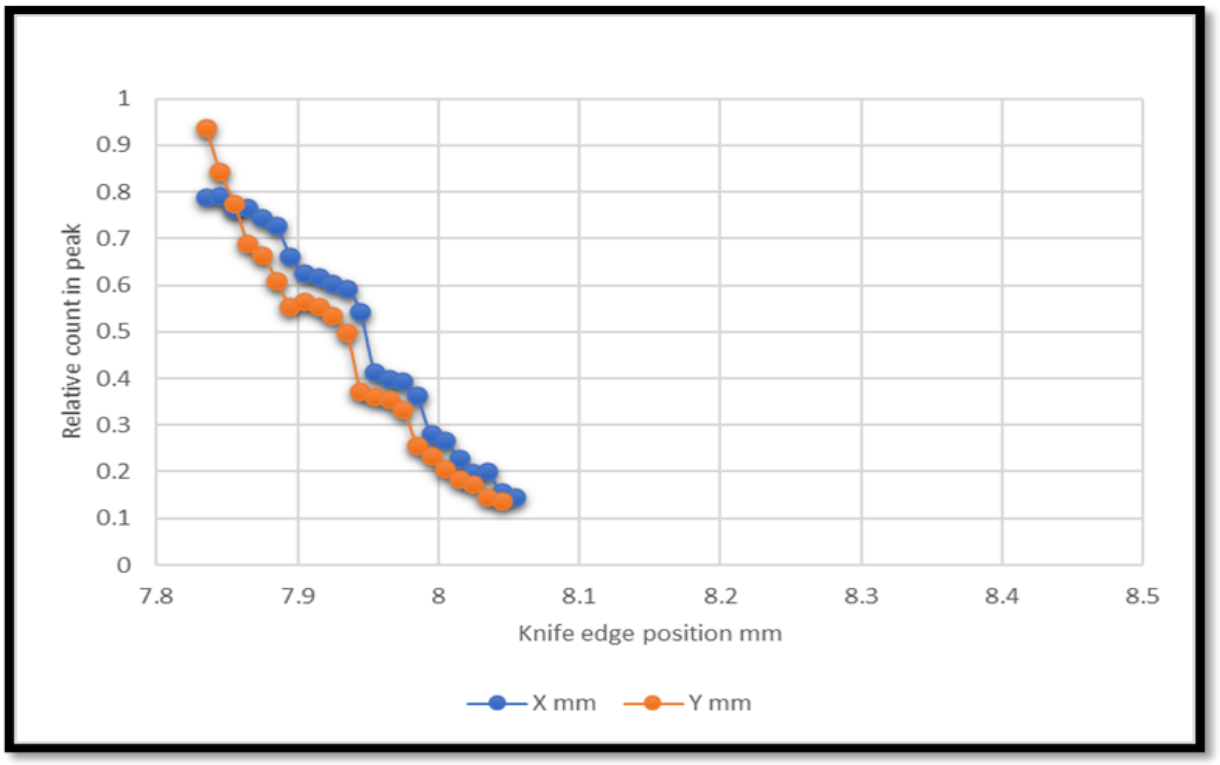

Figure 5.16: The voltage is 2.4 KV (Strength), slits area 1x1, and 68.73 Balance.

Knife-edges were utilized to measure the diameter of the charged particle stream. A thin material strip moves through the beam in two orthogonal directions via a motion phase of 0.1 µm resolution. The layer is thin enough to diminish but not halt the beam's energy, allowing a silicon surface barrier detector to detect the transmitted ions. As an escape window, 10 m thick Havar foil was employed.

Demagnification should be achieved whenever the object aperture is aligned with the lens, and the voltage of the lens elements is configured. The beam width measurements in the X and Y stage directions are taken with various sets of small lens voltages.

The minimum beam spot scans of 142.77 µm in the X direction and 146.55 µm in the Y direction for 3 MeV proton ions were obtained using a 1 mm diameter exit aperture after precise adjustment: first, the lens voltages, second slits area, and third exit window design, as shown in table 5.

5.4 Future direction:

The scope of developing the radiation research area is extensive and distributed over various fields. Depending on the provided results, the L-15 beamline can be developed to contain multi experiments, which can be illustrated below:

1- The Havar foil used to keep the vacuum and provide minimal energy loss at the end of the beamline was sufficient. The thinner (2 -3 um) output window will reduce the beam size to tens micrometers, which is used in other similar experimental settings. This lets small structures such as the nucleus of cultured cells grow in a cell plate through a strain of energy ions generated in an accelerator and confined to a couple of microns in diameter.

2- The present horizontal microbeam is signifying developed to perform microanalysis (microPIXE), a new secondary particle microbeam (neutron microbeam), or micro soft X-ray, which all require a high initial ion beam (proton beam) current.

3- The use of proton radiation to investigate the use of nanoparticles as radiation sensitizers for tumor cells and as radiation protectants for healthy tissue with different ranges of dose.

4- Create a Carbon beam for doing experiments in the air using a 500 nm Silicon Nitride Membrane Window Si_3N_4 as an exit window that supports the experiment using a vacuum chamber, as shown in figures 5.17, 5.18 using SRIM simulation.

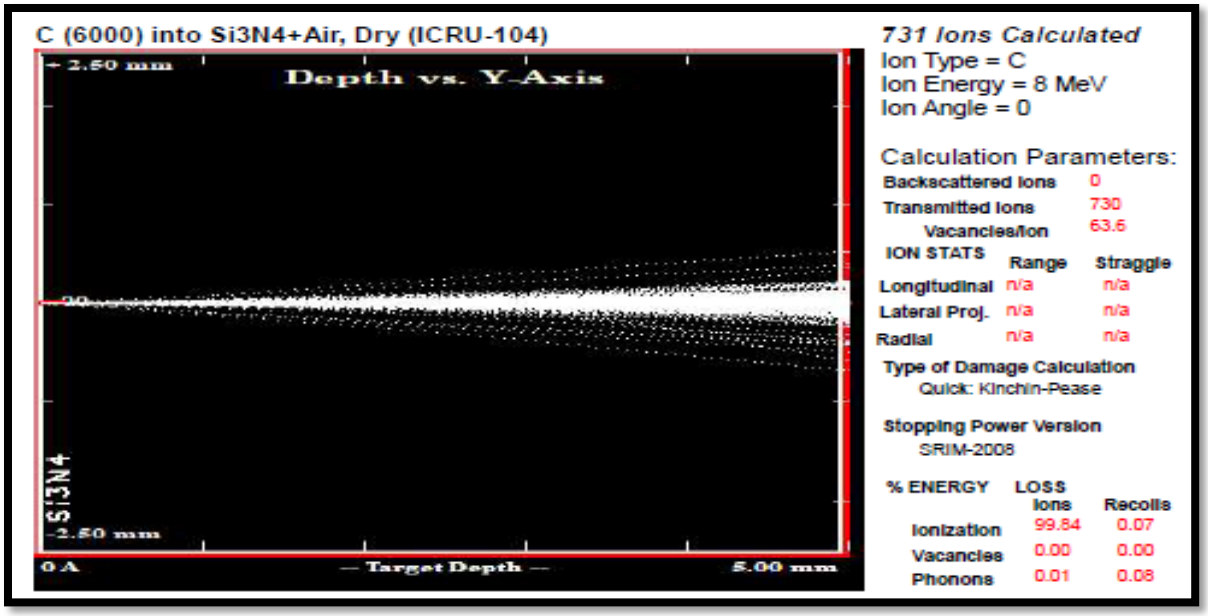

Figure 5.17: Carbon beam with 8 MeV energy passing through 500 nm Si_3N_4 exit window and transmitted 5 mm from the exit window.

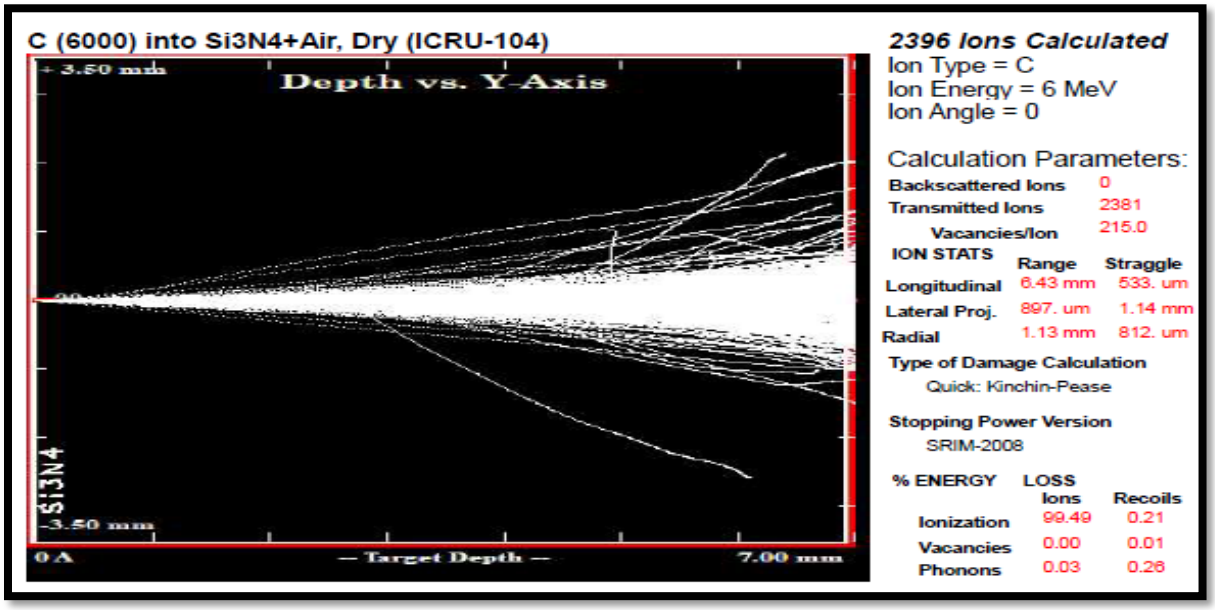

Figure 5.18: Carbon beam with 6 MeV energy passing through 500 nm Si_3N_4 exit window and transmitted 7 mm from the exit window.

References

1- *E. B. Podgorsak. "Radiation physics for medical physicists" second edition. Berlin; New York: Springer, 2006.*
2- *E. W. Webster, et al. "A primer on low-level ionizing radiation and its biological effects." 1986.*
3- *D.K. Avasthi, G.K. Mehta. "Swift heavy ions for materials engineering and nanostructuring." Springer Series in Materials Science, 145, 2011.*
4- *R. Castaing, Ph.D. Dissertation, "Application des sondes electroniques a une methode d'analyse poncuelle chimique et cristallographique", University of Paris, 1951.*
5- *H. E. Udeogu. "Quantitative micro-PIXE analysis using the GEOPIXE software." Thesis, the University of Louisiana at Lafayette. 2018.*
6- *J. W. Eisenmann. "Development of a proton-induced X-ray emission (PIXE) material analysis system" Thesis. East Carolina University, 2018.*
7- *R. E. Zirkle, and W. Bloom, Science 117, 487 (1953).*
8- *R. P. Perry. "Raymond Elliot Zirkle 1902–1988" Biographical Memoirs, Vol. 7.2005.*
9- *J.M. Khan, D.L. Potter, and R.D. Worley, Phys. Rev, 37, 564 (1966).*
10- *D.M. Khan, D.L., Potter, and R.D. Worley, Phys. Rev, 145, 23 (1966).*
11- *M. H. Kabir. "Particle Induced X-ray Emission (PIXE) Setup and Quantitative Elemental Analysis" Dissertation.The Kochi University of Technology. (Kochi, Japan).2007.*
12- *D.M. Poole and J.L. Shaw, in Proceedings of "the Fifth International Conference on X-Ray Optics and Microanalysis," edited by G. Mollenstedt K.H. Gaukler (Berlin, 1969), pp. 319.*
13- *T.B. Johansson, K.R. Axelsson, and S.A.E. Johansson, Nucl. Instr. and Meth, 84, 141 (1970).*
14- *S. A. E. Johansson, and T. B. Johansson, Nucl. Instr. Meth, 137, 473 (1976).*
15- *S. A. E. Johansson, J. L. Campbell, K. G. Malmqvist. "particle-induced X-ray Emission Spectrometry (PIXE)." volume 133, 1995.*
16- *Cookson, J. A., Ferguson, A. T. G., and Pilling, F. D. Proton microbeams, their production, and use. Journal of Radioanalytical Chemistry 12, 2 (Dec1972), 39-52.*

17- *D.N. Jamieson, G.W. Grime, and F. Watt. "The New Oxford Scanning Proton Microprobe Analytical Facility.". Nuc. Ins. and Met. in Physics Research (B40/41) (1989) 669-674.*

18- *J. A. Bearden, Rev. Mod. Phys., 39, 78 (1974).*

19- *The Radiological Research Accelerator Facility (RARAF) - the Center for Radiological Research (CRR) - Columbia University. www.crr.columbia.edu/raraf/our-research/microbeam. January 2021.*

20- *Y. Xu, G. R.P. Gerhard, S. A. Marino, A. W. Bigelow, M. S. Akselrod, J. Sykora, D. J. Brenner. "An accelerator-based neutron micro-beam system for studies of radiation effects." Radiat. Prot. Dosim. (2010), pp. 1– 4.*

21- *Nuclear Regulatory Commission. "Occupational Radiation Exposure at Commercial Nuclear-Power Reactors and Other Facilities"-1985. Eighteenth Annual Report, U.S. Nuclear Regulatory Commission NUREG-0713, Science Applications International Corporation (1988).*

22- *C. L. Lee, X. Zhou. "Thick target neutron yields for the Li-7(p, n)Be-7 reaction near threshold." Nucl. Inst. Meth. B. 152(1):1–11,1999.*

23- *A.W. Bigelow, G. R. Pehrson, G. Garty, C.R. Geard, Y. Xu, A.D. Harken, G. W. Johnson, and D.J. Brenner. "Ion, X-Ray, U.V. And Neutron Microbeam Systems for Cell Irradiation." AIP Conf. Proc. 1336, 351 (2011).*

24- *D. T. Goodhead. "Inactivation & mutation of cultured mammalian cells by aluminum characteristic ultrasoft X-rays III. The implication for a theory of dual radiation action." Int J Radiat Biol.; 32:43–70, 1977.*

25- *A. D. Harkena, G. R. Person, F. W. Johnson, D. J. Brenner. "The Columbia University proton-induced soft x-ray microbeam." Nucl Instrum Methods Phys Res B. 2011; 269(18).*

26- *F. H. Attix. "Introduction to Radiological Physics and Radiation Dosimetry." 1986.*

27- *J. E. Turner. "Atoms, Radiation, and Radiation Protection."Third Edition.2007.*

28- *H.H. Andersen and J.F. Ziegler, The Stopping and Ranges of Ions in Matter, Vol.2, Pergamon Press, New York, (1977).*

29- *J. F. Ziegler, U. Littmark, and J. P. Biersack, The Stopping and Ranges of Ions in Solid, Vol. 1, Pergamon Press, New York, (1985).*

30- *C. V. Sheth, "Relativistic corrections in k-shell ionization cross-sections." Phys. Rev. A 29 ,1151-1157, 1984.*

31- *J. M. Hansteen." Inner Shell Ionization by Incident Nuclei." Advances in Atomic and Molecular Physics Volume 11, 1976, Pages 299-329.*

32- *W. Brandt and G. Lapicki."The energy-loss effect in inner-shell Coulomb ionization by heavy charged particles" Phys. Rev. A 23, 1717, 1981.*

33- *B. W. Swartz, "Availability of cerium oxide nanoparticles as a radioprotector against proton radiation for non-malignant cells." A Ph.D. dissertation - Department of Physics - East Carolina University in 2015.*

34- *E. I. Azzam, Jean-Paul Jay-Gerin, and D. Pain. "Ionizing- radiation-induced metabolic oxidative stress and prolonged cell injury, Cancer Letters." 327: 48–60 (2012).*

35- *R. Hanal, M. Y.A. Z.U., K. HIE, "On the experimental distinction between ssbs and dsbs in circular DNA." International journal of radiation biology Date: May 1, 1998.*

36- *N. B. Carlson, "Protection and sensitization of human cells to proton radiation by cerium oxide nanoparticles." Ph.D. dissertation - Department of Physics East Carolina University, 2017.*

37- *R. Middleton, "A Negative Ion Cookbook," Department of Physics, University of Pennsylvania, 1990. see http://www.pelletron.com/cookbook.pdf, January 2021.*

38- *R. Middleton, "A versatile high-intensity negative ion source "Nuclear Instruments and Methods 214, pp:139-150 (1983).*

39- *R. Middleton, "A versatile high-intensity negative ion source " Nuclear Instruments and Methods 220, pp:105-106 (1984).*

40- *E. Maertz, "Fast carbon ion and proton-induced electron emission from condensed phase biological targets." Ph.D. dissertation, Department of Physics - East Carolina University, 2018.*

41- *National electrostatics corp. Instruction Manual for Operation and Service of 6SDH-2 Pelletron accelerator. East Carolina University, Department of Physics, Accelerator lab documents, 2021.*

42- *National Electrostatics Corp., Instruction Manual for Operation and Service of Fast-acting valve VS2F. East Carolina University, Department of Physics, Accelerator lab documents, 2021.*

43- *National Electrostatics Corp., Instruction Manual for Operation and Service of Remote slit drive system. East Carolina University, Department of Physics, Accelerator lab documents, 2021.*

44- *National Electrostatics Corp., Instruction Manual for Operation and Service of Electrostatic quadrupole quadruplet lens model EQQ5.5-5. East Carolina University, Department of Physics, Accelerator lab documents, 2021.*

45- *National Electrostatics Corp., Instruction Manual for Operation and Service of NEC Coaxial Pressure Sensor. East Carolina University, Department of Physics, Accelerator lab documents, 2021.*

46- *https://www.goodfellow.com/catalogue. January 2021.*

47- *Manual of PTP 703 passive isolation optical table supports. East Carolina University, Department of Physics, Accelerator lab documents, 2021.*

48- *Z8 Series Motorized DC Servo Actuators Thorlabs User Guide. East Carolina University, Department of Physics, Accelerator lab documents, 2021.*

49- *MCA-527 Digital Multi-Channel Analyzer User Manual GBS Elektronik GmbH. East Carolina University, Department of Physics, Accelerator lab documents, 2021.*

50- *Scientific-Grade Digital Camera User Guide & Fast Frame Rate CCD Scientific Cameras for Microscopy. https://www.thorlabs.com/navigation.cfm?guide_id=2365. January 2021.*

51- *Application Note AN-SDD-003: Amptek Silicon Drift Detectors. Amptek, INC.*

52- *XR-100SDD User's Manual, Amptek, INC.*

53- *http://www.srim.org/SRIM/SRIMINTRO.htm. January 2021.*

54- *Y. Xu, G. Randers-Pehrson, S.A. Marino, G. Garty, A. Harken, D.J. Brenner "A horizontal multi-purpose microbeam system" Nuclear Inst. and Methods in Physics Research, A 888 (2018) 18–21.*

55- *C. Allen, T. B. Borak, H. Tsujii, and J. A. Nickoloff, Mutation Research 711 (2011) 150-157" Heavy charged particle radiobiology: Using enhanced biological effectiveness and improved beam focusing to advance cancer therapy."*

56- *Christopher M. Boyd, "Modification of cell survival rates by cerium oxide nanoparticles for exposure to proton radiation." Ph.D. dissertation, Department of Physics - East Carolina University, 2018.*

57- *C. Trager "The study of novel electrostatic electron lenses." Ph.D. Dissertation, physics department, Royal Holloway and Bedford New College (United Kingdom), 1987.*

58- *TransfeX™ Transfection of Plasmid DNA into MCF 7– ATCC.*

59- *Frank J. Brand III, Mahtab Forouzandeh, Harmanpreet Kaur, Francesco Travascio, and Juan Pablo de Rivero Vaccari, Acidification changes affect the inflammasome in the human nucleus pulposus cells, Journal of Inflammation 13, 29 (2016).*

60- *Almut Herrmann and Hubert H. Felle, "Tip growth in root hair cells of sinapis alba L significance of internal and external Ca2+ and Ph", The New. Phys. 129, 3, 523-533 ,1995.*

61- *T. Konishi, M. Oikawa, N. Suya, T. Ishikawa, T. Maeda, A. Kobyashi, N. Shiomi, K. Kodama, T. Hamano, S. H. Takeda, M. Isono, K. Hieda, Y. Uchihopi and Y. Shirakawa "A focused vertical system for proton irradiation of a single-cell for radiobiological research." Journal of Radiation Research, 54, 736–747, 2013.*

62- *The first hormone--responsive breast cancer cell line. Levenson AS, Jordan VC. MCF---7: Cancer; 57(15):3071-8, 1997.*

63- *Marcos A. C. de Araújo, Rubens Silva, Emerson de Lima, Daniel P. Pereira, and Paulo C. de Oliveira "Measurement of Gaussian laser beam radius using the knife-edge technique improvement on data analysis." Applied optics. Optical technology and biomedical optics, Volume 48, Issue 2, 2009.*

64- *Thermo Scientific Multiskan FC User Manual Rev. 2.2, Cat. No. No. 7710. https://assets.thermofisher.com/TFS-Assets/LCD/manuals/N07710-ver2.2-Multiskan-FC-User-Manual-EN.pdf , April 2021.*

65- *Belli M, CeraF, Cherubini R, Dalla Vecchia M, Haque AM, Ianzini F, Moschini G, Sapora O, Simone G, Tabocchini MA, Tiveron P. RBE–LET relationships for cell inactivation and mutation-induced by low energy- protons in V79 cells: further results at the LNL facility. International Journal of Radiation Biology 74(4):501-9: 1998.*